Spring 2016

Comprehensive assessment and characterization of pulmonary acinar morphometry using multi-resolution micro x-ray computed tomography

Abhilash Srikumar Kizhakke Puliyakote
University of Iowa

COMPREHENSIVE ASSESSMENT AND CHARACTERIZATION OF PULMONARY ACINAR MORPHOMETRY USING MULTI-RESOLUTION MICRO X-RAY COMPUTED TOMOGRAPHY

by

ABHILASH SRIKUMAR KIZHAKKE PULIYAKOTE

A thesis submitted in partial fulfillment
of the requirements for the Doctor of Philosophy
degree in Biomedical Engineering in the
Graduate College of
The University of Iowa

May 2016

Thesis Supervisor: Professor Eric A. Hoffman

Graduate College
The University of Iowa
Iowa City, Iowa

CERTIFICATE OF APPROVAL

_____

PH.D. THESIS

_____

This is to certify that the Ph.D. thesis of

Abhilash Srikumar Kizhakke Puliyakote

has been approved by the Examining Committee for
the thesis requirement for the Doctor of Philosophy degree
in Biomedical Engineering at the May 2016 graduation.

Thesis Committee: _____
Eric A. Hoffman. Thesis Supervisor

_____
Joseph M. Reinhardt

_____
John D Newell Jr.

_____
Ching-Long Lin

_____
Madhavan L. Raghavan

_____
Merryn H. Tawhai

To my parents, and my wife and best friend, Janani.

The most exciting phrase to hear in science, the one that heralds new discoveries, is not ‘Eureka!’ but ‘That’s funny…’

Isaac Asimov

ACKNOWLEDGEMENTS

The work presented here would not be possible without the support and assistance of others, to whom I am deeply grateful. First of all, I would like to thank my advisor, Dr. Eric Hoffman, for his encouragement and support throughout this project. His vision and guidance have helped me explore my interests and grow as a scientist and researcher. I sincerely appreciate his efforts and the constructive guidance he has continually provided at each stage of my progress at Iowa.

I would also like to thank my academic advisor, Dr. Joseph Reinhardt who opened the doors to my research and for all his guidance and efforts in planning my doctoral program at Iowa. The Biomedical department has been kind to me and I must thank each member of the administrative staff, from Lorena to Courtney, for their support and patience in responding to all my questions and requests. Thanks also to Drs. Jessica Sieren and John Newell for all the guidance and help they provided over the years. They have provided valuable insights that have helped improve my research and my thought processes.

I am also grateful to Dragos Vasilescu, my lab mentor and colleague. His time and efforts provided me with the knowledge and experience that were critical in helping me develop my research. I enjoyed our time at Iowa and in Virginia and I am indebted to him for starting me on the path to exploring new experiences in foods and adventure. Thanks to my colleagues at APPIL, both current and past, for all their help and guidance. I have great memories of my time at Iowa thanks to Ahmed Halaweish, Matthew Fuld, Youbing Yin, Krishna Iyer, Samantha Dilger and Emily Hammond, who made the lab a friendlier place with their presence.

I must thank all the staff at APPIL, Timothy Eggleston and John Morgan, Melissa Shirk and Chelsea Sloan for their help and support. A special thanks to Ann Thompson who is the lifeline for our group. She has provided help at every approach and has always been a comforting presence.

Thanks to my friends, who have made Iowa City a pleasant place and full of great memories. Sandeep Bodduluri, I have enjoyed our conversations and discussions and will miss our brainstorming ideas and evening talks over tea. Thanks to Renu Pariyadath, Sucheta Mohapatra, Vijaya Joshi, Astha Singhal and Guhan Sukumaran, whose homes were open to me at all times. Thanks to Ajay Ramji who has always supported me in need and all the other friends who have been with me along the way.

Thanks to my parents, without whom I would have failed even before starting. This entire stage of my life is a realization of their dreams and their unwavering faith in me. They have supported me through thick and thin and have always been by my side. Finally, I must thank my best friend, my wife, Janani Natarajan. Thank you for being there for me at every turn. You have always known what was needed and have been the one I can always lean on. Your support and love have made all of this possible.

The work presented in this thesis was funded in part by the following grants: National Institutes of Health Grants R01-HL-080285, R01-HL-112986, 1-S10-RR019242-01, 1-S10-OD018503-01, P30-ES005605 and by National Science Foundation/Major Research Instrumentation Grant 0923297 awarded for "MRI: Development of the Next-generation Nano-CT system for ROI-focused Scanning and Exact Interior Reconstruction."

ABSTRACT

The characterization of the normal pulmonary acinus is a necessary first step in understanding the nature of normal structure-function relationships in the lung and in assessing the etiology of pulmonary pathology. Murine models play a vital role in the advancement of current understanding of the dynamics of gas exchange, particle deposition and the manifestations of diseases such as Chronic Obstructive Pulmonary Disease, Cystic Fibrosis and Asthma. With the advent of interior tomography, high-resolution micro computed tomography (μCT) systems provide the ability to nondestructively assess the pulmonary acinus at micron and sub-micron resolutions. Through the development of new center-line-based image analysis methods coupled with the development of imaging protocols incorporating Systematic Uniform Random Sampling (SURS) principles applied to intact ex-vivo lungs fixed in-situ, we seek to utilize interior tomography to characterize the structure of pulmonary acini in mice and study the variations across the variables of age, location within the lung and strain phenotypes.

Lungs from mice of three common research strains were perfusion fixed in-situ, and imaged using a multi-resolution μCT system (Micro XCT 400, Zeiss Inc.). Using lower resolution whole lung images, SURS methods were used for identification of region-specific acini for high-resolution imaging. Acinar morphometric metrics included diameters, lengths and branching angles for each alveolar duct and total path lengths from entrance of the acinus to the terminal alveolar sacs. In addition, other metrics such as acinar volume, alveolar surface area and surface area/volume ratios were assessed.

A generation-based analysis demonstrated significant differences in acinar morphometry across young and old age groups and across the three strains. In addition we have demonstrated distinct structural differences between central and surface acini. The method was successfully adapted to large animals and the data from one porcine specimen has been presented. The registration framework provides a direct technique to assess acinar deformations and provides critical physiological information about the state of alveolar ducts and individual alveoli at different phases of respiration.

The techniques presented here allow us to perform direct assessment of the three-dimensional structure of the pulmonary acinus in previously unavailable detail and present a unique technique for comprehensive quantitative analysis. The acinar morphometric parameters will help develop improved mathematical and near-anatomical models that can accurately represent the geometric structure of acini, leading to improved assessment of flow dynamics in the normal lung.

PUBLIC ABSTRACT

The pulmonary acinus is a collection of sac-like structures called alveoli that form at the very end of the airways in mammals. The acinus is the site of all gas exchange (oxygen delivery and carbon dioxide clearance) in the lungs and as such, represents the functional part of our respiratory system. A detailed study of the structure of the acinus is essential in furthering our understanding of the nature of respiration and gas exchange; however our understanding of acinar structure has been limited due to the challenges presented in the small size of the over-all structure and the individual components and by the fact that when the components are separated, their geometry is altered. Advancements in technology, such as CT imaging systems with the ability to look at micrometer scale, provide us with unique opportunities to perform detailed measurements of the acinus without the constraints that limited previous work.

We present techniques to study the three-dimensional structure of the pulmonary acinus in mice through the latest developments in imaging technology, without distorting or destroying the sample. We present a method to sample and perform detailed analysis of the normal structure of acini in three genetic strains of mice, and show evidence of how this can be used to explore the human respiratory system. Through this work, we put forward a set of techniques and methods that expand our current understanding of the mammalian lung structure and allow researchers to explore the nature of normal and diseased lungs in great detail.

TABLE OF CONTENTS

LIST OF TABLES

LIST OF FIGURES

CHAPTER 1. INTRODUCTION

The mammalian pulmonary acinus is defined as the peripheral part of the airways that are provided with alveoli and begins with the transitional bronchiole (1, 23, 72, 108). Functionally, this complex microstructure of alveolar ducts and alveoli represents the largest unit in which all airways contribute to gas exchange. Accurate quantitative assessment of pulmonary acinar structure is therefore an essential prerequisite to building functional models that represent the performance of the lung and assess the state of gas exchange. Gas transport in the acinar airways occurs predominantly by diffusion in the gas phase, and development of models that accurately represent the dynamics of air flow is dependent on a thorough understanding of the geometry of the alveolar ducts (14, 23, 75, 76, 89). Current models of alveolar air flow mechanics employ geometric approximations of the acinus based on available anatomical data. These models are continually improved upon, by accurate morphometric data. By extension, morphometric analysis of the pulmonary acinus is a critical component in characterizing the acinar structure, allowing for improvement in modeling. Such improved models find important applications in areas of air flow, particle transport, alveolar mechanics (42), and understanding of disease progression.

Traditionally, morphometric analysis of the acinus has been carried out by the use of classical histological techniques using stereology (102, 103, 108). Several studies have been carried out that employ serial histological sections (36, 55) and casting techniques (3, 23, 72, 80). The traditional approaches have a number of significant disadvantages including: sampling induced distortions, inability to resample, and the loss of contextual information regarding the location of sampled portions of the lung. Reconstruction

techniques applied to serial histological sections have sought to address the limitations of traditional techniques and perform direct assessment of functional parameters such as surface area and number of alveoli (55).

Micro X-ray computed tomographic (μCT) imaging (27, 65, 70) is becoming a powerful tool to overcome some of these limitations. The advent of high resolution μCT scanners that enable imaging of the lung on the order of 1-2 μm voxel sizes allow us to assess the 3D anatomy of the lung microstructures at the acinar and alveolar levels (97, 98). In addition, the non-destructive nature of μCT imaging protocols provides the flexibility of resampling, reorientation and 3D visualization of the anatomy. Perfusion fixation methods (99) have been developed which provide in-vivo like preservation of the lung structure as well as the radiologic qualities of the tissue to ensure that the ex-vivo specimens can be reliably studied and the measurements extrapolated to in-vivo images (99). The anatomical information from high resolution μCT images of the acinus has been applied to develop realistic models of alveolar mechanics (43).

Analysis of 3D tubular segments, such as the branches within an acinus, is simplified by the representation of the structures using a one-dimensional skeleton-tree. Such skeleton-trees provide a guidance tool for exploration of the entire tree and facilitate quantitative analysis of measurements along the centerline. There are multiple studies that perform analysis of airway morphometry using airway skeletonization (63, 106). The extraction of the center line has been extensively researched and there are multiple algorithms which can be used for this purpose. By applying these techniques to acinar structures, we developed a method to quantitatively assess and improve our understanding of the morphometry of the lung microstructures.

An important aspect of morphometric studies is the potential to perform assessment on a small number of samples and extrapolate the measurements to represent the whole lung. Therefore, it becomes important for any quantitative assessment technique to incorporate adequate sampling principles in order to assess the underlying heterogeneity in pulmonary structure. The 2010 ATS/ERS Joint Task Force on Quantitative Assessment of Lung Structure (29) has established standards that outline the principles of design-based stereology and recommendations that seek to ensure accuracy of measurements and balance it against efficient study design. These standards are based on the principles of Systematic Uniform Random Sampling (SURS) (19-21), allowing for efficient study design to represent the whole lung by minimizing the number of samples required. By treating slices from a microCT image as two dimensional stacks of data, SURS techniques can be implemented to create sets of acinar samples that provide unbiased estimates of acinar morphometry.

The work presented in this study seeks to present new techniques for acinar morphometric analysis and the important physiological data derived through these techniques. The aims of the study were as follows:

Aim 1: To develop a center-line based technique to assess the branch morphometry of the alveolar ducts and alveolar sacs in an acinus, acquired using high-resolution microCT imaging.

Aim 2: To develop region-based sampling techniques based on SURS to identify and sample acini from specific regional locales (the lung core and sub-pleural regions) and to assess heterogeneity in acini from two mutually exclusive locales.

Aim 3: To perform morphometric assessment of acini from three commonly used research strains and present any points of similarity or variance between the three phenotypes.

Aim 4: To demonstrate the capability of the presented techniques to assess acini from large animal and human lungs.

Aim 5: To present additional metrics that represent the functional characteristics of pulmonary acini via registration based deformation maps.

Through these individual aims, we present a methodology that can be easily applied to perform comprehensive assessments of acinar morphometry (via high-resolution microCT) in any given species. By supplementing the data from other techniques such as stereology, we can derive critical insights into the nature of pulmonary structure and function. By extending these techniques to disease models, we can study the etiology of pulmonary pathology and perform direct assessment of changes in tissue structure under various disease conditions.

CHAPTER 2. BACKGROUND

2.1 TRADITIONAL TECHNIQUES

Detailed study of acinar morphometry presents a challenge of scale. Specimen preparation and instrument precisions can contribute appreciably to measurement errors. Classical techniques have provided invaluable data that has helped shape the current understanding of lung anatomy. Some of the traditional techniques that have been utilized previously by researchers are presented below.

Morphometric analysis of pulmonary acini has traditionally been carried out by the use of classical histological techniques as previously mentioned (102, 103, 108). Histological sections represent the earliest attempts to study the structure of pulmonary tissue. The histological approach has a number of significant disadvantages including: sampling induced distortions, inability to resample the lung and the loss of contextual information regarding the location of sampled portions of the lung. In addition, the analysis of the three-dimensional architecture of the pulmonary acinus is severely limited when constrained by the two-dimensional nature of histological studies.

On the other hand, silicon rubber casting techniques provide easy direct access to the three-dimensional structure, and have been used to analyze and measure the branching pattern by microscopic dissections (3, 23, 72, 80). These procedures are susceptible to errors induced to the deformation of the septal walls during the casting process and are labor intensive, limited in application to the scale of murine lungs and not conducive to direct quantitative assessment of the 3D structure of the acinus. In addition, both techniques result in the destruction of the specimen, which removes any possibility of review and re-sampling.

Serial reconstruction involves the use of a series of photographs of serial sections and manual reconstruction of the three-dimensional structure by tracing the neighboring photographs. Rodriguez et al. (72) attempted to perform the first serial-section reconstructions of rat lung acini. They found the technique to be limited by the tedious nature and finally switched to casting of airways with silicon to assess the acini in rat and rabbits. Mercer and Crapo (55) manually traced several rat acini on photographs of serial sections with a thickness of 3 μm each. Due to the substantial effort for relating each alveolus to a ventilatory unit, Mercer and Crapo performed such a tracing for limited and undisclosed number of acini. The significant manual effort involved in addition to the disadvantages of tissue deformation and destruction, are significant disadvantages to this method. **Fig.2A, B and C** show examples of histology, silicon casts and serial reconstructions used in studies for assessment of the acinar airspaces.

2.2 IMAGING BASED TECHNIQUES

Imaging techniques offer a non-destructive alternative to study the 3D architecture of pulmonary acini. The main forays into acinar imaging have been in the MR and CT technologies. Pulmonary MRI experiments that use hyperpolarized gases have been used to perform quantitative assessment of lung microstructure in humans and mice (35, 62, 74, 92, 107). MR techniques for lung morphometry rely on estimation of the anisotropic diffusion coefficient (ADC) of the hyperpolarized gas in the lung and use previously described alveolar duct geometry as a base assumption. On the other hand, CT based techniques allow us to directly examine the 3D micro-structure of the lung. The advent of high resolution micro x-ray Computed Tomographic (μCT) imaging, combined

with developments in image processing tools, has opened venues in non-destructive 3D assessment of acini (9,31,32). In addition, multi-resolution scanning capabilities extend the application of sampling techniques, traditionally used in the areas of histology and stereology, to the μCT images, for stereological assessment of the whole lung.

2.2.1 MR IMAGING

In recent years pulmonary MRI experiments employing hyperpolarized gases such as ^{3}He (62, 107) and ^{129}Xe (35, 88) have proven important tools for performing noninvasive quantitative studies of lung microstructure. ^{3}He lung morphometry has been validated by comparison with histological measurements or CT imaging in humans (6, 74, 110), mice (62, 101), and dogs (92) and has been used to quantitatively characterize changes in lung microstructure at various stages of emphysema in vivo in rabbits(48) and in human subjects (68, 107). As a tool for studying lung micromechanics, ^{3}He lung morphometry is advantageous because it takes into account three-dimensional structure, samples all ventilated parts of the lung, and is spatially resolved. The technique employs a multiple gradient strength ^{3}He diffusion MRI to measure anisotropic diffusion of hyperpolarized ^{3}He within alveolar ducts in images that cover the entire lung (87). Based on established relationships between anisotropic diffusion of helium within acinar airways and the alveolar duct geometry, average values of alveolar duct radius and alveolar depth are obtained for the airways within each voxel of the MR image. The results can be used to calculate the average surface area and volume of individual alveoli and alveolar duct units as well as the total number of alveoli (87, 110). The significant disadvantage of this method is the underlying assumptions involved in the structure of the acinus. This technique uses a common model of the alveolar duct as a cylindrical

structure with an alveolar sleeve. The model is derived based on prior information regarding the acinar structure, which relies on the homogeneity of the branching structure across different regions in the lung. These assumptions present challenges when confronted with regional heterogeneities. An example image of an MR based assessment of the acinar airspace is shown in **Fig 3.A**.

2.2.2 OPTICAL COHERENCE TOMOGRAPHY

Optical coherence tomography (OCT) is an emerging image modality in medical diagnosis and biomedical research (50). The ventilated lung with its delicate structure of interconnected aerated alveoli and alveolar ducts are ideal targets for visualization via OCT. Because the measurement speed of OCT systems is constantly improved, time-resolved image capture of alveolar mechanics during the different phases of the ventilation cycle become possible. The 3-D alveolar structure of fixed rabbit lungs and the alveolar mechanics of ventilated and perfused rabbit lungs have been previously visualized with a Fourier domain OCT system (53, 54, 67). Researchers have introduced OCT as an investigative tool for alveolar mechanics which, in contrast to surface microscopy, provides depth information about sub-pleural alveoli (50-54, 67). **Fig 3.C** shows example images acquired using Fourier Domain OCT techniques.

OCT provides real-time information and spatial resolution that are necessary to analyze mechanics of aerated lungs on an alveolar scale during ventilation and enable in-vivo imaging at previously unavailable resolutions (~10 – 12 µm). However, they are limited by the depth of field. Therefore, current studies are either invasive through the use of needle probes to access alveoli beneath the lung surface (51), or are limited to assessment of alveoli at the lung surface through a transparent pleural window (53, 60). It

is unknown as to how representative the alveoli at the pleura are, relative to the whole lung, and this is a topic investigated through Aim 2 of this thesis. Because this depth information is missing, OCT cannot represent the ideal imaging platform to comprehensively assess and characterize acini and alveoli located more centrally in the lung.

2.2.3 SYNCHROTRON IMAGING

Synchrotron energy sources are capable of generating monochromatic beam of X-Rays. By removing the multi-spectral nature of the X-Ray beam, the signal to noise ratio of the system is increased significantly. This is especially of advantage in a complex structure such as the lung, where imaging artifacts such as beam-hardening and low contrast constraints can play a significant role in image analysis and quantitative assessment. Multiple researchers (2, 22, 65, 71, 78) have taken advantage of the application of Synchrotron based X-Ray imaging to acquire high resolution image of the pulmonary structure, allowing for the visualization of the distal airways and bronchioles. Example images of acinar structure visualized by Synchrotron Imaging are shown in **Fig 3.B**. Since tomographic imaging of the lung tissue preserves the three-dimensional structure, this method allows researchers to identify individual acini on virtual two-dimensional slices and make precise stereological analysis of the isolated acini. The high contrast and signal to noise ratio have allowed for the development of segmentation algorithms that have attempted to characterize the acinar structure (109). While this technique presents high image quality and allows for characterization of acini, access to a Synchrotron energy source forms a major hurdle for researchers. The high costs involved in developing and operating such a system make it cost-prohibitive and limit the number

of samples that can be imaged. These techniques are also limited in their flexibility in applying sampling techniques to perform unbiased estimates of the acinar structure.

2.2.4 HIGH RESOLUTION CT IMAGING

Advancements in scanner hardware and reconstruction algorithms have led to the development of high-resolution CT scanners that can perform interior tomography of an object several times larger than the Field of View (FOV) of the scan. High resolution CT techniques generate a dense stack of precisely registered serial sections. Suitable algorithms can be used to segment individual acini by the analysis of acinar airway connectivity and their relation to the peripheral vascular system, corresponding to measurements with the casting technique. In a second step, the fact that the procedure has not destroyed the tissue structure allows to study the internal fine structure of individual acini by applying stereological methods to a sample of the sections in order to accurately estimate the surface area and alveolar numbers within the bounds of the individual acinus as determined by the reconstruction procedure. One particular microCT scanner, the MicroXCT-400, developed by XRadia Inc. (Pleasanton, CA) proves ideal for the needs of sampling and characterizing acini and is described in detail. One such scanner, located at the Virginia Polytechnic Institute, was used for all high-resolution imaging on the murine lungs used in this study. The imaging of the porcine lungs was performed utilizing the second generation Xradia scanner, the Versa 520, (now under Zeiss Inc.) recently acquired by the University of Iowa through an NIH large scale shared instrumentation grant (S10OD018503-01) and housed in the Small Animal Imaging Center of the Iowa Institute of Biomedical Imaging.

MicroXCT-400 by XRadia Inc.

The setup of the Versa 520 scanner is shown in **Figures 4-8**. The scanner is completely enclosed and presents no radiation exposure to the operator who can control the scanner via the attached computing console. As shown in **Fig.4**, all operations performed at the console (A) can be observed real-time using a video feed (B). Emergency motor controls and OFF buttons (F) allow the use to react immediately to any danger to the specimen or to themselves. Opening the cabinet doors of the scanner also acts as an emergency shut off to the X-Ray source, ensuring safety of the operator. Scanner operation can be monitored via the color-coded lights (E) or via the monitor console. The console also serves as the reconstruction server, allowing for a central control for scanning and reconstruction.

The interior of the scanner is shown in **Fig.5**. The X-Ray source (A) and detector array (B) can only move in one axis, necessitating the sample to rotate for each projection. The sample is mounted on the rotating stage (C), controlled via fine motors (F, G). A close up of the sample stage is shown in **Fig.6**. Traditional CT systems rely on geometric magnification to provide increased resolution imaging of the object under study. The XRadia scanners provide a two-stage magnification, with advanced optics systems providing high resolution imaging via the use of multiple objective lenses, allowing for change in magnification with options including 0.4X, 4X, 20X, and 40X, shown in **Fig.7.** The adjustable objectives allow for the acquisition of high resolution images with geometric distortions of the object under study and provide for smooth change of resolution between scans. The scanner provides the capability to perform batch scanning, with different parameters for each scan. This allows for the acquisition of

images at different resolutions and coordinate locations. An additional advantage of this scanning workflow is the ability to register the different high-resolution images, acquired at higher magnification, to a whole sample image acquired at lower resolution via the physical coordinate system.

The sample is mounted vertically on the sample stage (**Fig.8**). Care is needed to ensure stability of the sample on the stage. Due to the high resolution nature of the scans, any movement of the sample can result in motion artifacts. The sample is capable of 4 degrees of motion: translation in x, y, z and rotation around the y axis. The orientation of the axes is also shown in **Fig.6**. Increase in x, y, and z coordinates leads to movement of the sample outwards from the scanner, downwards and towards the detector respectively. For high-resolution imaging, in order to increase X-ray photon count and signal to noise ratios, the source and detector must be moved as close as possible to the sample. For interior tomography, care must be taken to ensure that the sample has full freedom of rotation (-180º to +180º) without contacting the source or detector. Beam Hardening is a commonly observed artifact in CT imaging, resulting from the preferential absorption of low energy photons of the incident spectrum by high density objects in the beam path. Pre-hardening of the x-ray beam by means of appropriate filters at the source allows for reduction of such artifacts. The selection of the source filter is dependent on the x-ray spectrum (dependent on source voltage) and the transmissivity of the object under study. The source assembly, shown in **Fig.9**, has an adjustable filter wheel, with multiple filters designed for both low energy and high energy kilo-voltage ranges, that provides unique capability to automatically change the source filtration on-the-fly via scan protocols and can be set up ahead of time.

The unique capability to non-destructively image and segment individual whole acini in the ultra-high-resolution datasets opens up the opportunity to study the 3D morphometry in such a way as to provide the geometries needed by, for example, computational fluid dynamics, allowing for an improved understanding of gas exchange and particle delivery to the lung periphery. The new imaging and image analysis methods provide for branch-morphometry at the acinar level that has not been available to date. With these advantages in mind, high resolution microCT imaging proves the best alternative for exploring acinar analysis and has been chosen as the imaging modality for this research.

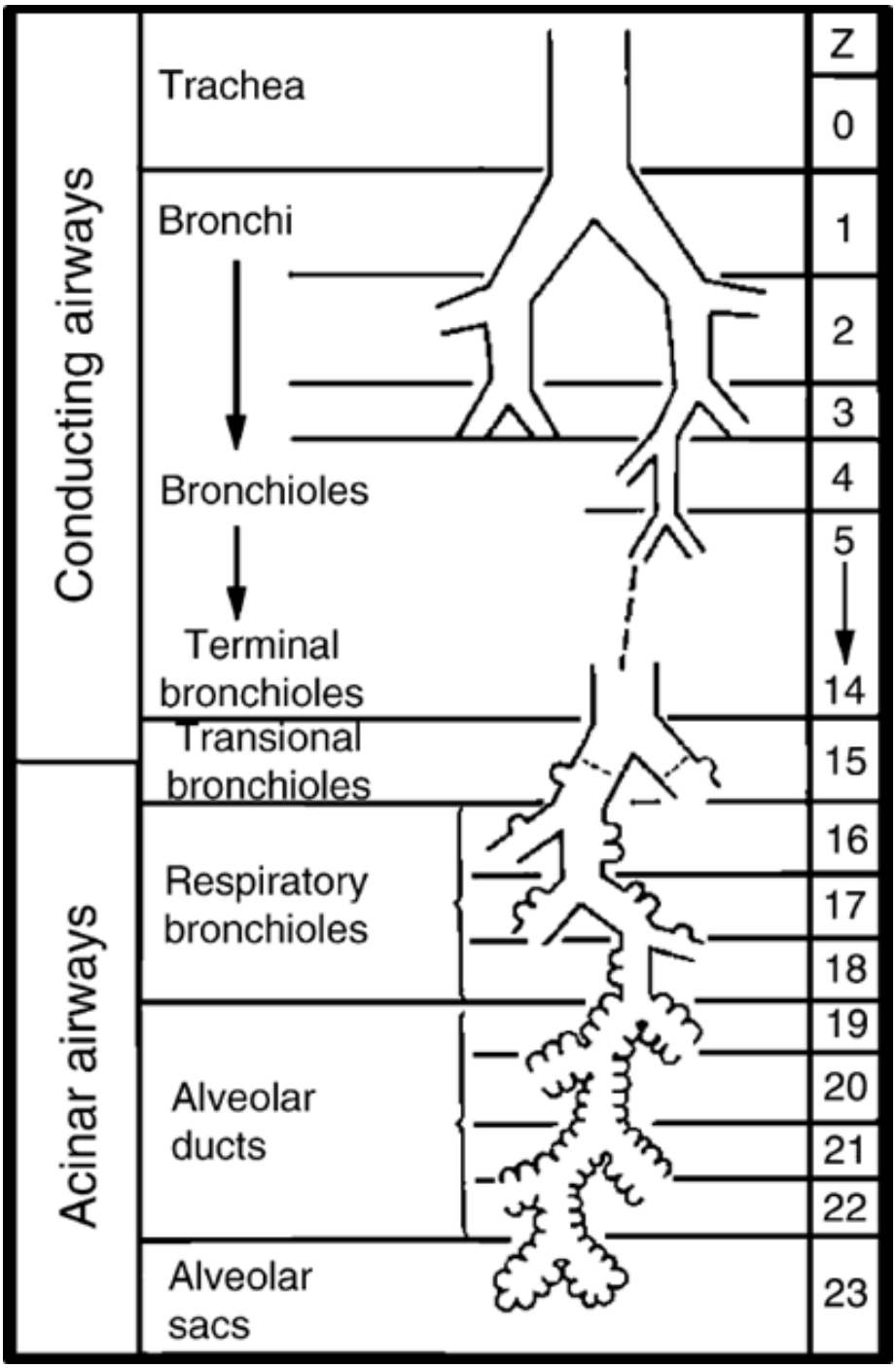

Figure 1. Model of Airway tree. The schematic shows the dichotomous division of conducting airways leading to the bronchioles that form the entrance to the acinus.

Reproduced from Lorenz (46) and *Respiratory Essentials* by John B. West (105).

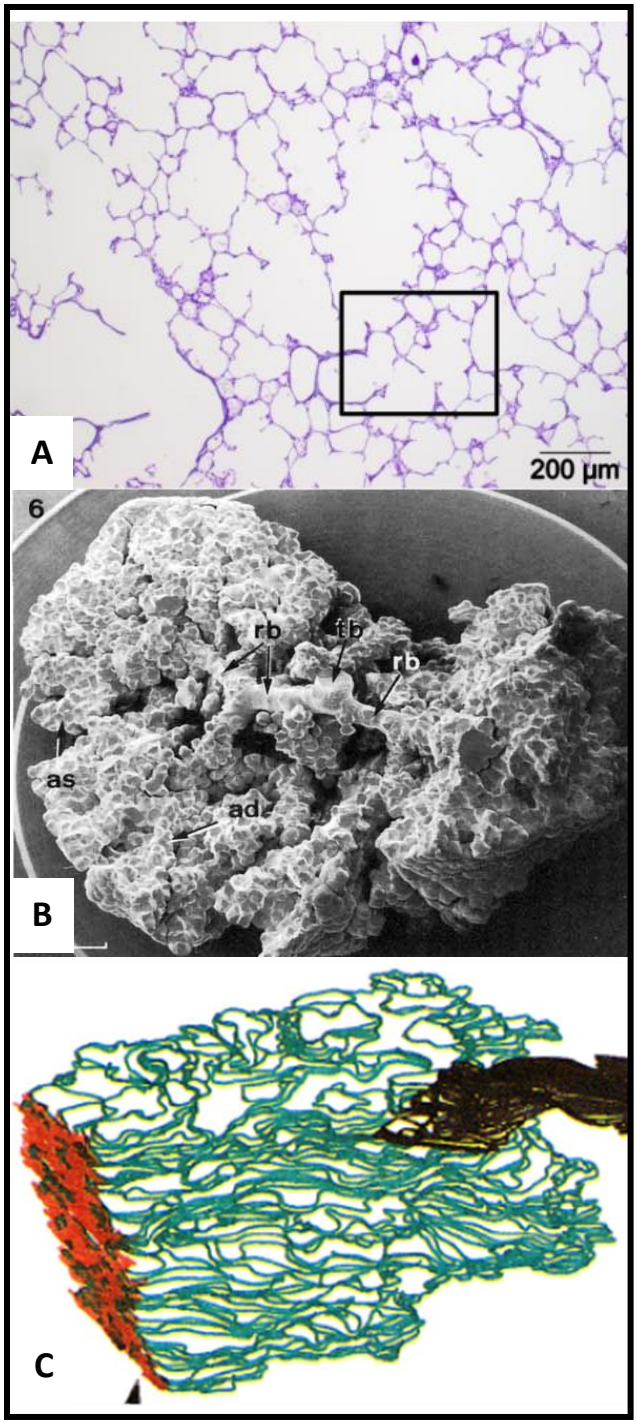

Figure 2. Traditional techniques for Acinar Analysis. Fig 2.A shows an example of histological assessment of acini. Fig 2.B is a cast of an acinus examined using Light Microscopy. Fig 2.C shows a reconstruction of an acinus from serial sections.

Reproduced from Haefeli-Bleuer and Weibel (23) , Vasilescu et. al (98) and Mercer et. al (55) respectively.

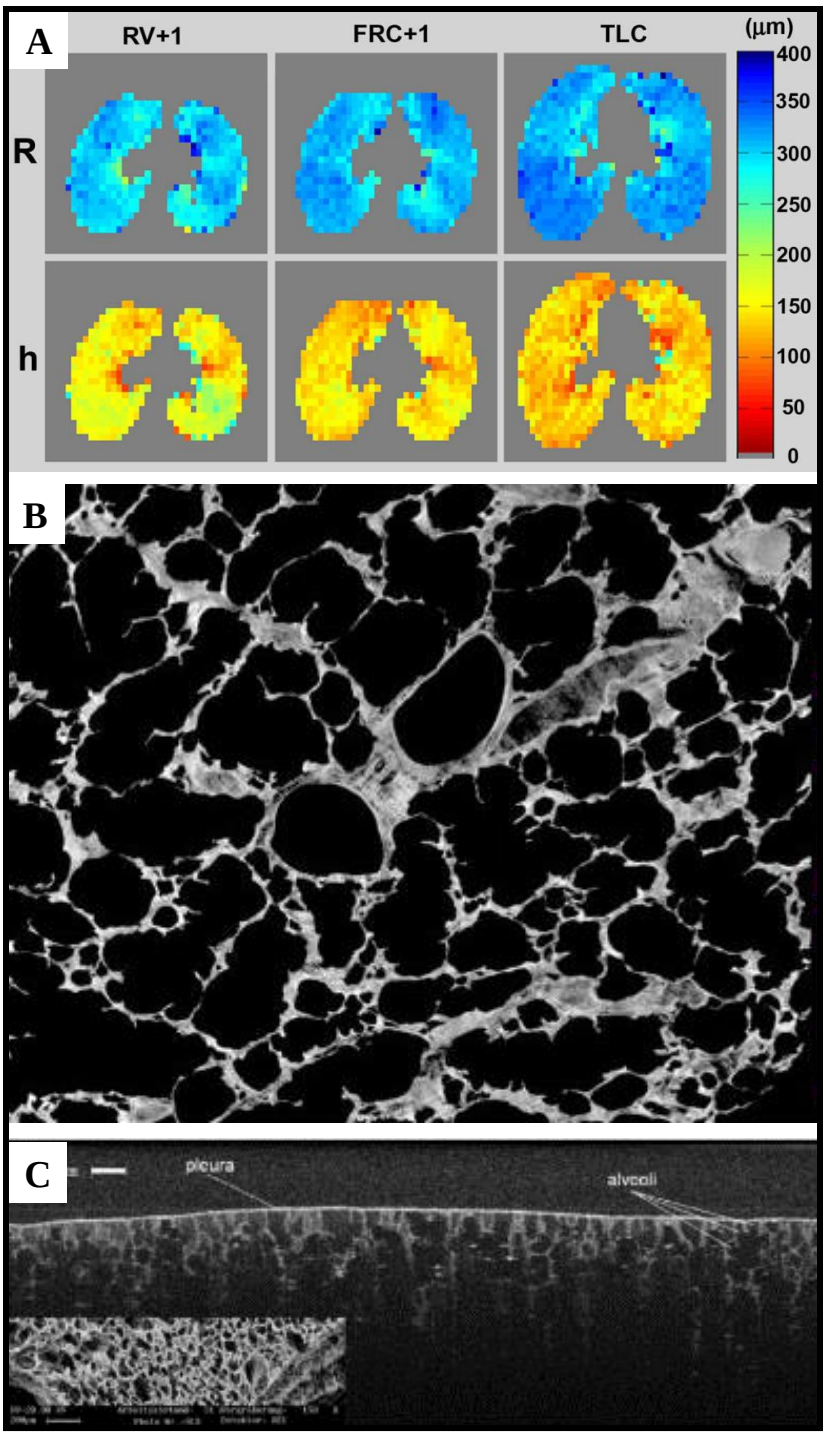

Figure 3. Imaging based assessment of acinar structure. Figures A, B and C show examples of images acquired using MRI, Synchrotron CT and Optical Coherence Tomography techniques respectively.

Reproduced from Osmanagic et al. (62), Haberthur et al. (22) and Popp et al.(67) respectively.

Figure 4. Setup of the Versa 520 scanner. Labels: A – Control computer display, B – Scanner interior video feed, C – Scanner control computer, D – Scanner cabinet, E – Status indicators, F – Emergency Reset.

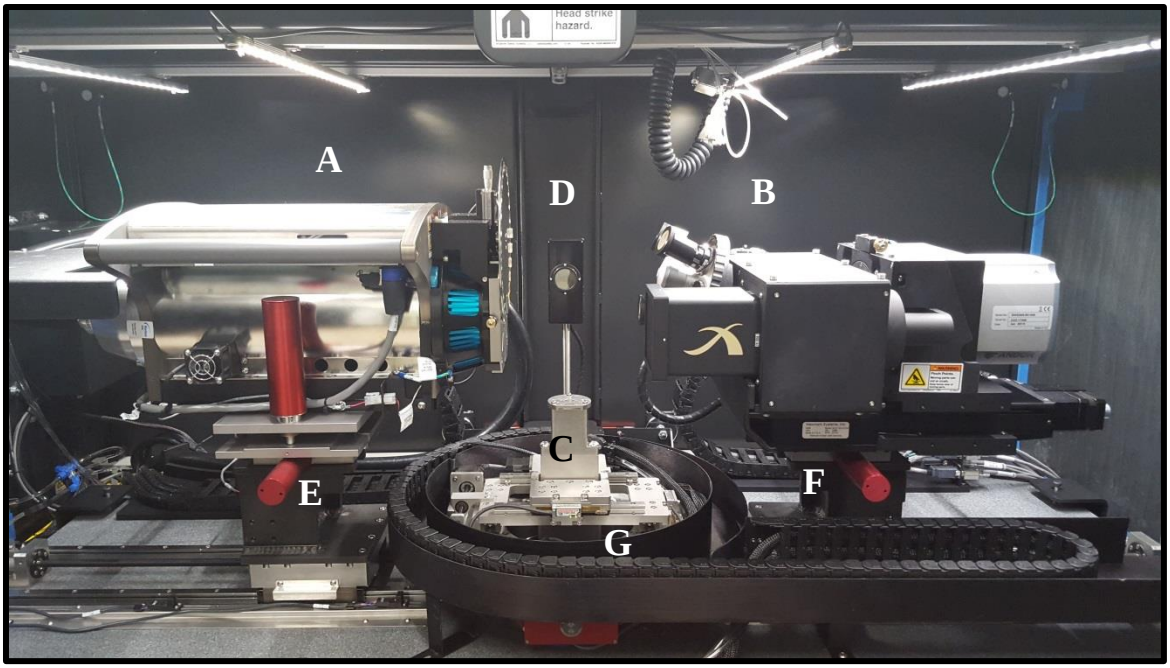

Figure 5. Interior of Versa scanner. A – X-ray Source, B – Adjustable objective setup, C – Rotating sample stage, D – Light and camera for video feed, E – Source movement motors, F – Detector movement motors, G – Sample movement motors.

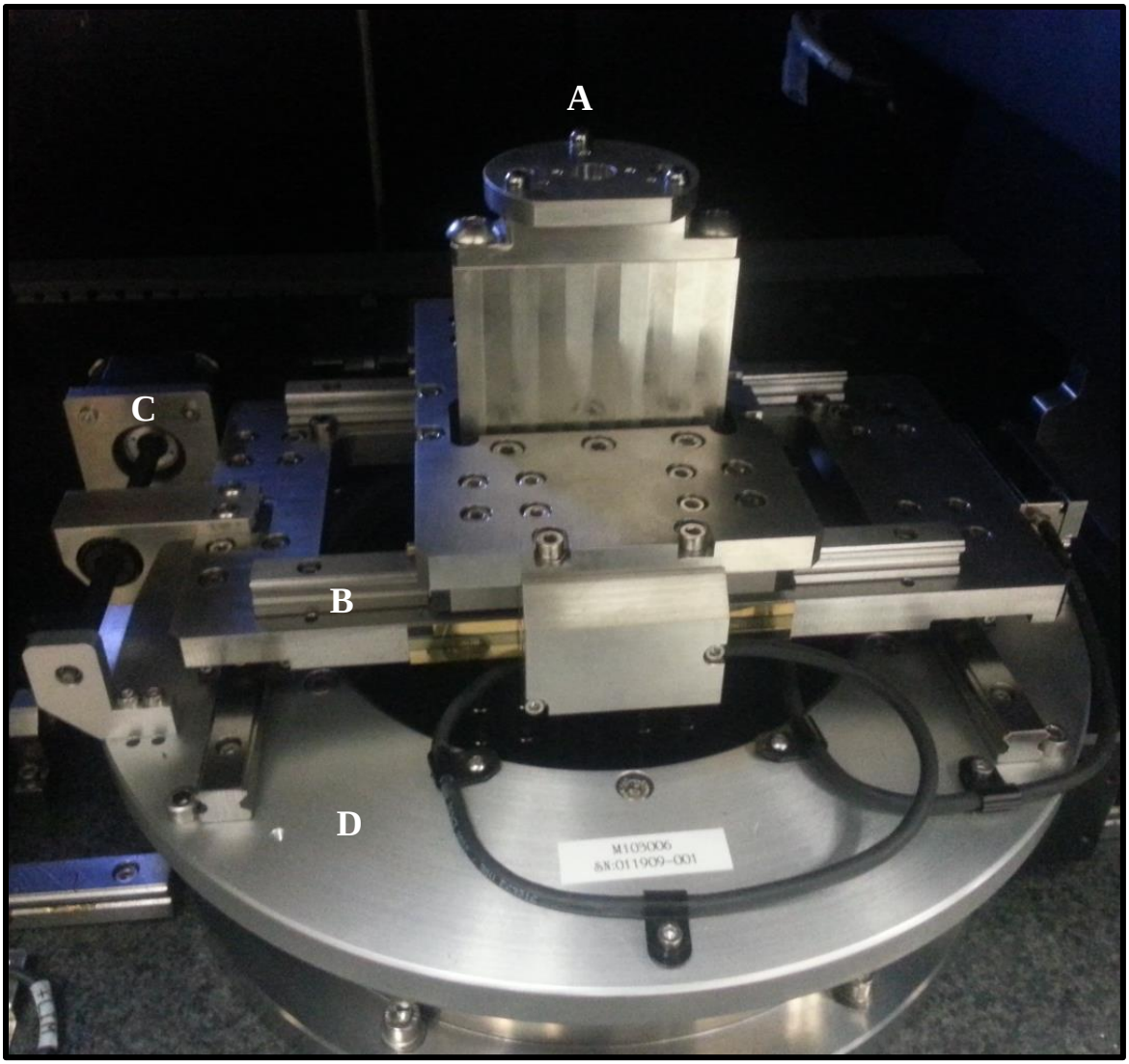

Figure 6. Close up of Sample stage. A – Mount for sample holder, B – Slider for Z axis movement (+Z towards detector). C – Slider for X axis movement (+x outwards from scanner), D – Rotating base for angular changes.

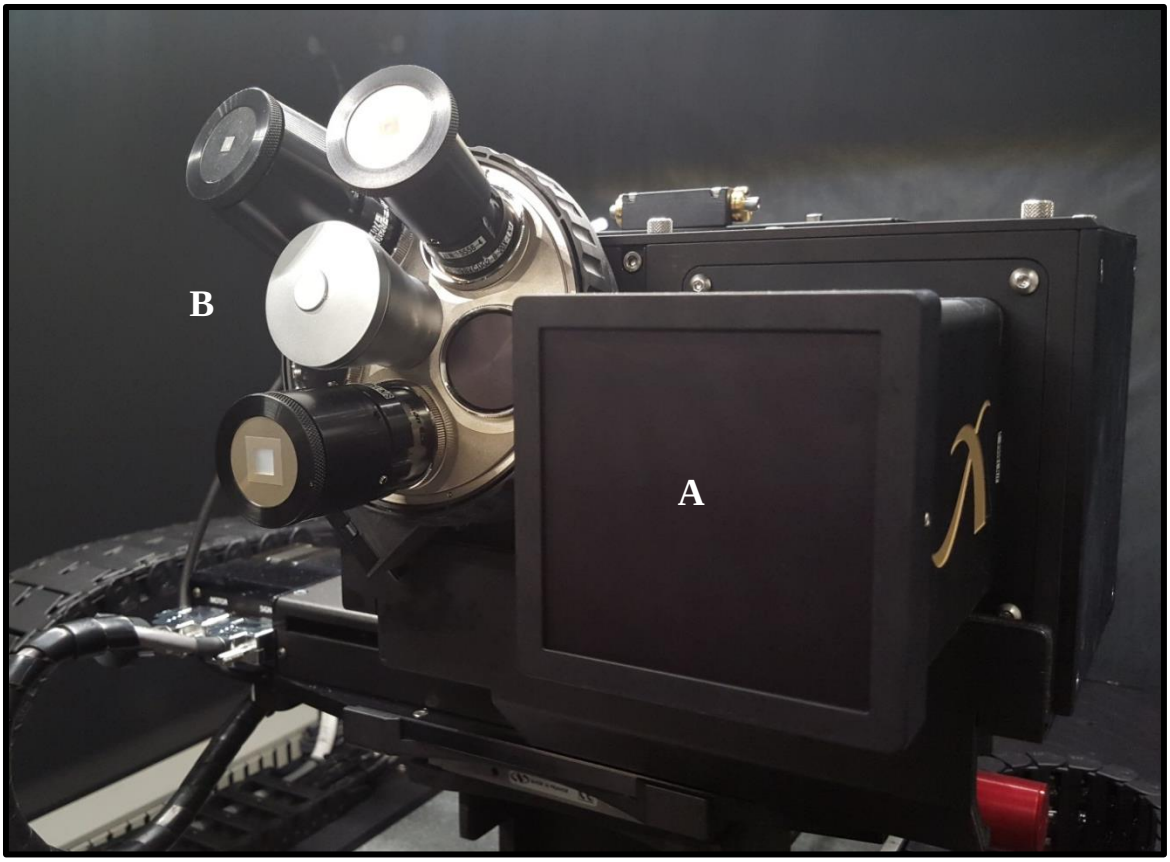

Figure 7. Close up of adjustable objectives. A – 0.5X objective, B – Array of adjustable objectives mounted on rotating disk. The Versa 520 has the following options in magnification objectives: 0.4X, 4X, 20X, 40X.

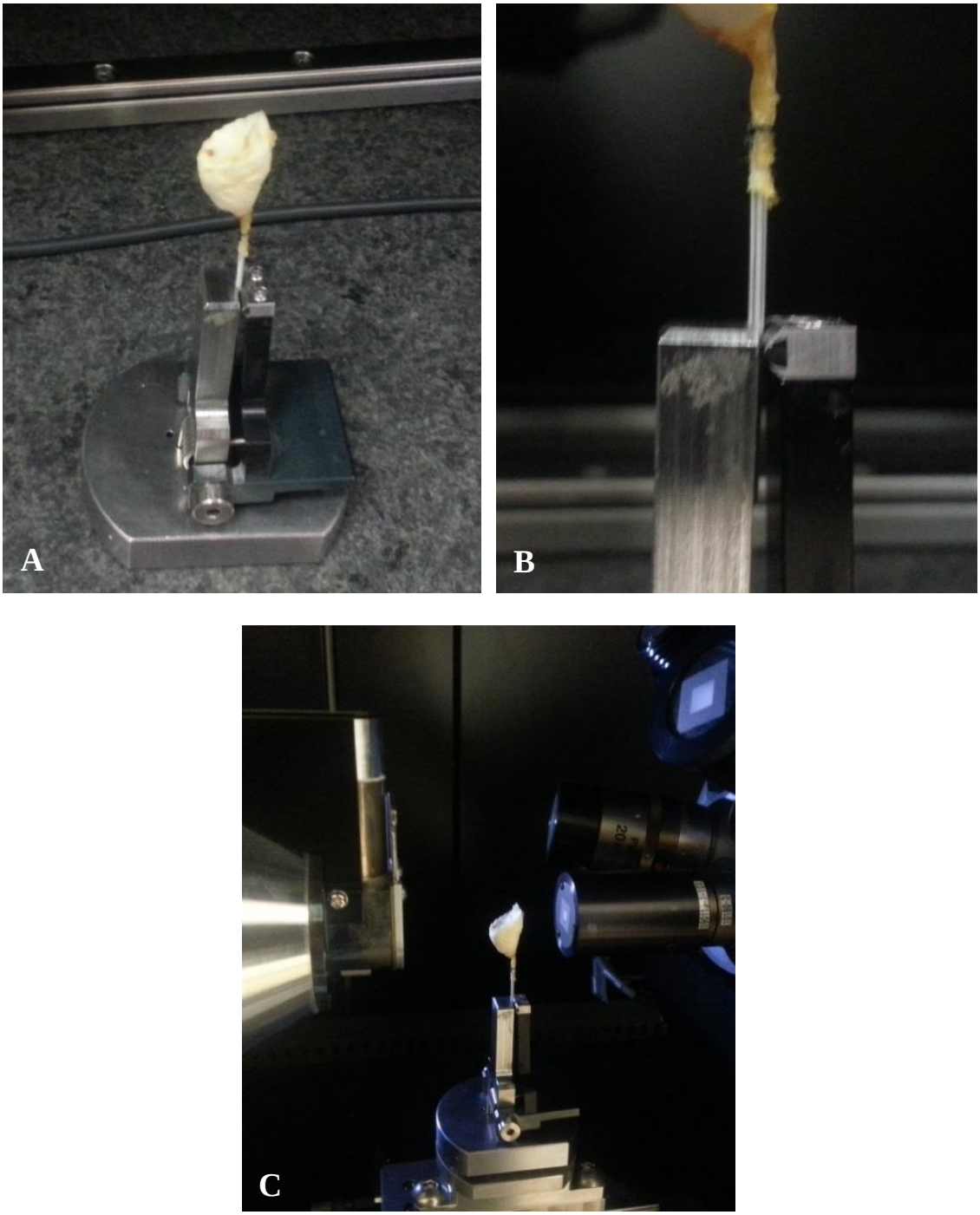

Figure 8. Mounting lung sample on sample stage. A – Lung mounted vertically using spring loaded sample holder, B – Cannula reinforced with needle is used as point of contact for holding the specimen, C – Placement of holder on stage. Stage must be rotated to ensure zero contact during scan.

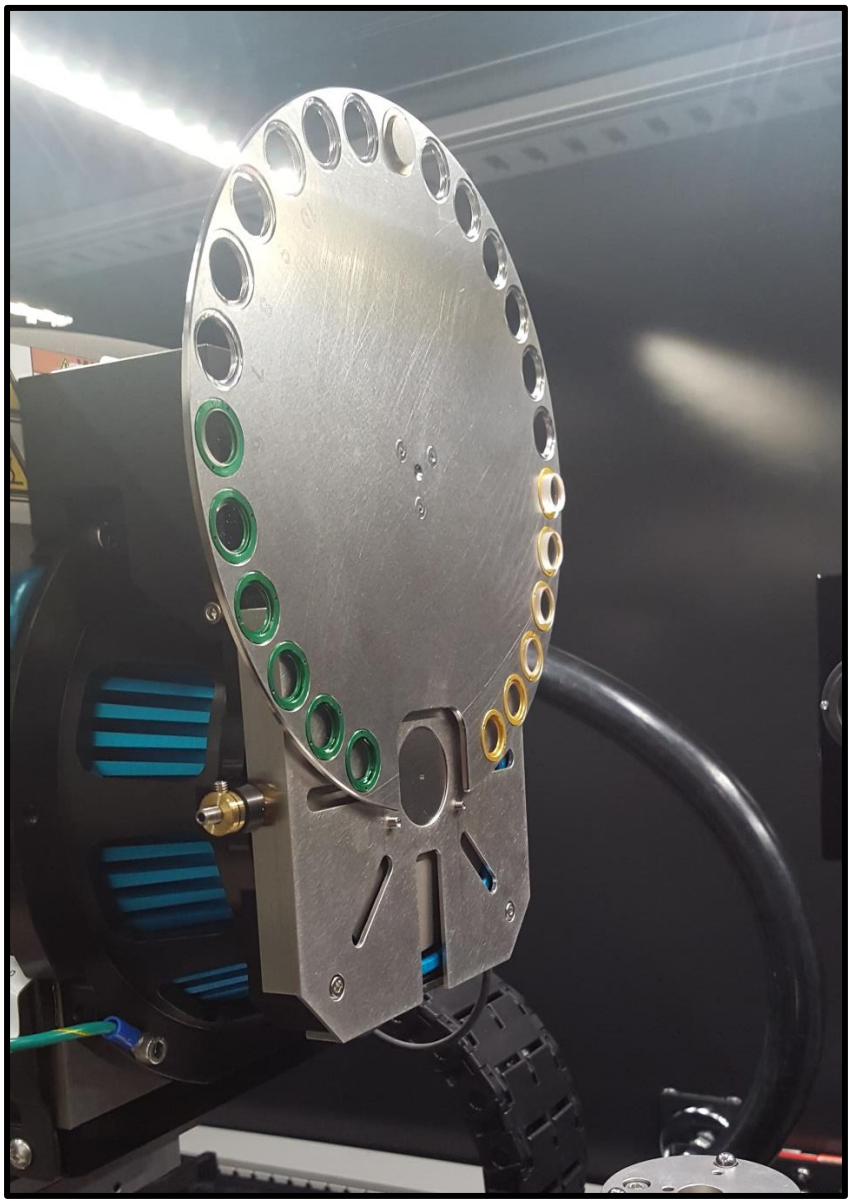

Figure 9. Adjustable Filter Wheel on the Versa 520. This feature is unique to this model

CHAPTER 3. SKELETON-BASED ASSESSMENT OF ACINAR MORPHOMETRY

3.1 INTRODUCTION

The high-resolution μCT scanners presented in the previous chapter, enable imaging of the lung on the order of 1-2 μm voxel sizes, allowing us to assess the 3D anatomy of the lung microstructures at the acinar and alveolar levels (97, 98). In addition, the non-destructive nature of μCT imaging protocols provides the flexibility of resampling, reorientation and 3D visualization of the anatomy. The anatomical information from high-resolution μCT images of the acinus has already been applied to develop realistic models of alveolar mechanics (42, 43).

Early exploration of these technologies allowed us to develop imaging protocols aimed at performing stereological assessment of the lung parenchyma (98) and validate these results via histology. Further work with the MicroXCT-400 systems allowed us to capture the pulmonary acinus via inspection of the low resolution whole lung image (97). The use of perfusion fixation techniques (99) that preserve in-vivo like state of the lung also provided the rigidity required to eliminate motion artifacts during high-resolution imaging. Through the use of specialized image processing, segmentation (16) and skeletonization algorithms (44), and applying these techniques to acinar structures, we have developed a method to quantitatively assess and improve our understanding of the morphometry of the lung microstructures. This morphometry will serve as the basis for establishing age and disease associated alterations in the micro structure of the lung.

3.2 METHODS

The workflow involved in the morphometric analysis is depicted in the series of images in **Fig.10**. A total of twelve mice from a commonly used strain (C57Bl/6, Jackson Laboratories) were used for this study, six each from two age groups (~20 and ~90 weeks of age). All of the old mice and 4 of the young mice are the same mice reported by Vasilescu et al. previously (97). The analysis presented utilizes newly developed methodologies not previously reported. The animals were housed in an animal facility at the University of Iowa and the protocols used were under the approval of the Institutional Animal Care and Use Committee (IACUC) at the University of Iowa. In-vivo imaging and lung sample preparation using a perfusion fixation method was performed as previously outlined in (99) and is briefly outlined.

3.2.1 SAMPLE PREPARATION

The animals were anesthetized prior to cannulation through a tracheotomy and were kept anesthetized throughout the study. A paralytic agent was administered and ventilation was carried out through a mechanical ventilator. The animal were then imaged in-vivo on a Siemens MicroCAT II scanner at an isotropic voxel size of 28µm using an Intermittent iso-pressure breath hold technique (59) with imaging at 20cmH_2O pressures as the gold standard against which to evaluate adequacy of fixation. After image acquisition, the animals were euthanized, the lungs were fixed via a perfusion fixation technique and extracted and dried overnight at room temperature under tracheal pressure of 20cmH2O. To verify structural integrity post fixation, the fixed lungs were scanned at the same resolution as used for the in vivo imaging and total lung as well as lobe volumes

were compared. Serial micro CT scanning of similarly fixed lungs has shown that the lung geometry and density remains stable over 6 months (99).

3.2.2 FOCUSED HIGH RESOLUTION IMAGING

The Xradia MicroXCT-400 (20KeV to 90KeV) scanner was used for all high-resolution imaging. This scanner has five microscopic objectives installed in front of the CCD camera, allowing for continuous adjustable magnification and resolution (pixel size). The combination of off-center scan capability and adjustable magnification of the camera allow us to image the whole lung, followed by focused imaging at particular spots of interest for higher resolution scans.

A large field of view (LFOV) scan was obtained using the following parameters: 40kV, 200 µA, 2000ms exposure time, detector binning of 1, a step size of 0.125 degree per projection over 180 degrees using a magnification lens of 0.5X. The datasets were reconstructed with a voxel size of ~12µm. At this resolution, the LFOV datasets allowed for identification of the terminal bronchioles which serve as the entry point for the acini and allowed us to select the locations of the high resolution (HRES) scans, such that each HRES scan contained one complete acinus. Two acini were chosen from each specimen: one each from the apical portion of the left lung and the caudal lobe of the right lung. These locations matched those used in Vasilescu et al. (97). Thus a total of 12 acini were evaluated.

To enable a comparison of the acinar morphometry between each animal, we have manually inspected the airway tree in the LFOV scans to identify and replicate the anatomical location of the chosen acini across all specimens. The HRES scans were obtained with the same scanner using the following parameters: 40kV, 200µA, 8s

exposure time, detector binning of 2, and a step size of 0.125 degree per projection over 184 degrees using a magnification lens of 10X. The datasets were reconstructed with an isotropic voxel size of 2µm with an approximate resolution of 2.5µm.

3.2.3 IMAGE PROCESSING AND SEGMENTATION

Acinar segmentation was performed using a semi-automatic 3D segmentation algorithm (16). Two sets of seed points were manually selected – one in the target acinus to be segmented and another in the surrounding airspaces. The segmentation algorithm itself (73) utilized iterative multi-scale topo-morphologic opening to iteratively eliminate leakages at different scales, and produces an isolated acinar volume at convergence. This isolated acinar mask image acts as the reference for all subsequent computations. The identification of the septal walls and other boundaries are achieved by the use of this acinar segmentation mask image. **Fig.10.A, B and C** show a single slice from the HRES image, the acinar segmentation mask and the resulting 3D acinar volume respectively.

3.2.4 SKELETONIZATION AND BRANCH POINT SELECTION

The binary acinar mask was subjected to iterative 3D erosion (average of 7-8 erosions) to simulate increased wall thickness and eliminate septal wall leakages. A connected components algorithm was run on the mask to ensure that a single connected region was used for further analysis. These steps resulted in the removal of smaller alveoli from the segmentation mask, but did not adversely affect the skeletonization or the morphometric analysis, which stopped at the level of alveolar ducts and sacs. The resulting mask was inspected after each erosion step to ensure that there was no loss of larger airspaces or loss of connectivity between branches of an acinus.

The eroded acinar mask was subjected to an iterative 3D surface thinning algorithm (44). The binary mask was iteratively and symmetrically eroded, guaranteeing the medial position of the skeleton line. **Fig.10.D** shows a 3D rendering of a representative skeleton. The skeleton line was dilated to a diameter of 5 pixels and the branch points dilated to 7 pixels to improve visualization. The skeletonization was applied by means of FIJI, an ImageJ based tool (77). Holes in the acinar mask led to the formation of loops in the skeleton structure and therefore needed to be corrected before the skeletonization step was applied. Furthermore, the generated skeleton tree had a number of short branches leading into individual alveoli. Therefore, the skeleton-tree required post processing which included pruning of very short terminal branches and elimination of loops. Subsequently, the entry point into the acinus, all branch points and all terminal nodes were selected manually using 3D visualization software (ITK-SNAP (113)). Branch points with trifurcations or higher order branching appeared as series of bifurcations due to the unit pixel width of the skeleton-tree. A distance threshold of 10 pixels (~20μm) was chosen such that branch points that occurred within this threshold of each other were merged into a single branching point with multiple child branches. The pruning step provided a simplified skeleton, which accurately represents the branching pattern of the entire acinus. **Figure 10.E** shows the results of applying the pruning step to the skeleton in **Figure 10.D**. The nodes are enlarged and color-coded for added visualization. The inset figures (**D1, E1**) show examples of pruning of loops that were not corrected during the previous steps and branches that lead to individual alveoli. The most distal points on the skeleton-tree located in the center of the alveolar sacs were labeled as terminal nodes.

3.2.5 SKELETON-BASED MORPHOMETRIC ANALYSIS

Dijkstra's algorithm (11) was applied to the skeleton tree to identify the path from each terminal node to the entrance of the acinus thus allowing us to determine the path length distribution. The branch points present on this path were recorded to analyze each individual branch. The morphometric analysis includes measurements of branch diameters, branching angles and branch lengths for each segment and the overall path length from the entry point to each terminal node. The measurements are depicted in **Figure 11** and are defined as follows:

Branch diameter (d): This is the inner diameter of each branch (i.e. the diameter of the acinar sleeve), as measured at the center of the branch. This measurement is defined to be the diameter of the largest sphere (centered at the midpoint of the branch) that will completely fit in the acinar sleeve. This measure is implemented using the distance transform map of the acinar mask, which provides a measure of the distance to the nearest septal wall. The diameter is measured at 5 pixels at the center of the branch skeleton (center ± 2 pixels) and the average of these diameters is chosen as the branch diameter.

Branching angle (Θ): At every branch point, pairwise angles are measured between each pair of child branches. To reduce the influence of small localized deviation of the branch skeleton, the angles were computed between the parent node and the centers of the branches.

Branch length (l): The branch length was computed as the sum of all points along the skeleton line between a parent node and a child node. The length computation takes into account the tortuosity of the branch.

Path length (p): The path length is the sum of branches between the entry point and a terminal node in the acinus.

The times for processing discussed above are as follows:

1) Initial image pre-processing: 15 minutes technician time; 2) Segmentation: 30 minutes technician time and 3 hour computer run time; 3) Skeletonization: 0 minutes technician time and 5 minutes computer run time; 4) Branch Point selection: 4-6 hours technician time and 0 minutes computer runtime; 5) Pruning and Morphometric Assessment: 0 technician time and 5 minutes computer run time.

3.2.6 VALIDATION

Low contrast objects such as lungs are more susceptible to noise artifacts. In addition, the polychromatic nature of x-ray photons, low keV ranges used and Compton scattering are all contributors to noise. Additionally, the nature of interior tomography and the off-center location of high resolution images lead to increased out-of-field artifacts. These can be resolved through the use of new reconstruction techniques, but these are yet to transition to microCT systems. As a step towards understanding how robust our measures are in the presence of noise we undertook to evaluate repeatability of our measures in the presence of noise.

Six acinar datasets were chosen such that the inherent noise level in each HRES image covered the range of observed noise levels from all available datasets. The noise level was calculated as the standard deviation (σ) of image intensity within the airspaces. In each acinus, the path from the entrance of the acinus to one terminal alveolar sac was computed and used for analysis.

Repeatability

Each acinus was analyzed twice to test for repeatability. Initial preprocessing and segmentation steps were identically reproduced. Branch point selection was performed by two separate users to check for user induced variations.

Sensitivity to Noise

In order to test the sensitivity of the analysis technique to noise, 3D additive Gaussian noise of mean 0 and multiple levels of standards deviations (σ = 0, 1, 2, 5, 10) was artificially introduced into the micro-CT datasets and the analysis was repeated and morphometry computed at each noise level. The original datasets were used as baseline measurements to estimate changes in branch measurements with increased noise levels.

3.2.7 STATISTICAL ANALYSIS

Two-way Analysis of Variance (ANOVA) testing (with generation number and age as the independent variables) was used on the morphometric measurements to look for statistically significant variations between the age groups and between generation numbers. The 10th generation was not considered for analysis due to lack of data points. In order to account for changes in morphometric measurements as a result of increased lung size, we normalized our measurements with total lung height as the reference. Two-way ANOVA testing was repeated on the normalized data.

3.3 RESULTS

Repeatability

Each acinus was analyzed twice (once each by two users) to determine repeatability of this method. Identical seed points were used for segmentation, followed by exact repetition of preprocessing steps and skeletonization. Manual selection of branch points and terminal nodes by the user provided the only source of variability in the workflow. Automated correction of branch points to the nearest point of divergence in the skeleton-tree compensates for any minor errors and inconsistencies in user selection. The measurements were found to be a 100% match, indicating high repeatability of the workflow across multiple users.

Sensitivity to Noise

Addition of Gaussian noise was found to reduce the signal to noise ratio (SNR) by up to 50% at the highest levels of added noise (for example, SNR was reduced from ~20 to ~10 in the case of one acinus). There was >95% overlap between centerlines for each acinus across all 4 noise levels. At very high noise levels ($\sigma = 25$, representing 10% of the maximum intensity of the 8-bit HRES image), the noise at the surface of the acinus was sufficient to cause variations of skeleton paths. At $\sigma = 25$, the center of the paths itself are displaced at points along the skeleton-tree by a distance of ~5 pixels (~10µm). One acinus (with least inherent noise and average SNR ~28) was found to exactly match with baseline measurements even with additive noise of $\sigma = 10$. Because all differences are zero, we have not displayed this graph. On average, the branch diameters are less sensitive to change in noise levels compared to branch lengths. Average change in lengths and diameters across all branches are <5µm. Bland-Altman plots showing the

pairwise changes in branch lengths across noise levels are shown in **Fig.12**. Changes in branch lengths did not exceed ±6μm and changes in branch diameters did not exceed ±5μm. Use of preprocessing steps was found to minimize the effect of noise. In the case of one acinus, there was initially found to be a considerable change in branch length (~18μm) with no significant change in diameter for just one branch when noise was set to σ=10. As a result of high noise, part of the branch leading to the alveolar sac was disconnected and eliminated during the initial preprocessing steps of morphological opening and closing. However, since the branches have relatively consistent diameter, the branch diameter was not as susceptible to an error in measurement. A manual inspection of acinar volumes after each morphological operation was found to be sufficient to eliminate such errors, improving the accuracy and robustness of the method. The challenge of higher noise levels is more prominent in the image segmentation stage than at the measurement stage. Therefore, for a given acinus, the measurements can be reliably estimated as long as the segmentation mask itself can be created without appreciable error. There were no statistically significant differences in the measurements, indicating that the current method is insensitive to noise up to an additive noise of $\sigma = 10$, matching the maximal noise inherent with the scanning modality utilized here. Similar Bland-Altman plots for branch diameters are shown in **Fig.13**.

Morphometric changes across Age groups

Using the above validated metrics, morphometric measurements in each acinus have been averaged over the generation count (estimated from the acinar entrance) and presented in **Fig.14.** Pairwise statistical comparison was performed at each generation. Acini from the older mice were found to have significantly larger branch diameters and

branch lengths at every generation ($p<0.03$ for diameters, $p<0.01$ for lengths) as shown in **Fig.14**. Acini from younger mice were found to have fewer generations on average with only one acinus in the younger mice reaching generation 10. In older mice, the segments extended to the 10^{th} generation. Because of limited number of data points in the younger mice, the 10^{th} generation was omitted from statistical comparisons between the two age groups. Normalization by total lung volumes did not affect statistical significance. Change in branch diameters remains relatively constant across generations, whereas change in branch lengths is greatest near the entrance to the acinus and diminished near the alveolar sacs. There were no significant differences in branching angles, but acini from the old age group were found to occasionally have a greater number of generations. On average there were 8.714±0.76 generations per acinus in the young mice vs. 9.286±0.76 in the old mice. However, these differences were not statistically significant. The alveolar duct volumes (of the alveolar sleeve, excluding surrounding alveoli) expressed as a percentage of total duct volume is shown in **Fig.15**. The average branching angles in acini across young and old mice averaged by the generation as measured from entrance to the acinus is provided in **Table 1**.

3.4 DISCUSSION

In both age groups, branch lengths and branch diameters progressively decrease from the terminal bronchiole up until the terminal alveolar sacs. The decrease in branch lengths and diameters with increasing generation number are in agreement with previous studies in mice, rats and humans (72, 80). The 10^{th} generations in the old mice, which only include alveolar sacs, were found to have increased branch lengths. The alveolar

sacs start appearing near the 6th generation (as measured from the terminal bronchiole) on average. The effect of including terminal sacs in the sample pool for averaging might account for the reduced branch length changes (convergence of curves in **Figure 5b**) at more distal generations. In addition, this inclusion may account for the increased levels of statistical significance observed within the first few generations as opposed to the distal generations. Because we include the alveolar sacs in the terminal generations, there is a sharp increase in size when only alveolar sacs remain in the average as is the case in generation 10 of the old mice. These observations were also seen in studies in the rat acinus (77).

The comparison across the young adult and old age groups revealed significant changes in the size and the structure of acini. The data indicate that when comparing these two age groups, the alveolar ducts are larger by way of larger branch diameters and lengths without significant differences in acinar branching patterns. The greater size of alveolar ducts contributes to the greater lung volumes observed in the old mice. The duct volume in each generation expressed as a percentage of the total volume of the alveolar duct spaces (shown in **Fig.16**) is consistent between young and old mice. This indicates that while each alveolar duct has an isotropic difference in branch morphometry, the contribution of each generation to the total acinar volume remains unaffected.

The C57BL/6J strain and its mutant derivative strains are commonly used in pulmonary research, especially in investigations of genetic emphysema and early onset emphysema (17, 31, 34). Some of these strains have shown increases in alveolar duct spaces not accompanied by destruction of the septa (34) while other strains have shown destruction with age. In order to better understand the nature and onset of emphysema

versus the age related anatomic changes, it becomes important to decouple the changes in the acinar airspaces that indicate non-destructive age related anatomic changes and destruction due to pathology.

Acinar development in the mouse lung begins in the fetal stage with formation of the terminal sacs and expansion of airspaces, culminating in alveolarization and formation of septa within 2 weeks of post-natal development, and the lung is generally considered to be fully developed within 4 weeks of post-natal growth and growth continues until adulthood (approximate age of 8 weeks) (78). However, microCT based evaluation of the acinus and the alveolar septa indicate that there are changes beyond these accepted timelines (97). Our group has previously shown that the number of alveoli per acinus is significantly increased between young adult and old mice (97). Data from the current study suggests that higher number of generations within an acinus may also contribute to increased lung volumes. We see 10 generation ducts in the old mice but the differences between the average number of ducts when comparing the two age groups is not significant. These observations warrant further study. Because of the study design, whereby we have young mice and very old mice without intervening ages, we cannot state whether these changes represent a continuous architectural alteration or represent a process occurring more in association with older age. A better understanding of the time course of the observed differences will come with the study of additional age groups. What these observations do is to demonstrate the ability of high resolution 3D micro CT imaging and image processing to provide a tool whereby the structure of the pulmonary acinus can be more fully explored within the intact lung in the context of acinar spatial location.

Generation from entrance to acinus	Young Mice Mean (SD) in degrees	Old Mice Mean (SD) in degrees
1	107.11(26.68)	116.09(16.37)
2	99.24(24.62)	107.256(19.72)
3	96.83(29.46)	105.13(32.52)
4	91.12(23.34)	102.55(31.95)
5	92.75(26.25)	103.68(27.74)
6	100.83(27.14)	106.32(28.13)
7	105.19(24.81)	102.81(26.95)
8	106.91(21.89)	106.37(15.36)
9	103.25(20.17)	99.92(11.82)
10*	87.78(3.9)	100.99(17.46)

Table 1: Branching angle in young adult and old mice averaged by generation.

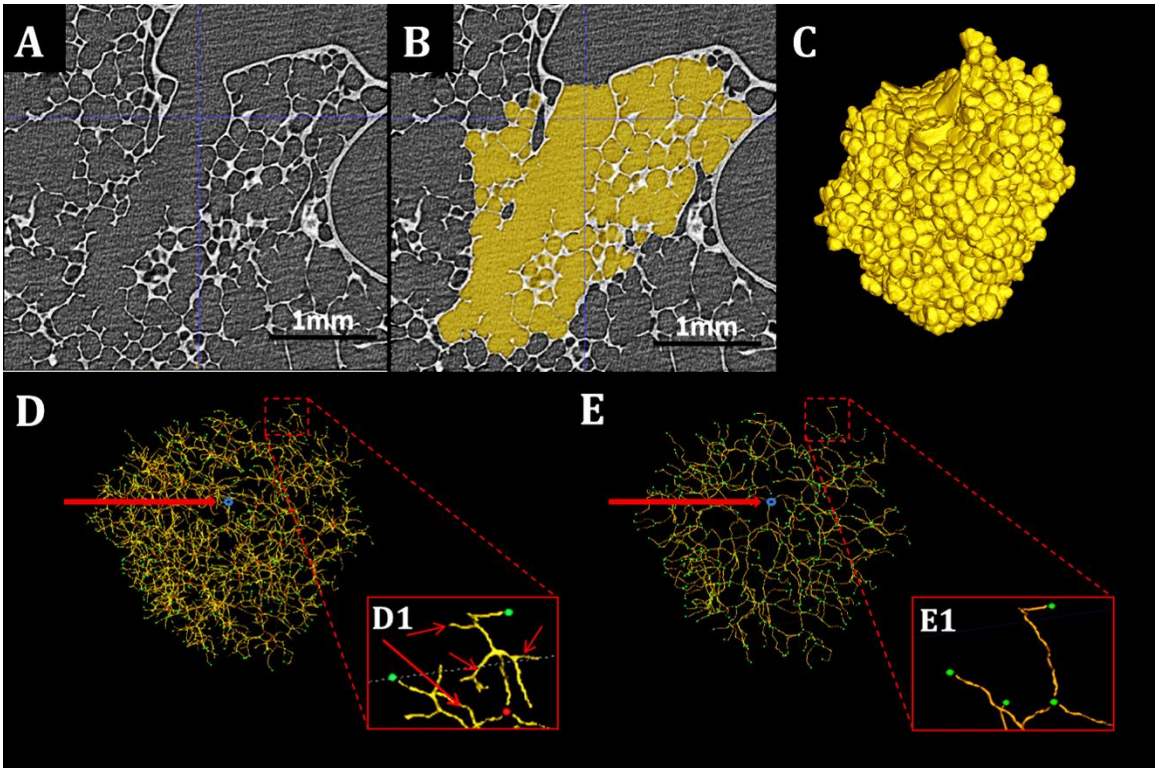

Figure 10. Workflow of Morphometric Analysis. A, B and C show a Sample slice of HRES acinar image, the 2D acinar mask and its 3D rendering respectively. D shows the original skeleton with entrance (blue), branch points (red) and terminals (green). E shows a pruned skeleton with nodes (green) and entry point (blue). The inset in each figure shows examples of the pruning process. Branches indicated by the arrows are not in the path from the acinar entrance to the terminal node shown in green and are pruned and absent in figure E.

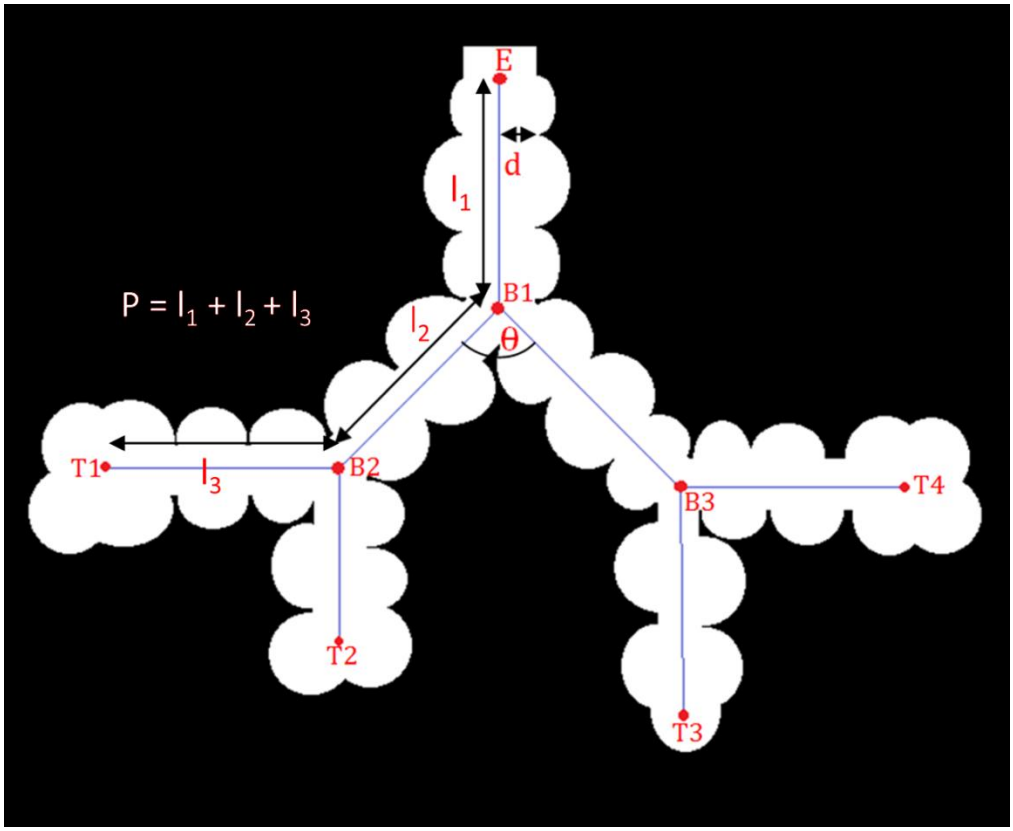

Figure 11. Schematic representation of acinar measurements. E - Entry point, B1, B2, B3 – Branch points and T1-T4 - Terminal Nodes. 'D', 'l' and 'Θ' represent branch diameter, branch length and branching angle respectively.

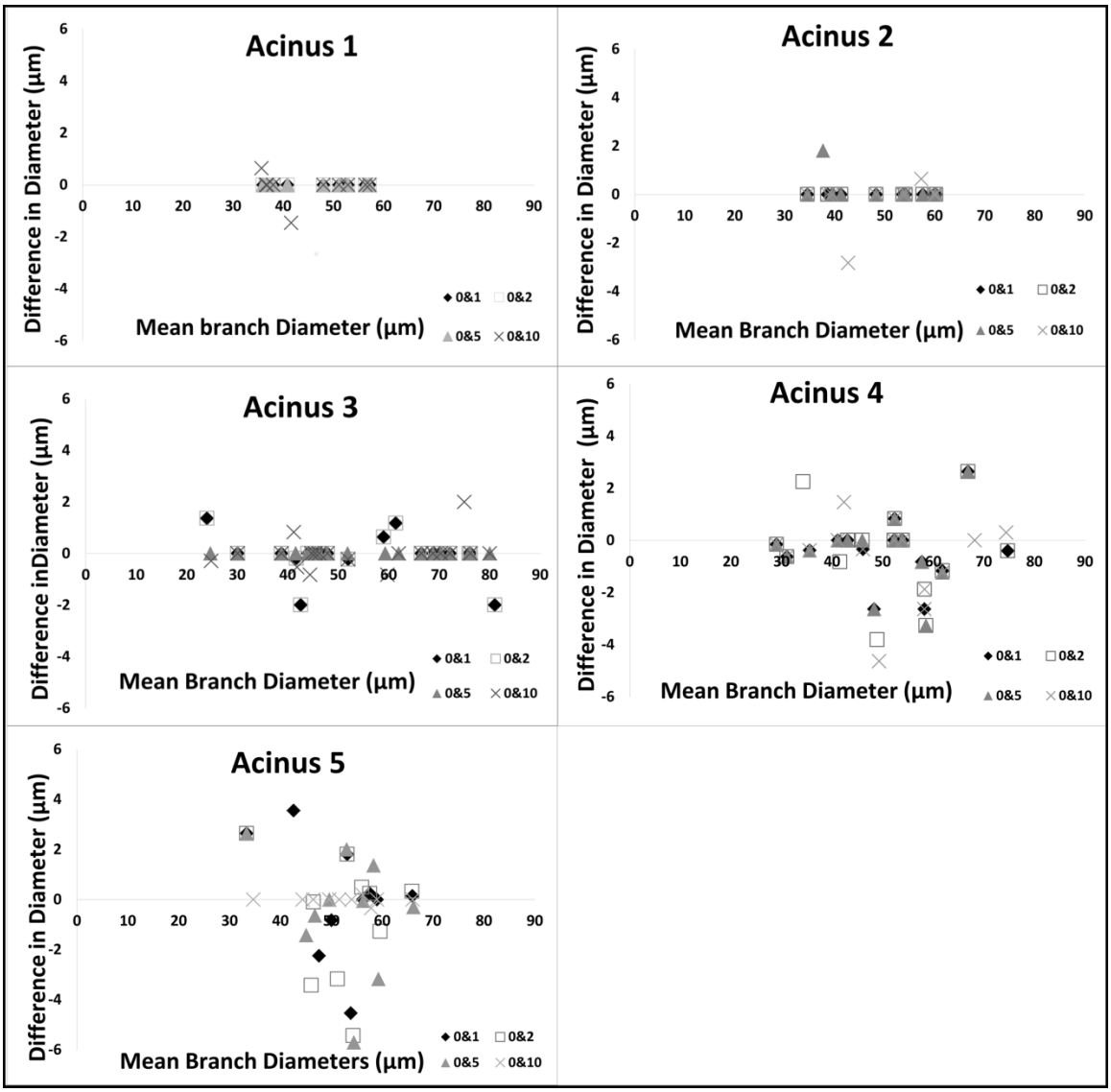

Figure 12. Bland-Altman plots showing pairwise comparison of the effect of noise levels on Branch Diameters for five acini.

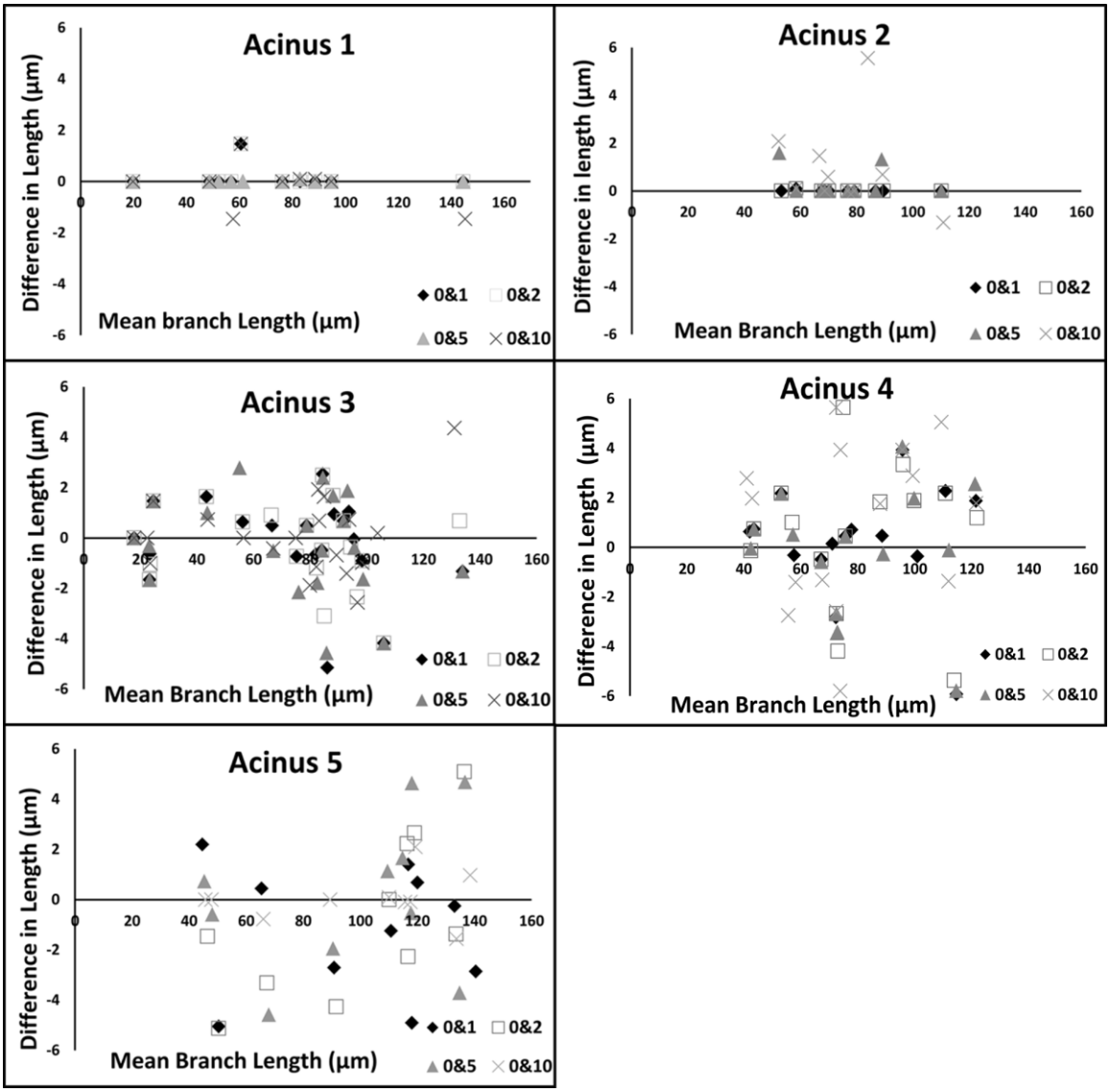

Figure 13. Bland-Altman plots showing pairwise comparison of the effect of noise levels on Branch lengths for five acini.

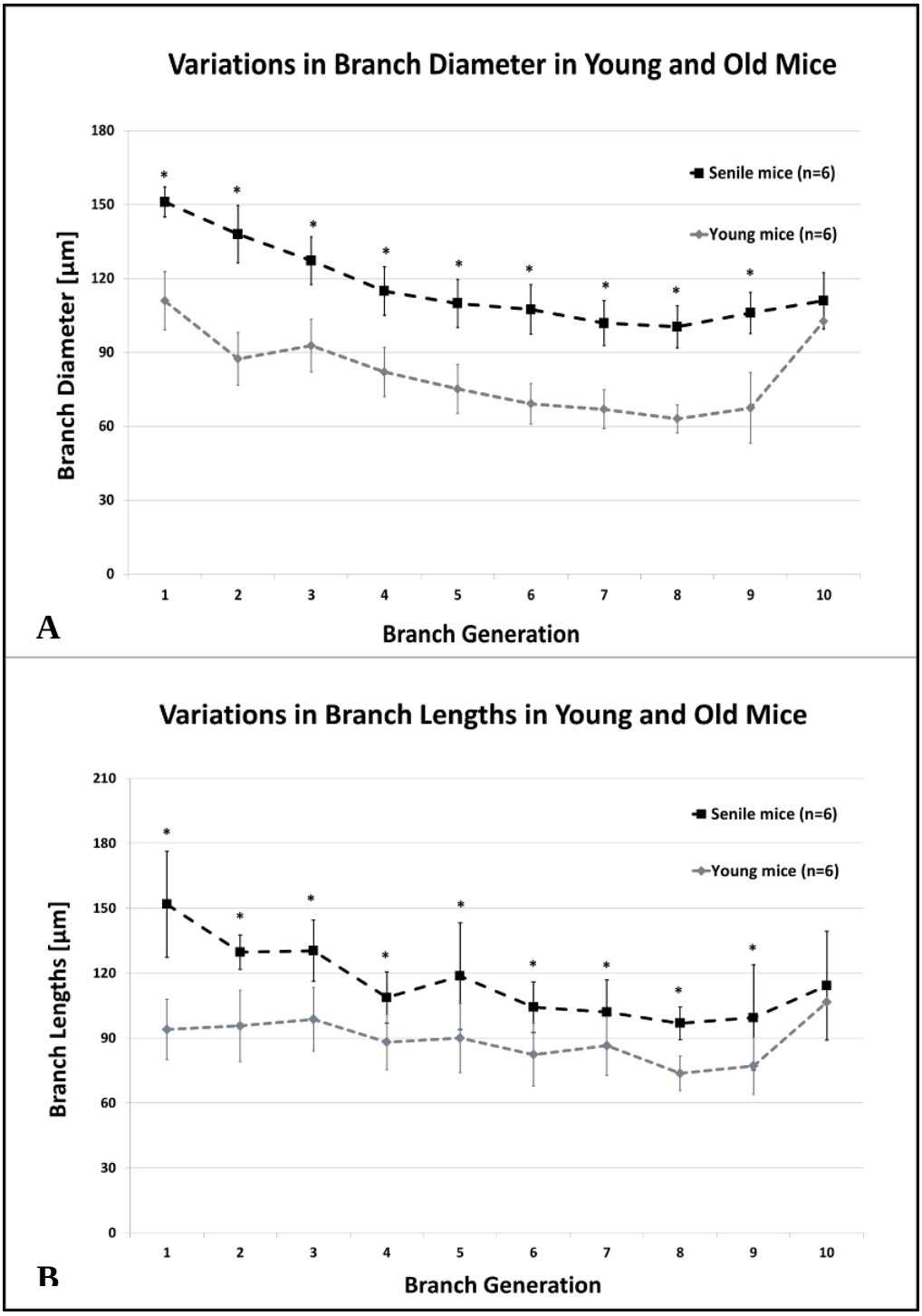

Figure 14. Variations in acinar morphometry in young and senile old mice, averaged by generation number as measured from entrance to the acinus. Generations 1-9 show statistically significant difference ($p<0.01$ for diameters and lengths).

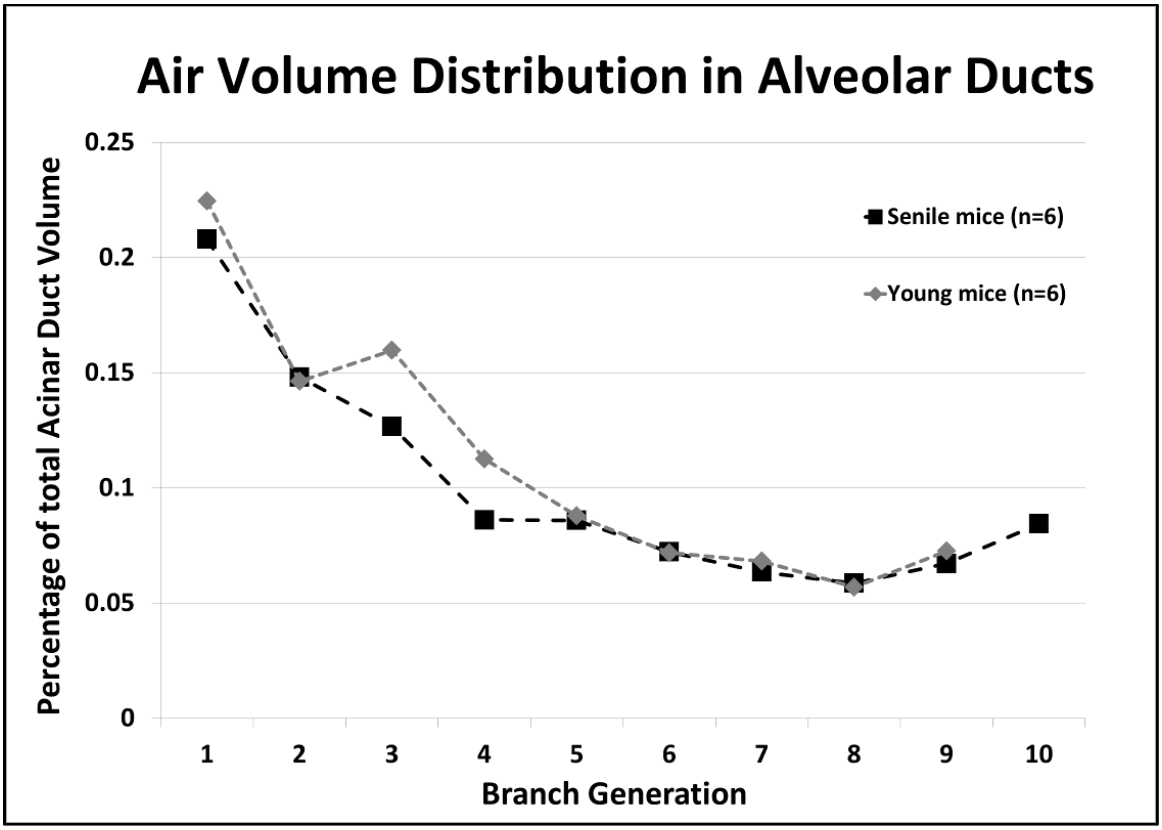

Figure 15: Percentage Distribution of Acinar Duct volume at each generation in young adult and old mice.

CHAPTER 4. SYSTEMATIC UNIFORM RANDOM SAMPLING FOR HRES IMAGING

4.1 INTRODUCTION

Fourier domain Optical Coherence Tomography (OCT) has emerged as a method which provides detailed three-dimension as well as four-dimensional (space plus time) information related acinar level lung structure and mechanics (50-54, 67). These optical techniques do not require tissue fixation and allow for in-vivo imaging in real-time. While OCT techniques enable in-vivo imaging at previously unavailable resolutions (~ 10 – 12 μm), they are limited by the depth of field. Therefore, current studies are either invasive through the use of needle probes to access alveoli beneath the lung surface (51), or are limited to assessment of alveoli at the lung surface through a transparent pleural window (53, 60). However, it is unknown as to how representative the surface alveoli are relative to the whole lung. In order to assess and understand the underlying heterogeneity in pulmonary structure, it becomes important to develop adequate sampling tools to identify selectively image acini from specified regions of interest. In order to assess and understand the underlying heterogeneity in pulmonary structure, it becomes important to develop adequate sampling tools, which incorporate the principles of design-based sampling as established by the ATS/ERS Joint Task Force on Quantitative Assessment of Lung Structure (29), to identify and selectively image acini from specified regions of interest.

In this chapter, our first goal was to develop a tool to perform sampling of acini in the fixed lung specimens through the application of the principles of SURS, with the added flexibility of selecting anatomical regions of interest.

Our second goal was to apply this tool to sample acini from two regions of interest, namely acini that extend to the pleural surface (*"surface acini"*) and acini that are bounded on all sides by lung parenchyma (*"central acini"*) and assess the variations in acinar morphometry across these two sub-locales. The assessment and characterization of the differences in acinar airspace morphometry between these two locales will provide improved understanding of the regional heterogeneity in the lung and provide information that will assist in evaluating the assessment of the surface alveoli and airspaces that have been reported through other optical techniques as representative of the whole lung.

4.2 METHODS

4.2.1 SAMPLE PREPARATION

A total of six mice from a commonly studied strain were used for this study (A/J, Jackson Laboratories, 15- 20 weeks of age). The animals were housed in an animal facility at the University of Iowa. All experiments and protocols were performed subject to approval by the Institutional Animal Care and Use Committee (IACUC) at the University of Iowa. The in-vivo lung imaging and fixation protocols are identical to the protocols presented in chapter 1, with the only difference being the breath-hold pressures used for in-vivo imaging. In-vivo pressures of 10, 20 and 30 cmH20 were used so as to capture a wider range of the physiology of respiration.

4.2.2 ACINAR SAMPLING AND SCOUT BASED IMAGING

SURS principles were used to perform sampling of suitable locations from the LFOV image for HRES imaging. The sampling process was iteratively used to reduce the dimensionality of the lung to first select individual slices from the 3D dataset and

reapplied to perform point selection on each 2D image. The process can be performed separately for right and left lungs if needed. In this study, we performed sampling considering the lung as a whole. The general steps involved are detailed below:

1. The 3D dataset is visually inspected to identify the axial limits of the region of interest i.e. first and last axial slices in which the lung can be identified: **(Z_{min},Z_{max})**. The axial limits are shown in red in **Fig.16**.

2. The axial limits are further constricted by half the size of the FOV of the HRES image (~1mm at each end equaling ~80 slices at a LFOV resolution of 12µm). This does not eliminate any part of the lung from sampling since the point selection is used to set the center of the FOV for the HRES image. The new axial limits **(Z_{start}, Z_{end})** represent viable slices for sampling.

3. The range of slices **($Z_{range} = Z_{end} - Z_{start}$)** is divided into *n* equal stacks. The number of stacks equals the number of locations to be selected for high resolution imaging. Each stack has a size $S = Z_{range} / n$ slices each. The stack boundaries are depicted in green in **Fig.16**.

4. A random offset p is chosen such that $1 \leq p \geq S$. This offset represents the slice to be selected from each stack. This offset is applied uniformly to each stack such that n slices chosen are:

$$Z_{start} + i*(S) + p \qquad i = 0, 1, 2 \ldots n-1$$

The application of the offset is depicted in yellow in **Fig.16**. These set of operations have reduced the 3D dataset to a sub-selection of 2D slices. The following

steps are applied on each slice chosen in this step and represent the second level of SURS.

Note: In this particular sub-section, 3 locations each were used for HRES imaging of central and surface acini. This was achieved by setting n= 3 and independently sampling the central and surface acini one after the other. The differentiation in sampling between central and surface acini is established at the second level of sampling.

5. A grid with row and column separation equaling the FOV of the HRES image (~2mm) is overlaid on the 2D slice. This grid mimics the stack separation that was performed in the previous steps. Similarly to the stack offset, a random offset is applied to the starting coordinates of the grid. The grid generation and application of a random offset were performed using an open source imageJ based tool (FIJI) (77). Each intersection point on the grid represents a viable coordinate for imaging. In order to limit the points to regions of interest, a binary mask image is used. The sampling tool allows the user to create a temporary 2D mask on the fly through an extrapolation of manual points or by importing a 2D mask that has already been created. This allows the user to limit the viable samples to specific regions of interest based on study design.

Note: In our study, central acini were sampled using a lung mask that was eroded to eliminate pleural regions while surface acini were sampled by using a "peel" mask by subtracting the eroded mask from the original mask to isolate acini that are on the pleural surface. An example of a 2D slice with a grid overlay, along with an example of the eroded mask and the "peel" mask is shown in ***Fig.17****. All points (excluding those that fall on large airways or pulmonary vasculature) that fall within the corresponding ROI*

mask are eligible for high-resolution imaging. The set of all eligible points for central and surface acini are shown in red and green respectively.

6. A single random intersection point in each 2D slice, which falls within the binary mask, is chosen at random as a location for HRES imaging. **Fig.17** shows an example of one randomly selected point each for central and surface acini and the FOV of the HRES image at that coordinate. The acinus at this randomly selected location is selected for imaging. In order to ensure that the chosen acinus is completely within the FOV for the HRES image, the LFOV stack is manually inspected to identify the limits of the acinus and the coordinates are shifted to center the FOV on the chosen acinus. An example of a shifted center and the new FOV are shown in yellow in **Fig.18A** along with the corresponding high-resolution image in **Fig.18B**. These selected locations are translated to scanner coordinates and sequenced in a batch for high-resolution interior tomographic imaging.

7. This protocol resulted in the sampling and imaging of three central and three surface acini from each lung specimen. A total of 36 acini, 18 central and surface acini each, were imaged. Four of the image datasets were removed from analysis due to artifacts during image acquisition, resulting in a total of 32 acini included in this analysis.

The 3D nature of the microCT dataset provides the ability to reslice the datasets at any desired orientation. In the previous study by Vasilescu et al. (98), the authors have commented on the possibility of re-orienting the image slices to avoid orientation bias. Re-slicing needs to be considered if the structure of interest (the acinus in our case) has nonrandom spatial orientation distributions, and are of significance in stereological

studies where measurements on 2D sections are used to assess 3D structure. The ATS/ERS joint task force report (29) has previously commented on the need for "orientator" procedures to perform reliable estimates of structures within the lung which have orientation biases. The report concludes that such orienting procedures are not necessary with respect to acini and alveoli which have a nearly random orientation and face all directions with equal probability. In order to simplify our sampling procedures, we do not perform re-slicing of the 3D dataset and perform sequential sampling steps as outlined above.

4.2.3 IMAGE PROCESSING AND MORPHOMETRIC ANALYSIS

Acinar segmentation was performed using the algorithms previously outlined in chapter 3. Acinar volume was calculated by multiplying the voxel count in the binary segmentation mask with the 3D voxel size (2x2x2 μm^3). The segmentation mask was also used to generate a surface mesh using a marching cube algorithm (45). The surface was smoothed using a size-preserving algorithm (93). The alveolar surface area was calculated as the sum of all triangles in the surface mesh.

Morphometric analysis was carried out using the skeleton-based approach that has been previously outlined in Chapter 3 (39). The lengths, diameters and branching angles for each branch were determined. Additional parameters that were computed include number of terminals, total path length to each terminal node and histogram of branches in each acinus grouped by generation as calculated from the entrance to the acinus. All computational analysis was performed on MATLAB (Mathworks Inc., Natick, MA).

4.2.4 STATISTICAL ANALYSIS

Two-way Analysis of Variance (ANOVA) tests were used to compare each morphometric measure across central and surface acini with the generation number as the second variable. In order to reliably compare acinar measurements across specimens, the statistical analysis was repeated after normalization by total lung length (as measured from apex to base from the ex-vivo LFOV microCT image). Independent two-sample t-test was used to test for significance in acinar volume across central and surface acini, before and after normalization by total lung volume.

4.3 RESULTS

The 3D structure of a surface and central acinus each, along with their anatomical location in the lung and their centerline skeleton are shown in **Fig.19.** Through direct visual inspection of the 3D rendered acini, we observed distinct differences in the structure of acini depending on their location within the lung. A flattened radial-tree representation of the acinar branching structure, for one central and surface acinus each, is shown in **Fig.20 A** and **B** respectively**.** The entrance to the acinus is enlarged and presented at the center. The radial distance from the center represents an increase in the generation number of the acinus. In the examples shown in **Fig.20**, branches in the surface acinus extend to a maximum of 9 generations, while branches in the central acinus extend to a maximum of 8 generations.

The mean total lung volume was 1,099 ± 143 mm^3. This is comparable to the lung volumes reported in the C57Bl/6 mice fixed at identical pressures of 20 cmH_2O (97) and in A/J fixed at pressures comparable to the current protocols (15 cmH_2O, 30 cmH_2O) (84,

85, 91, 94). The volume of surface acini extending to the pleural surface was significantly greater than that of central acini contained in deeper parts of lung parenchyma (0.27 ±0.02 mm^3 vs. 0.16±0.05 mm^3 respectively; P = 0.01). Normalization by total lung volume did not affect statistical significance. . Dividing total lung volume by average acinar volume, we estimated average number of acini per lung at 5510±371 acini.

Similar to acinar volume, the average alveolar surface area of a surface acinus was significantly greater (13.4 ± 2.43 mm^2 vs. 10.8 ± 1.4 mm^2; P = 0.01), suggesting that the larger volume is not related simply to higher compliance of surface acini but has a structural basis. The surface-to-volume ratio showed no significant difference between the two regions of interest (56.3 ± 6.98 mm^{-1} in central acini vs. 49.5 ± 9.4 mm^{-1} for the old mice).

The diameter of the alveolar ducts ranges from 148 ± 10.49 μm at the transitional bronchiole to 68 ± 11.38 μm at the most distal generation in surface acini and from 115 ± 2.72 μm to 63 ± 4.32 μm in the central acini. The variations in branch diameters are shown in **Fig 21A**. Surface acini have significantly larger branch diameters at every generation except at the last generation (P<0.01). There were no statistically significant differences in branch lengths in the sequential generations between surface and central acini, even though there appeared to be a tendency towards longer segments in most generations, as evidenced by the branch length distributions by generation shown in **Fig 21B**.

The average branch histogram for central and surface acini, computed as the average number of branches per generation, is shown in **Fig. 22**. For the first few generations, all acini follow the power law; with exponential increase in number of

branches due to dichotomic branching as long as there is no break-off (see **Fig. 22**). In surface acini, this increase continues for two generations more than in central acini, leading to a larger number of branches. All surface acini were found to have alveolar sacs that extended to 9 generations while most central acini terminated at the 8^{th} generation. Only two central acini were found to extend to the 9^{th} generation. The higher branch count and generation numbers account for the increase in acinar volume and increase in total path length observed in surface acini. Histograms of percentage distribution of path lengths in central and surface acini are shown in **Fig.23**. The Mean longitudinal path length L_p, was found to be greater in surface acini when compared to central acini (448.48 ± 76 µm vs. 369.9 ±60 µm, P = 0.01). A statistical summary of the path lengths in central and surface acini is shown through a Box and Whisker plot in **Fig. 24**. Terminal nodes in surface acini span a wider range of path lengths with the shortest paths comparable to measurements found in central acini. The branching angles were not found to vary significantly between surface and central acini and are presented in **Table 2**.

4.4 DISCUSSION

The morphometry of the conducting airways in mammalian species is well documented (28, 66, 72, 78, 79, 95, 102). While heterogeneity in airway morphometry plays an important role in ventilation heterogeneity and gas exchange, the available experimental data are increasingly incomplete near the respiratory zone (i.e. acini), which form the entrance to the acinus in mice.

Newer mathematical models of acinar structure incorporate the heterogeneous nature of the alveolar ducts within the acini (41-43) from available experimental data and

seek to better assess the relationship between anatomical structure and respiratory function (14, 23, 72, 75, 76, 89). With these increasingly accurate models, there is a need for characterization of inter-acinar heterogeneity across regions of interest in the lung. Previous studies by McDonough and colleagues (49) have shown evidence for heterogeneity in alveolar density based on lung height in humans. In rats, Zeltner and co-workers (114) have demonstrated regional differences in apex vs. base and in sub-pleural vs. central lung regions. Haefeli-Bleuer and Weibel (23) have previously commented on the differences in acini located in the pleural regions vs. central lung regions, readily apparent in the shape of the acinus. In the current study we have observed (see example in **Fig.4**) that, on average, all central acini are isotropic and near-spherical in shape, while surface acini have a fan-shape orientation with branches extending from the terminal bronchiole to the pleural surface. These structural differences between core and surface acini can be compared to the compact fractal nature of a cauliflower floret and the fan-like structure of a broccoli floret respectively.

The estimate of the total number of acini in this study is comparable to previous estimates of acinar count (3, 42) in rats and C57Bl/6 mice respectively. On average, we find that surface acini have increased volumes through an increase in alveolar duct diameters and total number of branches, without any significant change in segment lengths. In this study, the difference between surface and central alveolar duct diameter decreased in the more distal alveolar duct generations. Previous studies on C57Bl/6 mice (39) and rats (72) have shown similar results with the convergence of diameters at the terminal alveolar sacs across age groups. The generations furthest from the acinar entrance are comprised of alveolar sacs and the convergence of the distal diameters of

both the central and surface acinar alveolar ducts indicates that the alveolar sacs and individual alveoli have similar geometry in both surface and central acini. In addition, we observed that the alveolar sacs, which form the terminal nodes, extend further from the acinar entrance in surface acini when compared to central acini, i.e. the total path length is longer in surface acini. The increased longitudinal path length in surface acini represents the greater average distance traveled by inhaled gas or particles to reach the most distal alveoli. Given the diffusive nature of gas transport within acini, this heterogeneity in acinar structure becomes important in computational modeling of gas exchange (14, 76, 89).

The surface acini have increased alveolar surface area in comparison to central acini. However, the surface-to-volume ratio was not significantly different between the two groups. This suggests that there is no difference in the geometry of the alveolar ducts with the corresponding alveolar sleeve.

The statistical evidence indicates that there are significant differences in acinar shape and geometry between pleural and central regions of the lung. This heterogeneity suggests that care should be taken when extrapolating the results from assessment of surface acinar and alveolar measurements to represent the whole lung, especially in applying the dynamics of pulmonary physiological processes and in the development of numerical models to represent the lung. The in-vivo IIBH protocols, fixation techniques and high-resolution interior tomographic imaging presented in this chapter, in accordance with the guidelines set up in the ATS/ERS Task Force report, allow us to perform unbiased characterization of the murine pulmonary acinus. The techniques set forth allow us to perform efficient studies to evaluate and characterize the heterogeneity in acinar

morphometry in normal and diseased lungs. The evidence for heterogeneity in central and surface acini has been presented and is indicative of a need for greater investigation across different anatomical regions of the lung.

Generation from entrance to acinus	Central Mice Mean (SD) in degrees	Surface Mice Mean (SD) in degrees
1	102.34(2.81)	116.09(16.37)
2	99.24(24.11)	99.92(11.82)
3	106.32(28.13)	105.13(32.52)
4	102.81(26.95)	102.55(31.95)
5	106.37(15.36)	103.68(27.74)
6	99.92(11.82)	106.32(28.13)
7	105.13(32.52)	106.32(28.13)
8	102.55(31.95)	102.81(26.95)
9	103.68(27.74)	106.37(15.36)
10*	106.32(28.13)	99.92(11.82)

Table 2: Generation based estimates of branching angle in Surface and Central acini

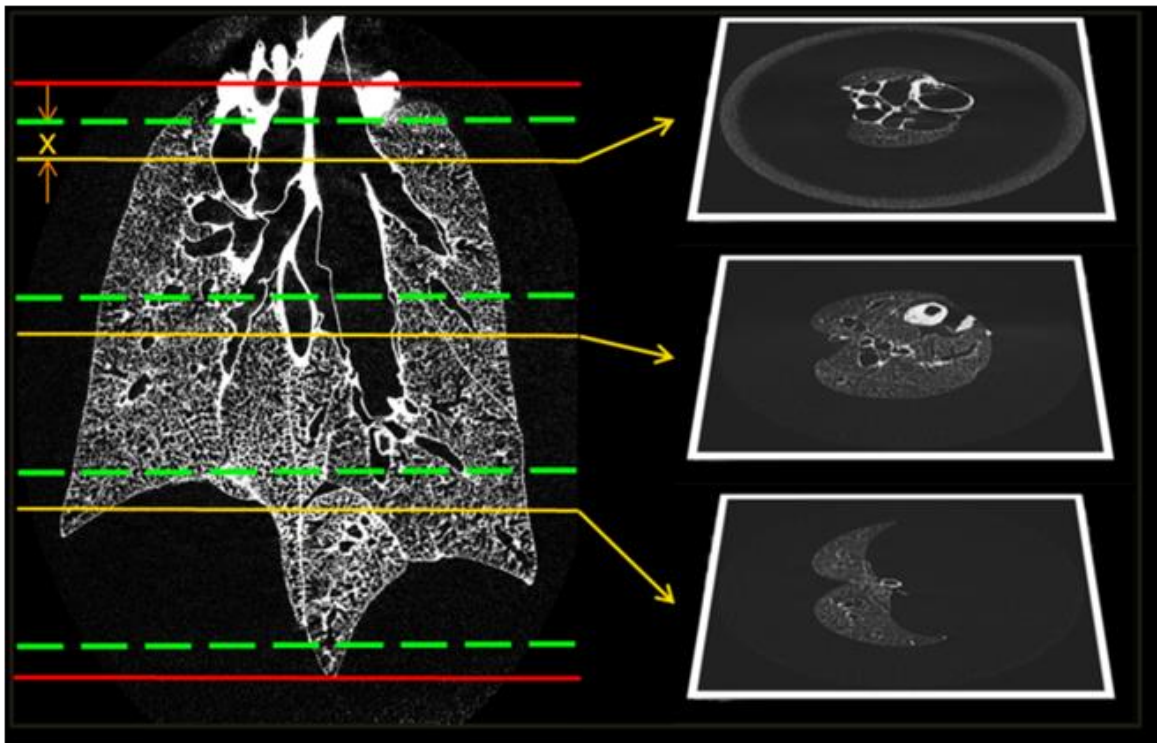

Figure 16. Stage 1 of the systematic uniform random sampling process. The red lines indicate the limits of the lung. The slices suitable for sampling are divided into 3 stacks. The green lines represent the stack boundaries. A random offset 'x' is applied identically to each block to select slices as shown above. The sampling reduces the dimensionality of the data from a 3D volume to a set of 2D slices. The selected slices are then subjected to the next stage of sampling.

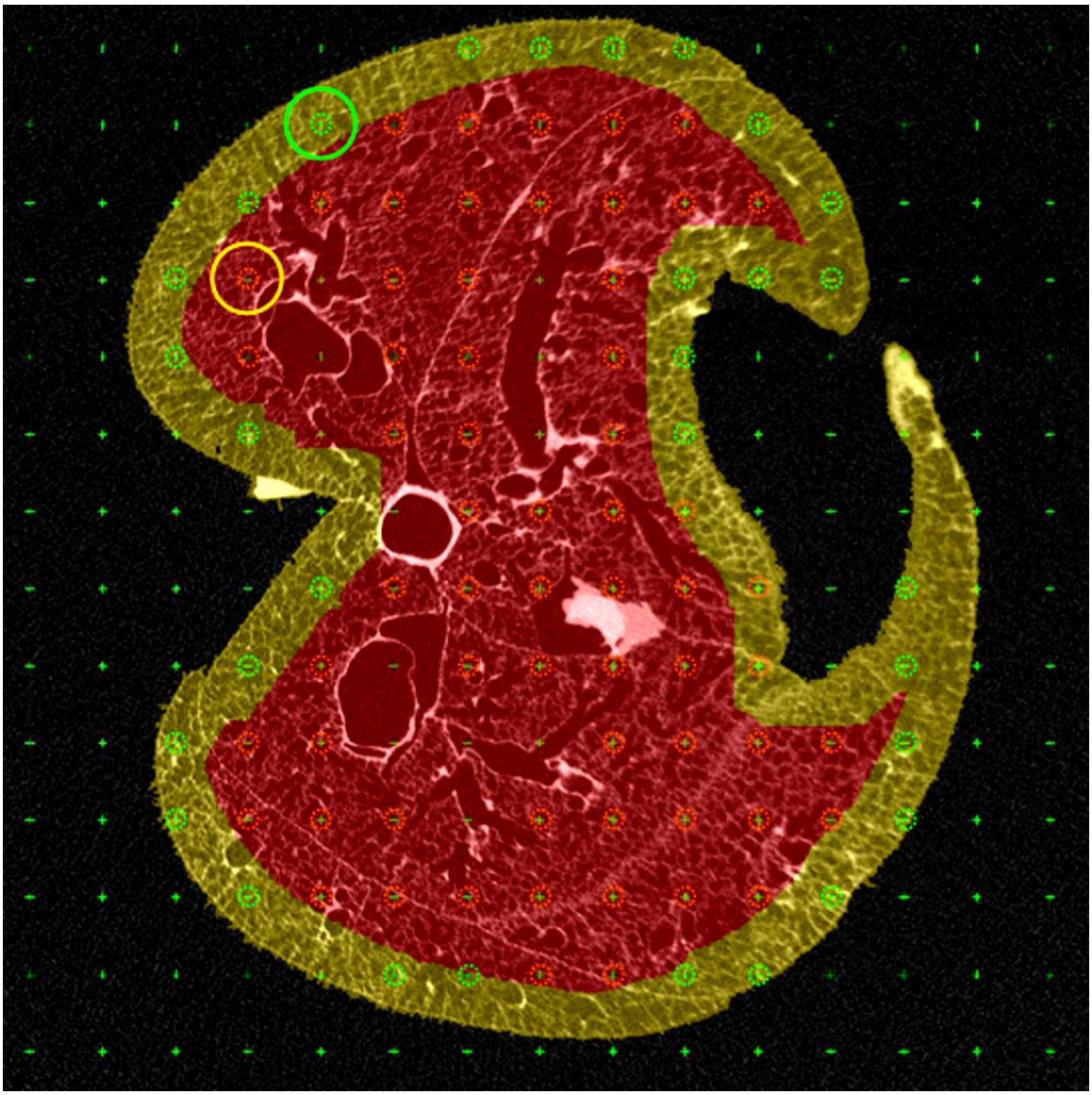

Figure 17. Demonstration of ROI based sampling. The masks used to separate the central and surface acini are depicted in red and yellow respectively. A grid is overlaid on the 2D slice (the intersection points of the grid are indicated by a green cross), and the points that fall within the respective lung masks are eligible for selection. All points that fall on large airways or the blood vessels are eliminated. The points eligible for central and surface sampling are depicted in red and green circles respectively. The random point chosen for each example and its un-adjusted circular FOV are also depicted.

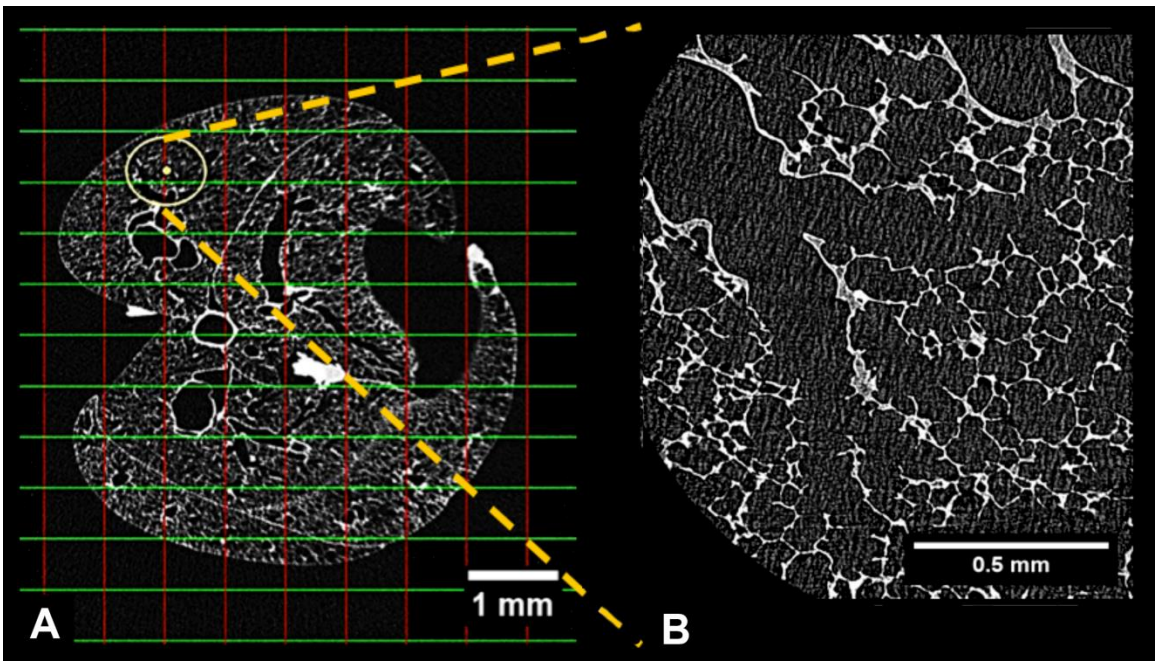

Figure 18. Example of shifted FOV and corresponding HRES image. The circle in Fig.19A represents the field of view of the HRES image at the new shifted coordinate. The center of the FOV has been manually shifted from the nearest grid intersection in order to ensure that the selected acinus is completely within the FOV. The high resolution image corresponding to the highlighted FOV is shown in Figure 19B.

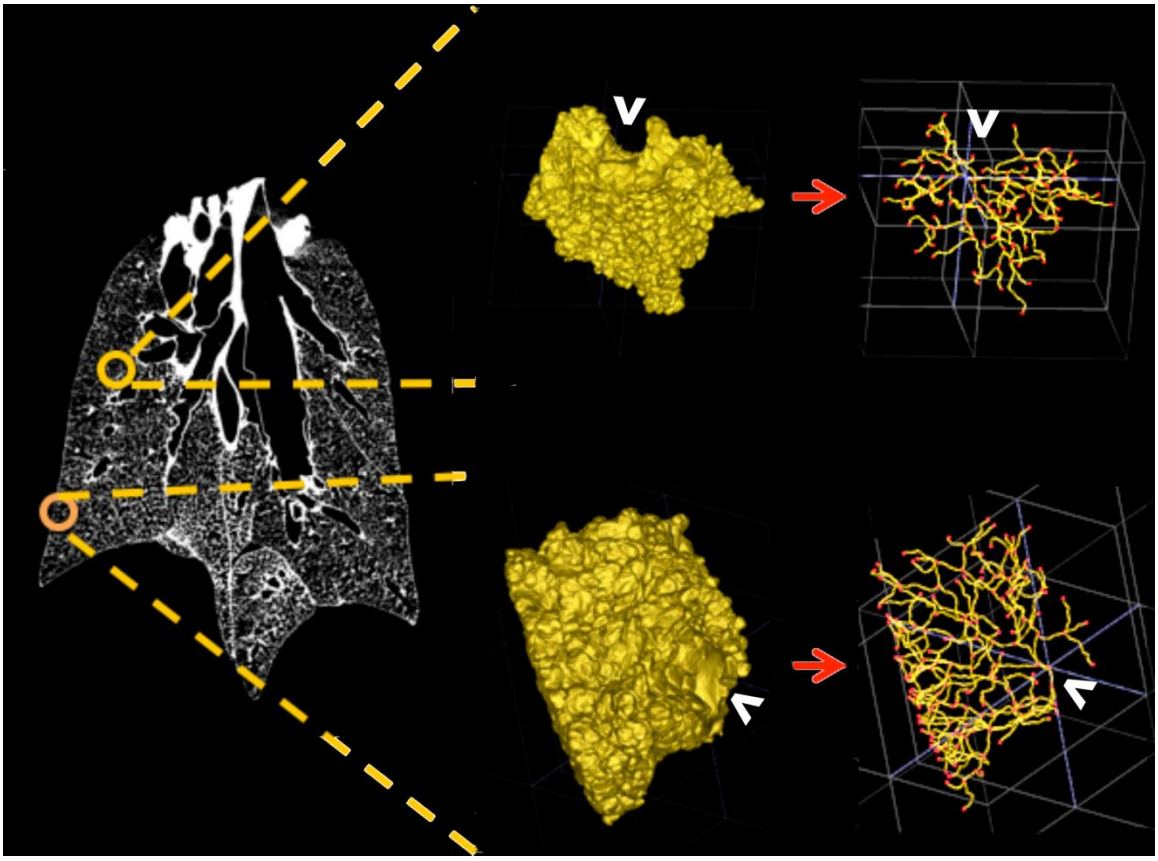

Figure 19. Sampling of surface and central acini, with the 3D rendered acinus and the respective center-line trees used for morphometric analysis. Central acini extend isotropically while surface acini have branches "fanning" towards the pleural surface. The white arrows indicate the entrance to the acinus.

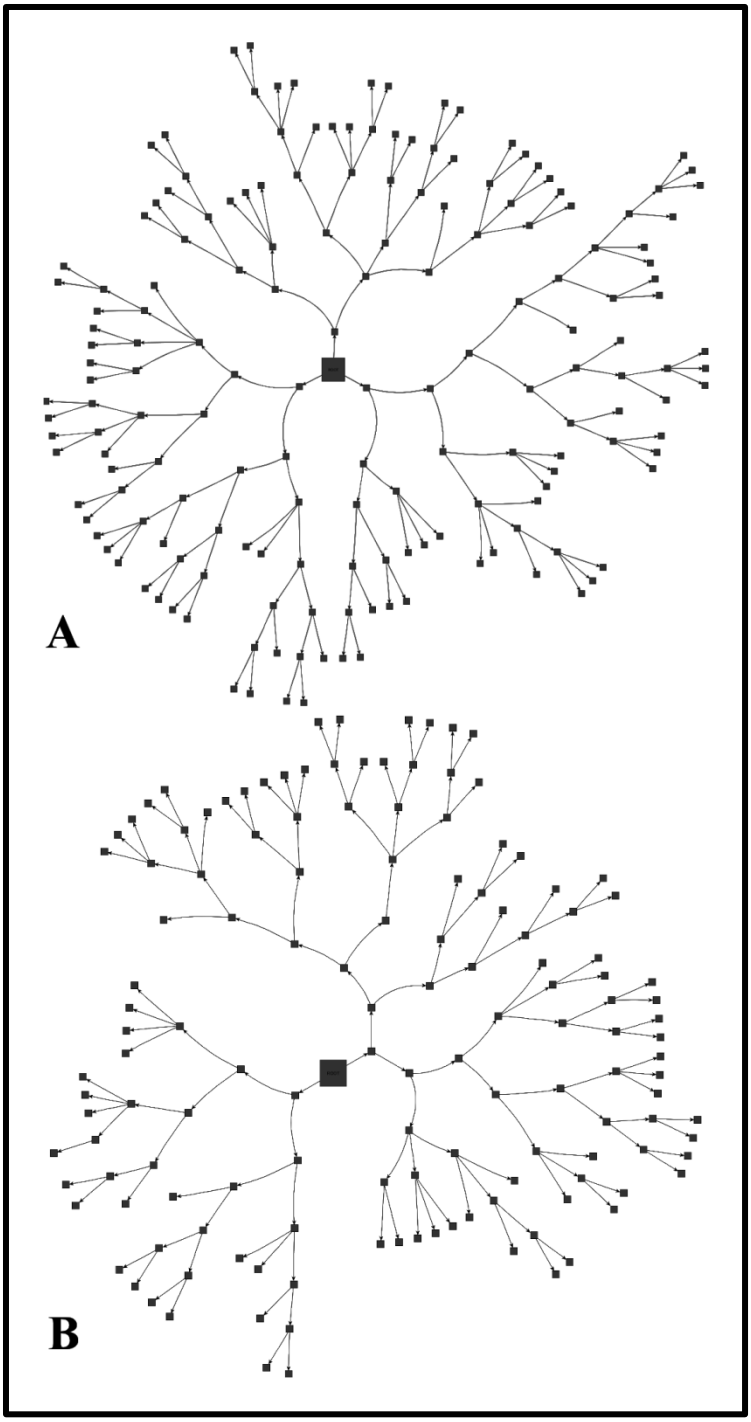

Figure 20. Schematic representation of the acinar branching structure. A and B show the branching structure for one central and surface acinus respectively. The branches are not to scale, but represent an example of the acinar branching pattern. The entrance to the acinus is enlarged for better visualization.

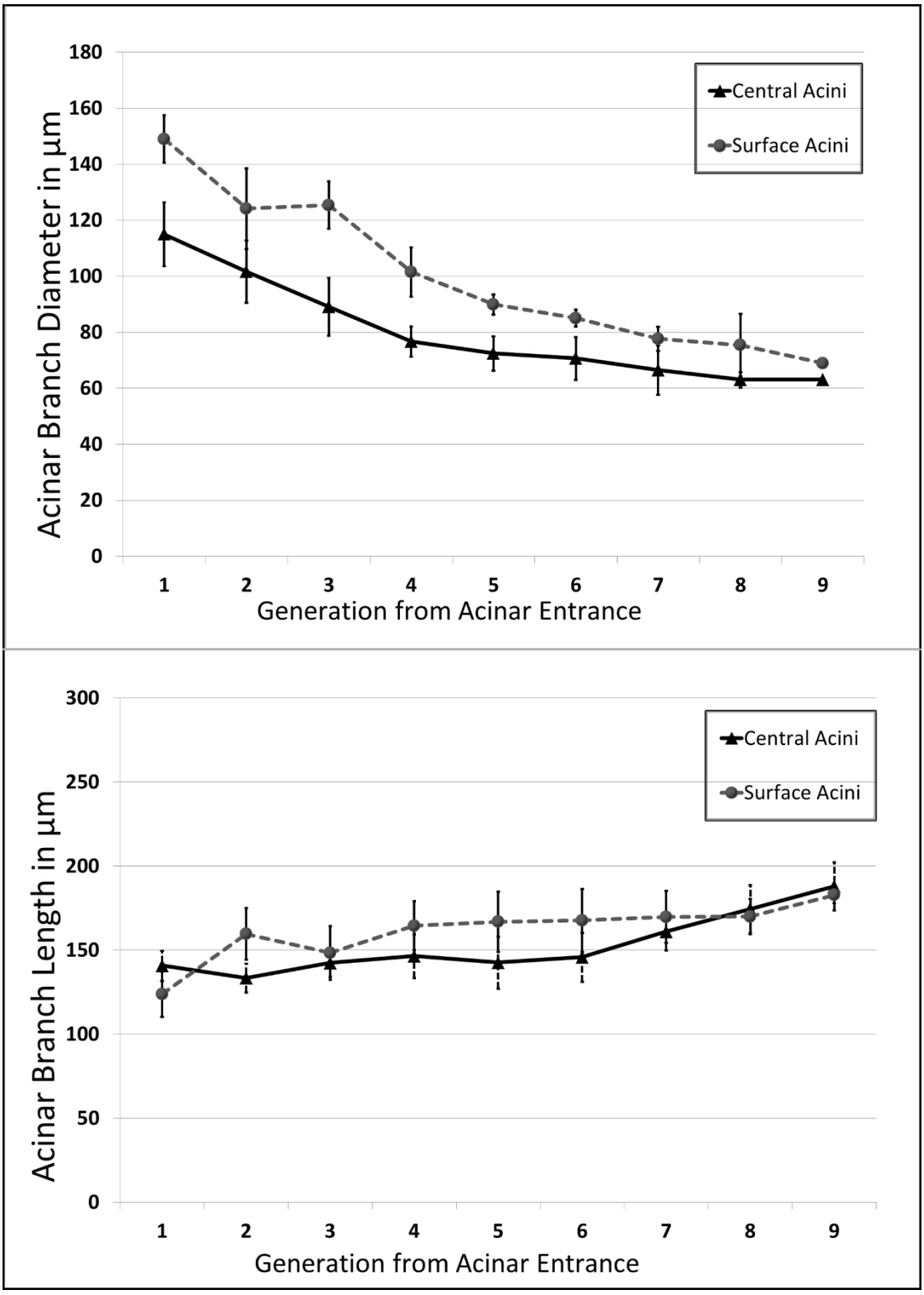

Figure 21. A, B - Variations in acinar branch diameters and branch lengths respectively across central and surface acini. Measurements are averaged by generation. The difference in diameters between surface and central acini are diminished near the terminal nodes, indicating that the alveolar sacs are similar in size. There are no significant differences in branch lengths between central and surface acini.

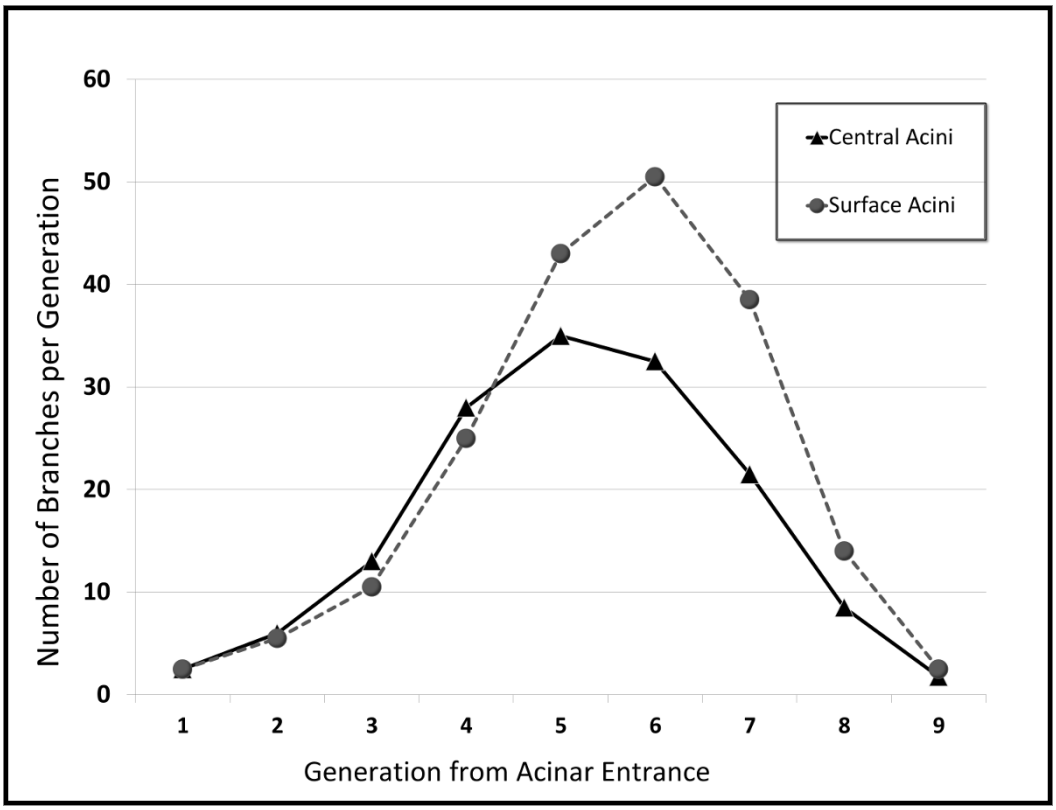

Figure 22. Histogram of number of acinar branches categorized by generation number. The branch histogram follows the power law for the first 4-5 generations. Surface acini have increased number of branches, especially in generations 5-7.

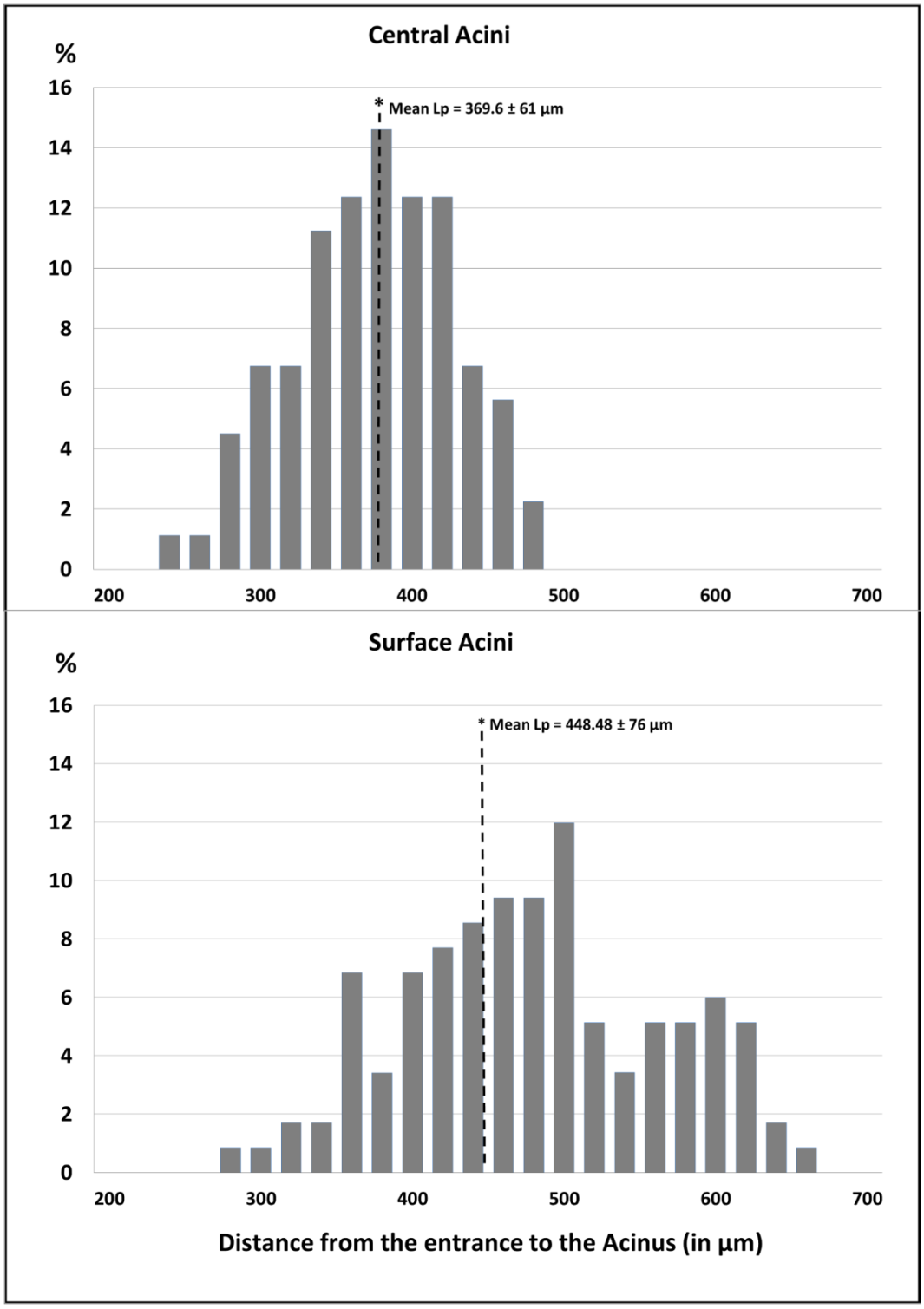

Figure 23. Distribution of path lengths from acinar entrance to terminal alveolar sacs in central and surface acini. The y-axis represents the percent contribution to the total longitudinal path length from each generation. The x-axis represents the distance from the entrance to the acinus in µm. Bins of 20µm width have been used to group the measurements for a histogram representation. The mean longitudinal path 'Lp' in surface acini are greater than in the case of central acini.

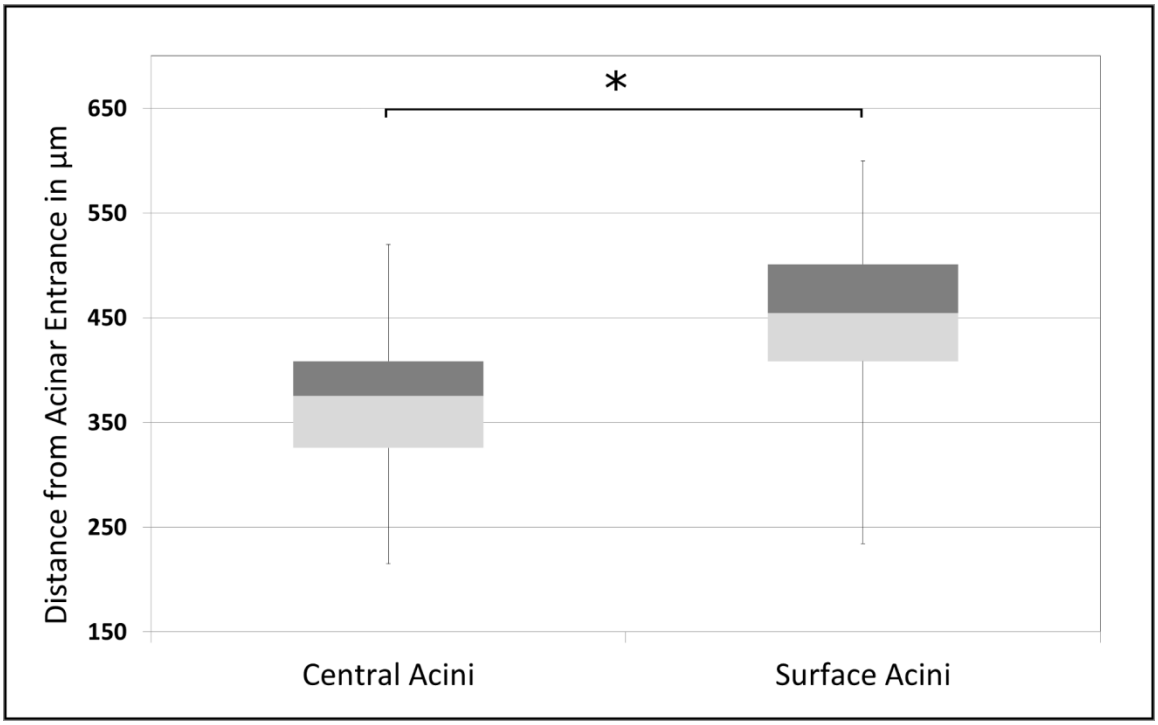

Figure 24. Box and Whisker plot showing the minimum, first quartile, median, third quartile and the maximum path lengths from acinar entrance to a terminal node in surface acini compared to central acini. On average, surface acini have increased path lengths, greater number of terminal nodes and a wider range in total path length.

CHAPTER 5. NORMATIVE METRICS OF ACINAR PHENOTYPES FOR THREE COMMON STRAINS OF MICE

5.1 INTRODUCTION

Animal models for human disease form the basis of fundamental research in medicine. Mouse models are widely used in research into pathophysiology, especially in the pulmonary domain (12, 32, 82). Data from the Mouse Genome database and the Mouse Tumor databases allow researchers to explore the gene-phenotypes relationships (4, 13, 83) and assess the viability of translating research to human pathology. Inbred mouse strains have known genetics and the resulting phenotypic characteristics can be used to analyze important pulmonary pathophysiology associated with specific disease states such as hypoxia, pulmonary embolisms, emphysema, and cystic fibrosis (17, 18, 56, 57, 100). The mapping of the genome allows for the creation of gene-knockout models that can serve as models for pre-clinical trials and drug development. Three strains commonly utilized in research as a baseline for subsequent genetic manipulations are the C57BL/6, A/J, and BALB/c mice. These strains are extensively used in pulmonary research, such as in toxicology studies assessing response to inhaled particulate matter and pharmacokinetic response to spasm-inducers (15, 61). Such studies have relied on the assessment of respiratory function and mechanics via traditional tools such as pulmonary function testing to estimate airway resistance, lung elastance and compliance in addition to postmortem histology. Observed variations in response between strains can be attributed to genotype changes between the strains leading to differences in metabolism and tissue sensitivity (15). However, potential differences in the underlying anatomy of the lung in the upper airways and acinar airspaces can result in modified airflow distributions and lead to differences in respiratory function. An improved understanding

of the normal anatomy of these strains becomes paramount in decoupling the anatomical sources of variations from the observations in pathology.

Imaging techniques such as microCT have allowed for the characterization of the phenotype variations in these three strains via in-vivo microCT imaging (94), allowing for the characterization of the gross characteristics such as lung and lobe volumes, along with the characterization of the upper airway tree. These results have provided an ideal starting point from which we can expand phenotyping through the high-resolution imaging methodologies put forward in this thesis. The assessment of the acinar airspaces (with regional sampling), allows us to perform morphometric comparison of the acini in the three strains, generating an extended atlas of the airway tree, assessing how central airway structural differences propagate into the lung periphery

5.2 METHODS

5.2.1 SAMPLE PREPARATION

Six mice from each strain were used for this study (C57BL/6, A/J and BALB/C strains, Jackson Laboratories, 15- 20 weeks of age). The animals were housed in an animal facility at the University of Iowa. All experiments and protocols were performed subject to approval by the Institutional Animal Care and Use Committee (IACUC) at the University of Iowa. The C57BL/6 and A/J specimens are the same as presented in chapters 3 and 4. The BALB/C specimens were prepared and imaged in-vivo similar to the A/J specimens, with minor changes in the sampling methodology, detailed below.

5.2.2 ACINAR SAMPLING AND SCOUT BASED IMAGING

The SUR sampling process detailed in Chapter 4 was repeated for the BALB/c specimens with one change in the final step involving coordinate selection. In collaboration with Dr. Ewald Weibel, we have incorporated a third stage of sampling in our protocol, further extending the systematic nature of the sampling paradigm.

The initial steps (1- 5) of the sampling process are followed identically for the new strain, resulting in a set of 2D slices. The third stage of sampling is applied at the point of coordinate selection and follows the smooth fractionator principle (19-21) applied in the previous stages. All grid intersection points that fall within the ROI mask (from each sampled slices) are added to a set of eligible points. The set of eligible coordinates is divided into stacks based on the planned number of final coordinates. A random offset, similar to the slice offset in the 3D sampling step, is used to select a single point from each stack. These points are equidistant in the stacks and provide the new coordinates for HRES imaging. **Fig.25** shows a representation of the stacked coordinates and the fractionator principle used to sample the coordinates. The exact coordinate is shifted to ensure that the sampled acinus is completely within the HRES field of view. Image processing and acinar analysis is carried out as previously outlined for the other two strains. A side by side comparison of the three strains is shown in a grid representation in **Fig.26.** Each column represents a particular strain, from left to right: C57Bl/6, A/J and the BALB/c strains. The first row of the image shows a 3D rendering of the lung acquired via in-vivo imaging at a baseline of 20cmH_2O. The second row contains examples of a HRES image with the terminal bronchiole feeding an acinus in the

slice presented. A 3D rendering of the acinus corresponding to the HRES image and the respective center-line skeletons are shown in rows 3 and 4 respectively.

5.2.3 STATISTICAL ANALYSIS

Two-way Analysis of Variance (ANOVA) testing (with generation number and strain as the independent variables) was used on the morphometric measurements to look for statistically significant variations between the three strains groups and between generation numbers. Two-way ANOVA testing was repeated after normalizing the data by lung height to account for any bias due to size when comparing the three strains. Pairwise mean comparisons between strains were carried out with the p-values adjusted using Bonferroni's method to account for the number of tests performed (3 pairwise comparisons at each generation).

5.3 RESULTS

The acinar branching patterns for the three strains are illustrated via a flattened radial tree representation in **Fig.27**. Pairwise comparison showed significant differences at the first 4 generations between the C57BL/6 inbred strain and both the A/J and BALB/c strains. **Fig.28** and **Fig.29B** show the variations in branch lengths and branch diameters respectively. The C57BL/6 strain was found to have significantly smaller (adjusted $p < 0.05$) branch diameters and branch lengths compared to both the A/J and BALB/c strains. The differences were progressively reduced with increase in generation number from the acinar entrance. The distal generations did not yield any significant differences in branch diameter or length. Addition of upper airway diameters from Thiesse et al. (94) allow us to compare the differences in airway morphometry of the

three strains at the conducting and respiratory airspaces. The variations in upper airway and acinar branch diameters are shown in **Fig.29A**. The C57BL/6 strain was found to have significantly larger upper airway diameters; however, there is a reversal in this trend with the same strain having significantly smaller acinar diameters in comparison to the other two strains. The average acinar volume of the C57BL/6 was significantly different ($p < 0.05$) compared to the A/J and BALB/c strains (0.18±0.02μm3 in C57BL/6 mice vs. 0.25±0.05 μm^3 and 0.24±0.06 μm^3 in A/J and BALB/c mice respectively). There were no significant differences observed between the A/J and BALB/C strains for branch diameters or branch lengths. In both A/J and BALB/C specimens, all acini were averaged to compare against the C57BL/6 data due to a lack of ROI based sampling for the C57BL/6 strain. No statistically significant differences were observed in the distribution of branching angles between any of the strains. The branch histograms were not found to vary significantly between the three strains and are shown in **Fig.30**. The branch count follows power law for the first 4 – 5 generations on average for all three strains. The distribution of the longitudinal path length measured from the acinar entrance for each of the three strains is shown in **Fig.31**. The mean longitudinal path length represents the distance from the acinar entrance to the terminal alveolar sacs and was found to be significantly smaller ($p<0.01$) in C57BL/6 mice (Lp = 347.39 ± 73.96 μm) compared to the other two strains (409.185 ± 68.4 μm and 418.082 ±84.93μm in A/J and BALB/c mice respectively). A summary of the branch morphometric measurements for the three strains are shown in Table 3, with an asterisk marking pairwise comparisons of statistical significance.

5.4 DISCUSSION

In this body of work, we have focused on the differences in the structural lung phenotypes in three of the most commonly utilized mouse strains. Using high-resolution imaging protocols, we have identified differences in the structural organization of alveoli and alveolar sacs across the three strains. An observation of note from the current data is that the differences in branch diameters and branch lengths are pronounced at the generations closest to the terminal bronchiole and disappear at the distal generations. In the pulmonary acinus, alveolar sacs start appearing after the 4-5 generations on average. The inclusion of these terminal sacs is one possible contributing factor for the reduced estimates of the branch morphometric parameters at the distal generations. The shape of the branch count histograms can also be attributed to the appearance of the alveolar sacs, leading to an exponential increase for the first 4 - 5 generations, followed by a reduction in branch count at the more distal generations. Thiesse et al. (94) presented data that characterized the upper airways of these three strains. The upper airway diameters from that study have been reproduced in Fig.23 in order to provide a comparative analysis to the acinar airways. This comparative analysis provides a significant point requiring further investigation. It has been observed that the C57BL/6 strain has larger upper airway diameters on average in comparison to the A/J and BALB/C strains. However, this trend is reversed in the acinar airspaces, where the C57BL/6 strain has the smallest diameters of the three strains. This implies a significant restructuring of the airway branching morphometry at the transition between the conducting and respiratory airways. There are pronounced differences in the diameters of the C57BL/6 airways at both measured scales in comparison to the other two strains. Previous studies have outlined

evidence of possible structural differences in alveolar size (84, 85) and in lung function (69, 81) across similar strains. Soutiere et.al (85) examined lungs for two of the strains presented in this work and identified that A/J mice have larger alveoli on average than C57BL/6 mice (38±2 vs 35±3 μm respectively). Similarly, Huang et al. (30), Schulz (81) and Reinhard (69) have investigated the change in lung mechanics across other strains and sex and concluded that there are significant differences in the age-dependent changes between strains. These results and other similar research provide a basis to conclude that there are architectural differences in the size and structure of pulmonary acini along with those previously assessed in the upper respiratory tract.

The current data provides a basis for further investigation into the structural phenotypes of the normal mouse and the need to assess the differences in airflow dynamics in these strains. Through the application of regional sampling to the C57BL/6 strain, we can further characterize the acinar structure by performing regional comparisons and identifying patterns in the architecture of the parenchyma. These phenotypes will allow us to develop improved gold standards to serve as control groups for comparison with mouse models of pulmonary pathology.

Generation from Entrance to the Acinus	C57BL/6			A/J			BALB/C		
	Mean (± SD) µm			Mean (± SD) µm			Mean (± SD) µm		
	Diameters	Lengths	Branching Angles	Diameters	Lengths	Branching Angles	Diameters	Lengths	Branching Angles
			Degrees			Degrees			Degrees
1	110.87(26.34)	93.94(11.79)	102.34(2.81)	131.95(30.48)	134.98(30.48)	116.09(16.37)	135.91(33.2)	128.55(26.55)	106.32(28.13)
2	87.29(13.08)	98.65(10.71)	99.24(24.11)	112.88(17.53)	129.13(17.53)	99.92(11.82)	116.43(11.52)	117.39(15.77)	106.37(15.36)
3	92.67(18.2)	95.6(10.68)	106.32(28.13)	107.03(34.07)	118.1(34.07)	105.13(32.52)	111.49(55.4)	115.78(22.25)	105.13(32.52)
4	81.97(50.16)	86.11(10)	102.81(26.95)	89.07(25.36)	107.73(25.36)	102.55(31.95)	97.97(30.27)	99.75(11.25)	102.55(31.95)
5	75.1(8.17)	80.02(9.88)	106.37(15.36)	81.19(22.5)	81.95(22.5)	103.68(27.74)	79.01(54.29)	79.56(14.7)	105.13(32.52)
6	69.08(20.55)	77.34(8.21)	99.92(11.82)	77.83(18.29)	79.85(18.29)	106.32(28.13)	71.6(23.27)	73.93(17.02)	99.92(11.82)
7	66.82(13.53)	78.47(7.89)	105.13(32.52)	72.04(28.14)	76.42(28.14)	106.32(28.13)	69.54(10.08)	74.2(21.56)	106.32(28.13)
8	62.99(50.25)	73.69(5.7)	102.55(31.95)	69.19(42.08)	72.4(42.08)	102.81(26.95)	73.57(26.54)	66.42(10.98)	102.81(26.95)
9	67.38(26.51)	82.11(14.3)	103.68(27.74)	68.91(7.26)	68.86(7.26)	106.37(15.36)	67.54(44.22)	66.85(19.96)	102.81(26.95)
10							68.56(5.49)	72.72(23.39)	99.92(11.82)

Table 3: Phenotype variations in Branch Diameters, Branch Lengths and Branching Angles across three common research strains

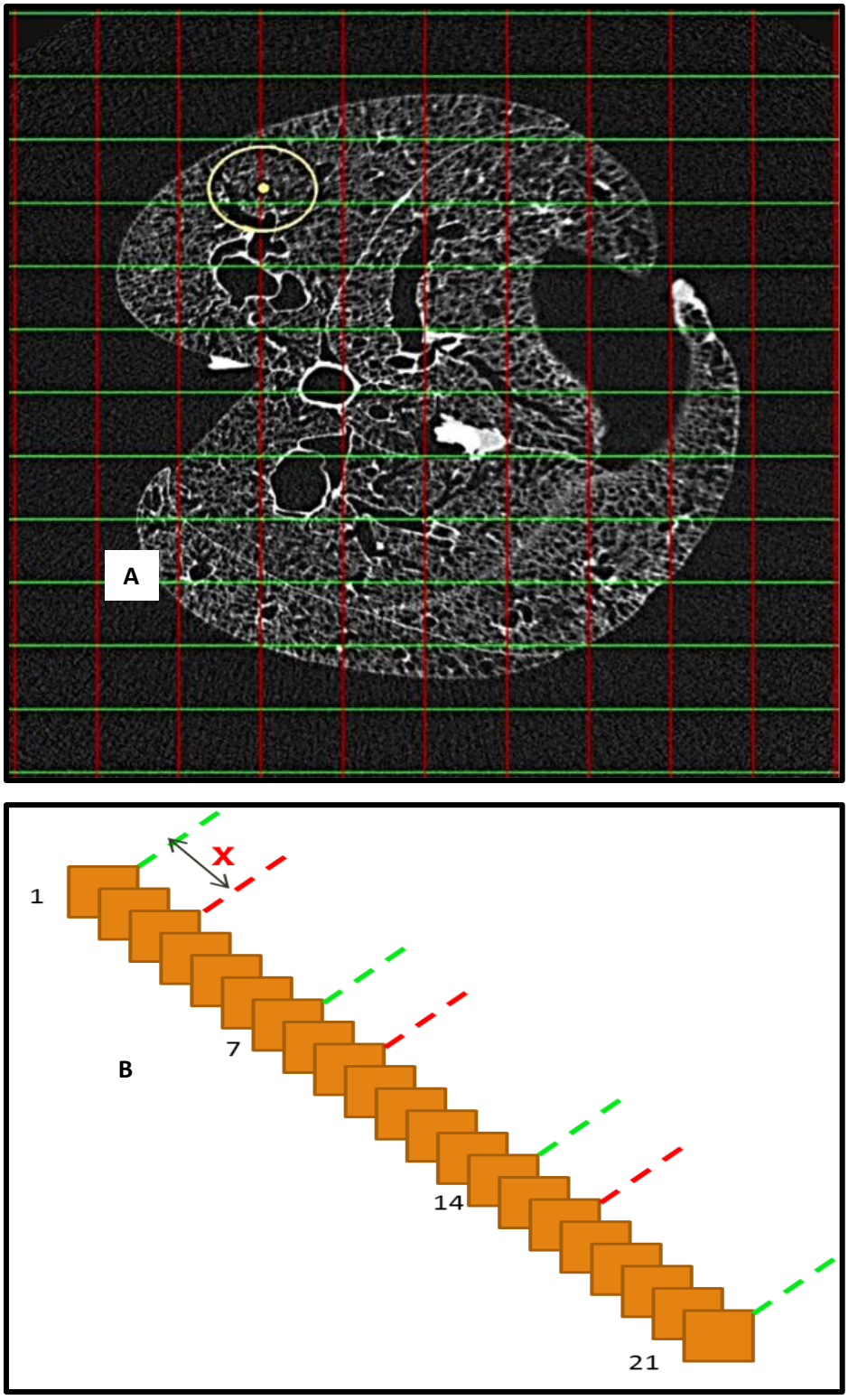

Figure 25. Third Stage of SUR sampling. The grid points chosen in figure A are sampled using random offset method. Figure B shows the application of a random offset 'x' to the list of all eligible points to select 3 coordinates for HRES imaging.

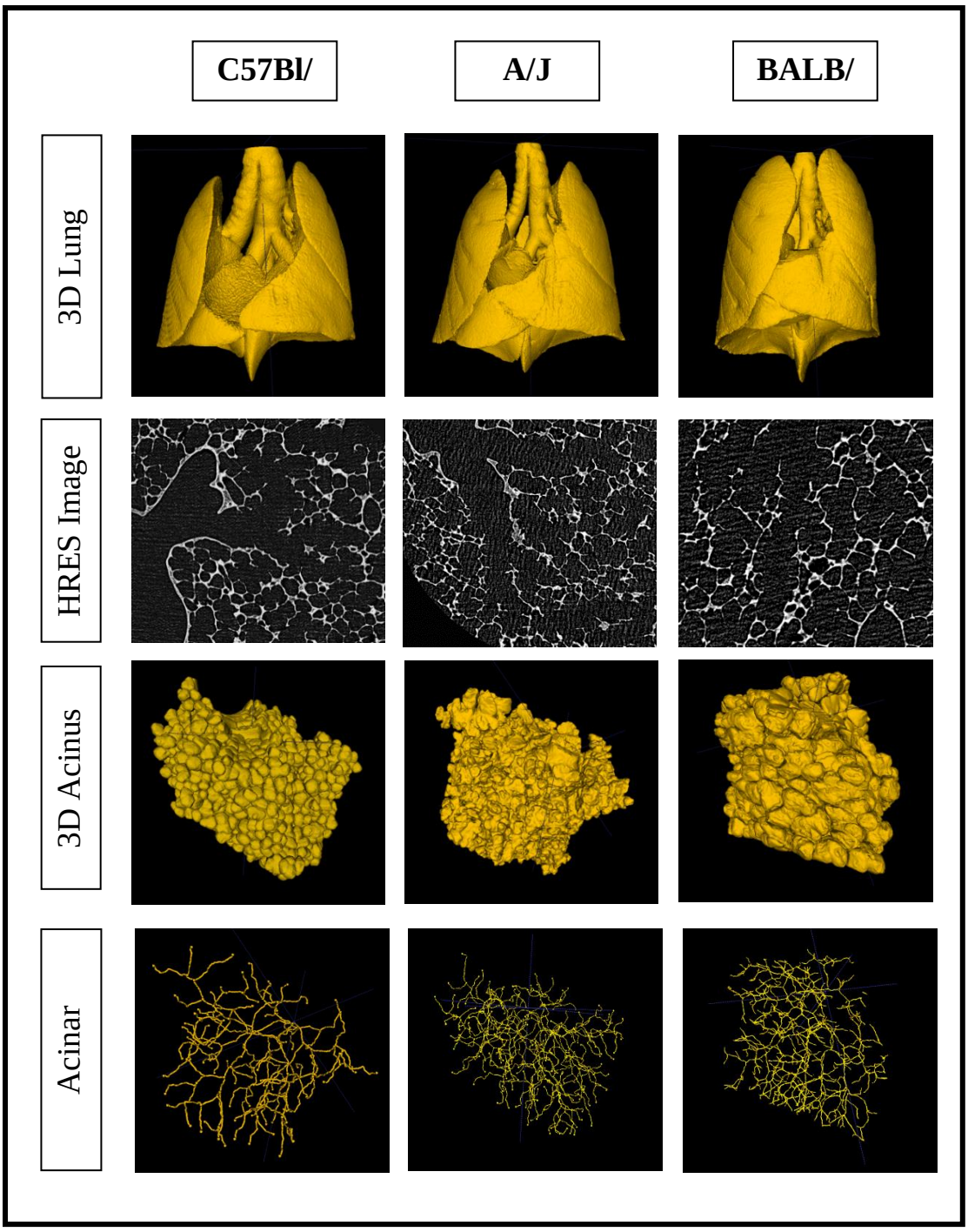

Figure 26. Illustration of the three strains. Columns 1 – 3 represent images from C57Bl/6, A/J and BALB/c strains in that order. Rows 1 – 4 depict the 3D rendered in-vivo volume, a sample HRES slice with the acinar entrance, the 3D rendered Acinus and the corresponding center-line skeleton in that order.

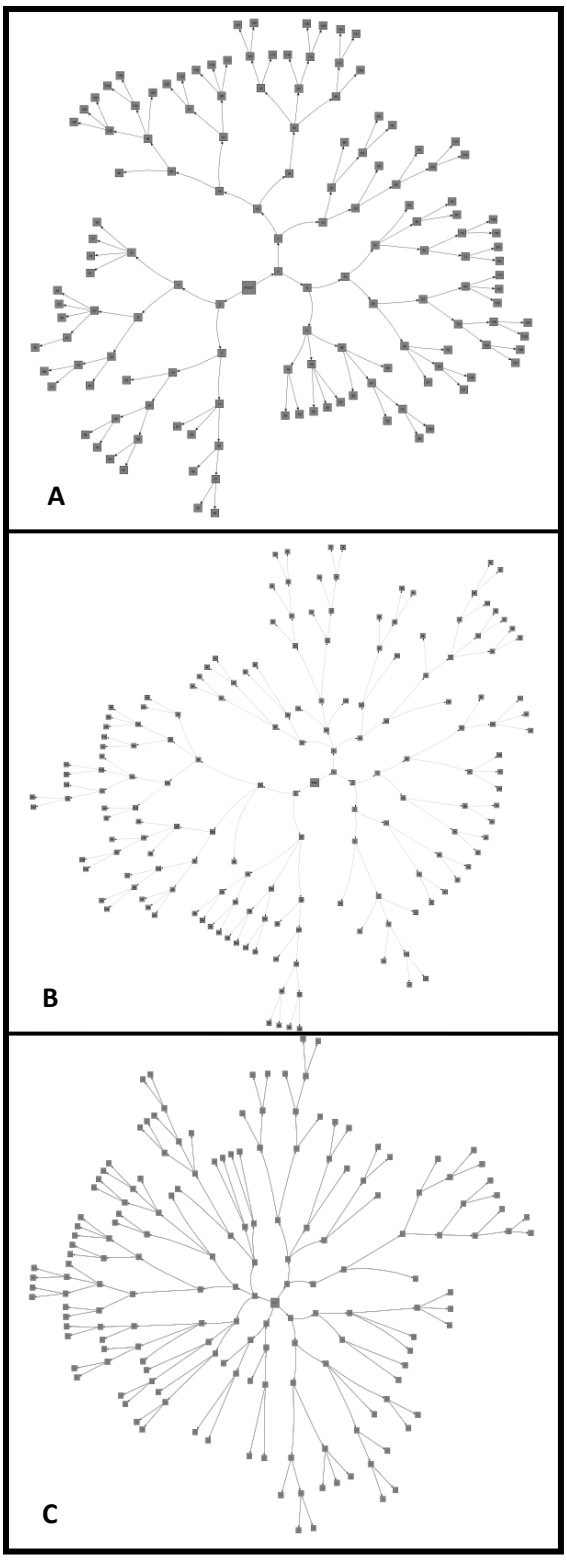

Figure 27. Flattened Radial tree Representations of the acinar branching structure. Figs. A, B and C show an example each of a branching pattern from the C57Bl/6, A/J and BALB/c strains respectively.

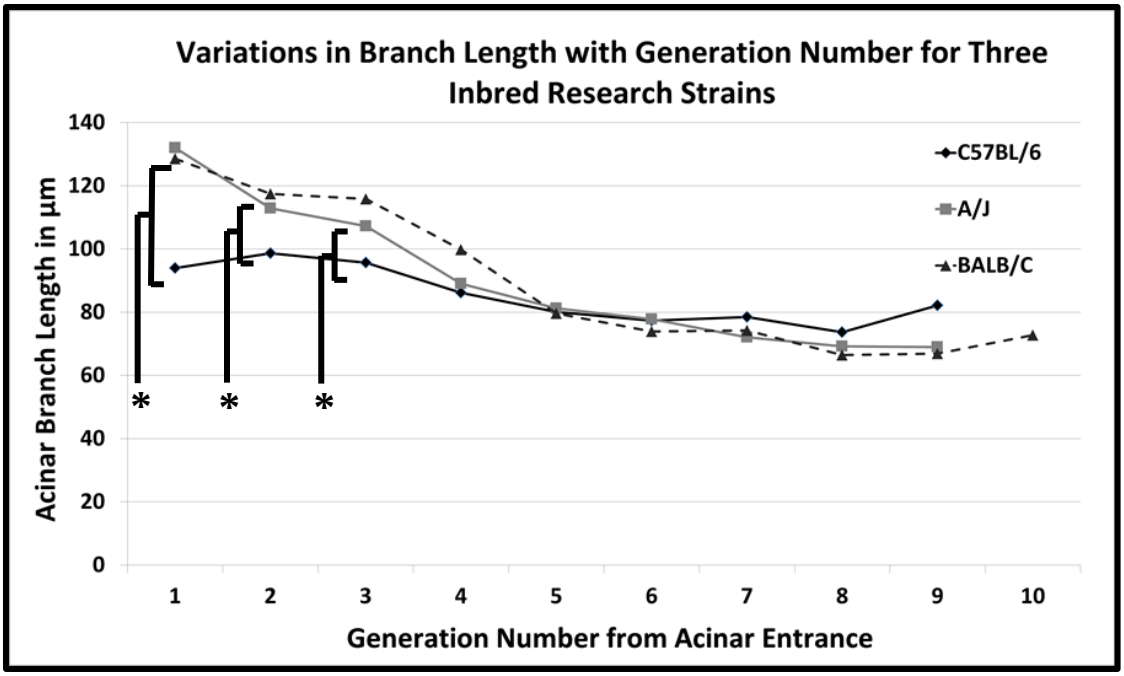

Figure 28. Comparison of Branch lengths across three strains. The C57bl/6 mice have significantly shorter branch lengths in comparison to both the A/J and Balb/C strains in the first few generations. At the higher generations, alveolar sacs start appearing, leading to reduced differences between the strains. Generations with asterisk denote statistically significant differences.

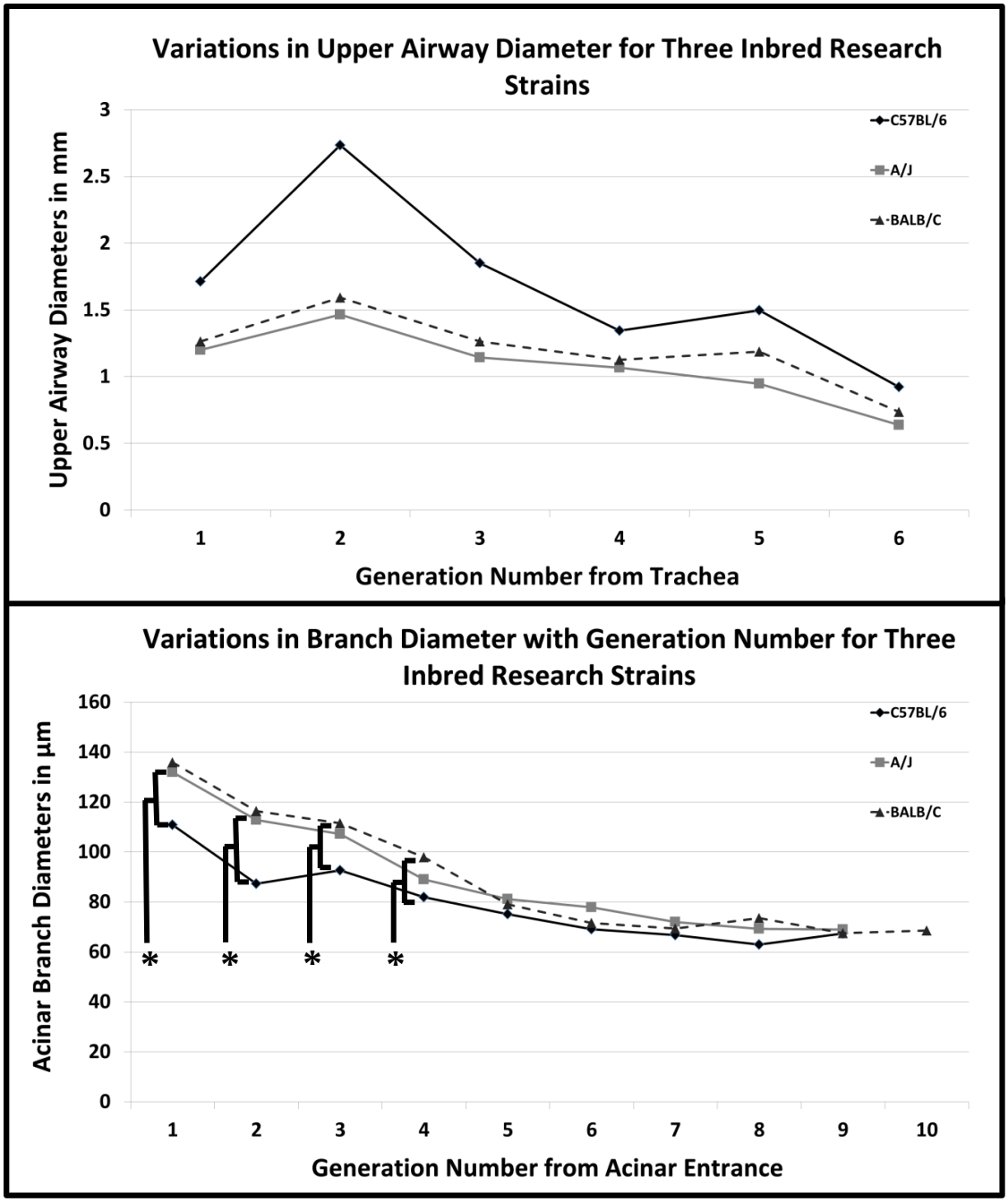

Figure 29. Comparison of Branch diameters in central and acinar airways across three strains. There is significant difference (adjusted p<0.05) in the branch diameters between the C57Bl/6 strain and the other two strains in the first few generations (denoted with asterisk) of the acinar airspaces similar to the results observed in branch lengths. The upper airway diameters are based on measurements presented by Thiesse et. al (94).

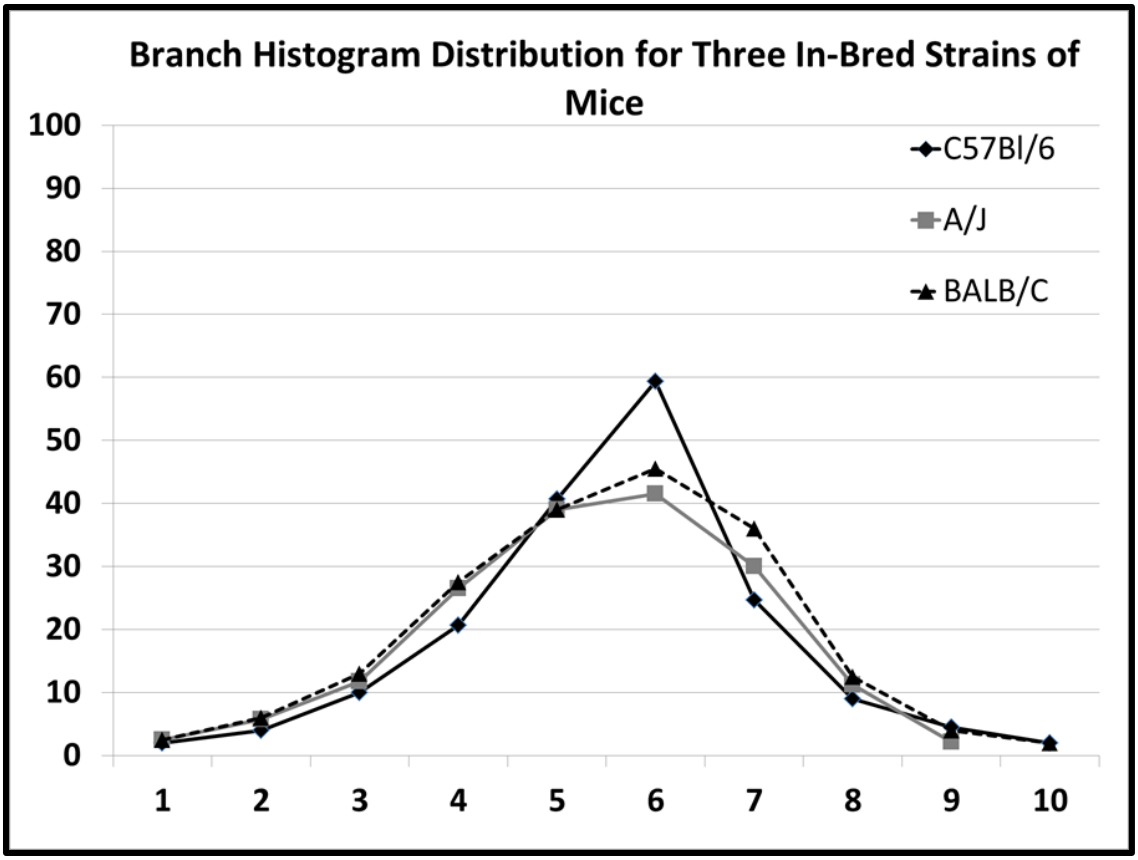

Figure 30. Histogram distribution of acinar branches based on generation number for the three strains. All the strains have similar distributions with no significant differences between strains. The branch histogram follows the power law for the first 4- 5 generations, at which point, alveolar sacs start appearing in the branching structure.

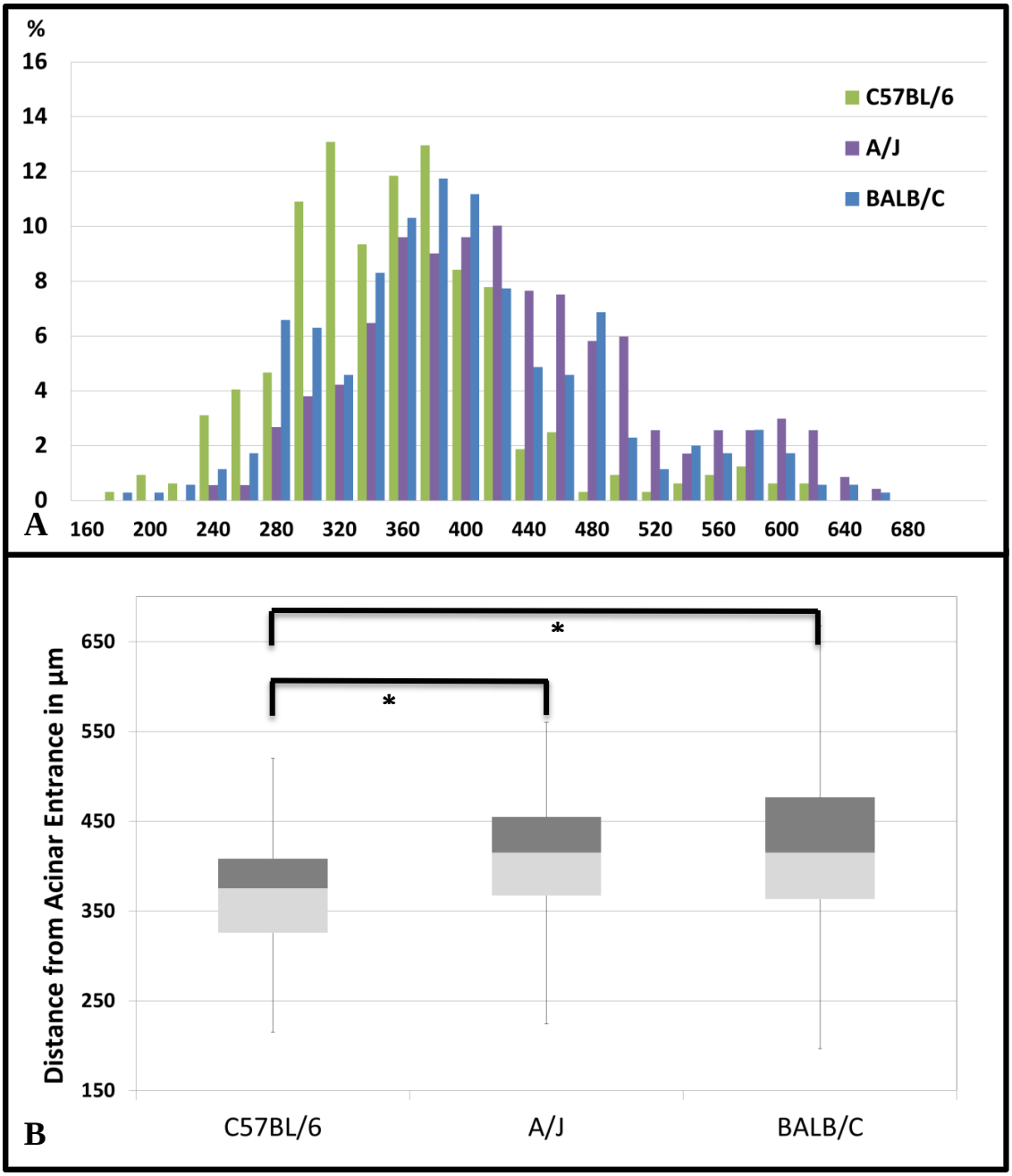

Figure 31. Distribution of longitudinal path lengths in the three inbred strains. 'A' shows the distribution of the longitudinal path length (distance from acinar entrance to alveolar sac) in acini from each strain. The mean longitudinal path length in C57Bl/6 mice is significantly shorter than in the other two strains. 'B' shows a Box and Whisker plot illustrating the Interquartile ranges of the path length in each strain. The asterisk indicates statistically significant differences ($p<0.01$) between the C57Bl/6 strain to the other two strains.

CHAPTER 6. TRANSLATION TO LARGE ANIMAL PROTOCOLS

6.1 INTRODUCTION

Advancements in Multi-row Detector Computed Tomography (MDCT) and Hyperpolarized gas MR Imaging have allowed researchers to perform detailed investigations of the human lung and accurately assess and characterize the structure of the lung through image based metrics such as density, texture, volumes and airway morphometry. Recent development in hyperpolarized ^{3}He studies have led to a new in-vivo lung morphometric analysis method that has allowed researchers to perform theoretical assessment of small airway and acinar morphometry (62, 74, 92, 107). These techniques have been able to identify regions of severe emphysema in patients with COPD through the variations in the apparent diffusion coefficient (ADC) (35, 107), track progression of induced emphysema in canines (92) and perform preliminary assessment of lung growth following pneumonectomy (6). . These techniques however rely on ideal models of the alveolar ducts as lineated in Chapter 1. In addition, the analysis techniques are limited by the voxel sizes typical in MR imaging. The latest MDCT systems provide the capability to image the lung in-vivo at relatively high resolutions of 0.5mm. This allow researchers to extend their analyses of the airway tree to the fifth through seventh generations providing greater insights into the branching structure of the central airways and regional characterization and assessment of parenchymal perfusion and ventilation. These methodologies are now being used to provide better understanding of the structural and physiologic alterations due to lung pathologies associated with diseases such as COPD (25). Traditional measurements of lung physiology cannot differentiate between abnormalities in the lung that arise from emphysema from those that result from other

causes such as asthma or bronchitis (47). MDCT based studies have helped develop models of the bronchial tree and the pulmonary vasculature, and seek to characterize phenotypes of the normal and diseased lung, allowing researchers to develop hypotheses that describe the physiological response to manifestations of pathology such as inflammation and hypoxic pulmonary vasoconstriction (25). These imaging tools provide detailed anatomical information allowing for comprehensive assessment of the lung down to the sub-lobar segments. However, the resolutions provided by these modalities do not provide the capability to directly image and assess the structural changes at the acinar and alveolar levels. Through the assessment of the small airways and alveolar ducts, researchers have been able to conclude that the obstruction of small airways in COPD was most strongly correlated with progression of the disease and was associated with airway wall thickening as a direct result of tissue repair and impaired mucociliary clearance (26). Other studies have revealed that central and peripheral airway inflammation can occur independent of each other (58). Changes to the airway lumen and branching patterns in the small airways have been observed in patients presenting with COPD and exposed to smoke inhalation (9). Currently, histological studies reflect the gold standard in assessing lung microstructure. In addition to some of the disadvantages already lineated, the use of histology in these studies limits the ability of researchers to perform 3D characterization of the airways and alveolar ducts, which can provide vital information about the branching patterns and structural geometry of the peripheral airways.

High-resolution microCT methodologies, such as the protocols outlined in this thesis, provide an alternative paradigm to perform assessment of the small airways and

microstructures, along with valuable information regarding the 3D architecture and remodeling of tissue geometry associated with COPD progression. Through the direct assessment of the 3D anatomy, we can provide solutions that seek to answer questions raised by the above studies regarding the etiology of pulmonary diseases.

The porcine lung is extensively used in research environments, as both stand-alone models of pulmonary diseases (33, 40, 104), and as a precursor to human clinical trials. The similarities in airway branching structure between porcine lungs and human lungs, along with other similarities in biochemistry and genetics allow researchers to use the porcine lung as a stand-in during the development of experimental protocols designed for human clinical use. In this chapter, we present protocols that allow us to perform SUR sampling of the fixed porcine lung, and by inference, on the human lung and perform morphometric assessment similar to measurements presented in murine lungs. A single porcine lung was evaluated to test the viability of transitioning the existing image acquisition and analysis protocols. The sampling techniques and high resolution imaging protocols have been applied to image and characterize the structure of a single acinus from the porcine lung under study.

6.2 METHODS

6.2.1 IN-VIVO IMAGING AND LUNG FIXATION

A Yucatan miniature pig was used in this study. The specimen used here was part of a larger cohort that was imaged as part of a different study seeking to correlate in vivo CT imaging-based metrics to post mortem histologic assessments (HL112986). One lung from these studies was used for the micro CT imaging we report here. All animal studies

were performed under the approval of the Institutional Animal Care and Use Committee (IACUC) at the University of Iowa. Similar to the murine protocols, the study animal was anesthetized and intubated to allow for mechanical control of respiration and static lung volume during CT acquisition. The animal was kept under anesthesia via vaporized isoflurane for the complete duration of the study. Physiological monitoring (ECG, $EtCO_2$, SPO_2) of the animal was performed throughout the study to maintain homeostasis of the physiological parameters. All scans were acquired with an at a static breath-hold inflation pressure of 25cmH_2O. A Somatom Definition CT (Siemens Medical Solutions, Erlangen, Germany) was utilized to gain chest CT data with three different protocols: high (14.98 mGy), medium (6.00 mGy) and 22 low (0.74 mGy) radiation exposure at a source voltage of 120kV, pitch of 1, and rotation time of 0.5 seconds. The dose variation protocols were part of the original study design to assess the minimum dose requirements and are not directly relevant to the methods or data presented here. The CT images were reconstructed at a slice thickness of 0.75 mm using a medium iterative reconstruction kernel (I30).

The perfusion fixation technique used in the murine specimens was adapted for the porcine lung. In the case of the porcine lungs, in order to minimize fixation volumes and simplify post-fixation surgeries, perfusion of the fixative solution was achieved after isolating the pulmonary vasculature. The lungs were exposed via a medial sternotomy, following which the lungs were isolated from surrounding anatomical structures. The pulmonary vasculature was isolated and flushed using a solution of hetastarch and heparin, similar to the procedure using the heparinized lactated ringer solution in mice. The fixative solution used was similar in chemical composition as previously presented in

mice. Perfusion of the fixative solution followed the flush solution. When the perfusion was complete, the chest cavity was filled with excess fixative solution, so as to completely submerge the lungs, and closed, to continue to fix the lungs in an approximation of the in-situ anatomic structure. Following perfusion of the fixative, the lungs were dried in a dryer unit at room temperature for 72 hours, with the inflation pressure at the endo-tracheal tube maintained at 25cmH_2O, to preserve the in-vivo like volumes. The fixed and dried lungs were imaged via quantitative CT ex-vivo to perform assessments of the shape and tissue integrity. In **Fig.32**, we show a series of images that outline the lung preparation and associated CT imaging. In order by row, from left to right, the images show: A 3D rendering of the lung from in-vivo images acquired at total lung capacity, a photograph of the final fixed intact lung and a 3D rendering of the fixed lung from ex-vivo images; series of CT image slices representing the in-vivo lung via axial, sagittal and coronal sections and a series of corresponding CT image slices representing the ex-vivo via axial, sagittal and coronal sections.

6.2.2 LUNG SECTIONING AND CORE SAMPLING

The high resolution scanner limits the size of the sample that can be imaged via interior tomography. Even with successful mounting of the sample onto the stage, large samples result in increased source-object and object-detector distances, leading to a reduction in signal to noise ratio and affecting the image resolution. The porcine lung therefore was sectioned into lung cores of size 2.5cm X 2.5cm X 2.5cm such that it is suitable for high resolution interior imaging. The SURS based sampling methodologies presented in the previous sections are applied first to physically section the porcine lung, followed by a secondary sampling step to sample acini from the core sample.

The first step in the sectioning process is the reduction of the three-dimensional lung to a stack of 2D-equivalent slabs of equal thickness. A custom made lung sectioning apparatus, constructed of a radiolucent medical grade plastic (Polyoxymethylene, commercially sold as Delrin), was used for this purpose. The lungs were placed into the sectioning box, shown in **Fig.33**, and completely covered in quick-setting spray foam to secure the lung during the sectioning process. The box has a series of slits on the longitudinal sides, which allow for the insertion of blades to cut the lung into slabs. These slits are separated by a distance of 2.5cm, resulting in sections approximating the typical FOV of current microCT systems. The physical placement of the lung in the box automatically incorporates randomness in the starting location of the first slab. The fractionator method is used to divide the stack of slabs and pick one slab from each stack for imaging.

Each selected slab is sectioned into a grid to derive cubed core samples. The cubed samples were sectioned with a grid spacing of 2.5cm, yielding three-dimensional lung cores of sides 2.5cmx2.5cmx2.5cm each. A sample core is shown in **Fig.33**. All the core samples are eligible for the acinar sampling process and one core was chosen at random. Each cube contains a number of acini and a second sampling process was utilized to select individual acini from each chosen core.

6.2.3 SCOUT AND ZOOM IMAGING

High resolution imaging was performed on a Versa 520 system (Zeiss Inc.) capable of multi-resolution imaging via the use of adjustable microscope objectives. This system, a recent acquisition at the University of Iowa, represents an upgraded model of the system used in the previous chapters. This system is capable of delivering the micron

and sub-micron resolutions with improved image contrast and reduced scan times. In addition, this system provides additional capabilities such as adjustable source filters, wide-field modes of acquisition and the ability to perform vertical stitching to combine multiple images of large specimens.

Each cube is subjected to the same workflow as the complete murine lung. An initial LFOV image is acquired at a resolution of ~16-20 µm. This image serves as a "scout" image, allowing us to perform sampling and focused interior tomographic imaging at specific regions of interest. The SURS protocols outlined in chapter 4 are repeated in order to set the field of view for acinar imaging. Since the purpose of this study is to demonstrate the viability of acinar analysis to large animals and human studies, a single acinus was chosen at random for analysis to demonstrate our ability to image and process the data. **Fig.34** shows an example of a LFOV slice, with the coordinates of the sampled acini and the corresponding HRES image. Additional high resolution images were obtained so as to backtrack from the terminal bronchiole feeding the acinus under study, to the upper airways. The central airways can be segmented from the whole lung ex-vivo images and matched to the LFOV core image. A 3D rendering of the upper airways is shown in **Fig.35A**. The acinus under analysis and the distal airways that feed the acinus are rendered and shown in **Fig.35 B and C**. The center-line skeleton image is also shown and color-coded for better visualization and separation of the acinar branches and the conducting airways. Image processing and morphometric assessment was carried out as previously outlined for the murine specimens. A radial tree representation of the acinar branching structure is shown in **Fig.35D**.

Because of the questions raised by Hogg et al (26) whereby they suggest that airways are lost prior to the loss of alveoli in smoking-associated emphysema, we have adapted our workflow to take advantage of the vertical stitching capability of the Versa 520 scanner. Through the acquisition of multiple HRES images, with known shifts in the axial position, we can back-track from the acinus and the bronchiole connecting it to the central airways.

6.3 RESULTS

The total lung volume was 2160 mm^3. This is comparable to the corresponding in-vivo baseline lung volumes of 1969 mm^3. This increase in volume can be attributed to overinflation of the lung during the fixation process and the opening of the thoracic cavity for access to the pulmonary vasculature. Acinar volume was 0.62 mm^3, yielding an estimate of 3484 acini in the porcine lung.

The diameter of the alveolar ducts varies from 630 ± 53.78 µm at the terminal bronchiole to 378 ± 45.16 µm at generation 11. The branch length varies from 372 ± 60.34 µm at the terminal bronchiole to 218 ± 54.78 µm at generation 11. The variations in branch diameter and branch length are shown in **Fig.36**. The mean longitudinal path length was 3.164 mm. The distribution of the longitudinal path lengths, expressed a percentage of total terminal nodes, is shown in **Fig.37**. A histogram analysis of branch counts by generation number is shown in **Fig.38**.

6.4 DISCUSSION

It has been previously presented in literature that there should be a direct proportionality between morphometry of the exchange system and oxygen consumption. Oxygen consumption varies as a power law of animal mass. Our results show evidence of similarities in the branching structure and arrangement of the acinar airspaces between the porcine and murine lung. There is an increase in the size of the acinus without significant difference in the structural organization of the alveolar ducts and alveolar sacs. This suggests that in higher order organisms, the size of the terminal functional respiratory units is increased, without significant differences in tissue and airspace geometries. Further investigations into the acinar structure via the sampling techniques presented earlier will provide statistically significant data that will help us understand the structural geometry of the porcine lung in detail.

The analyses presented in this chapter demonstrate the capability to transition the sampling, imaging and analysis techniques, developed for the murine acini, to large animal and potentially human lungs, without requiring significant changes. By performing this analysis on a larger set of fixed porcine lungs, with greater number of acinar samples per specimen, we can perform comprehensive assessment of the porcine acini and establish the normative acinar structure that can then lay the foundation for comparison with similar analysis on disease models. This technique can be applied to the multitudes of genetic knockout models that are used to study pulmonary diseases such as COPD, Cystic Fibrosis and Asthma, providing a unique understanding of the effects of disease progression on septal walls and alveolar destruction. Likewise we can do the

same thing for the human lung, allowing us to investigate the hypotheses (26, 27) regarding small airway occlusions and track the progression of disease.

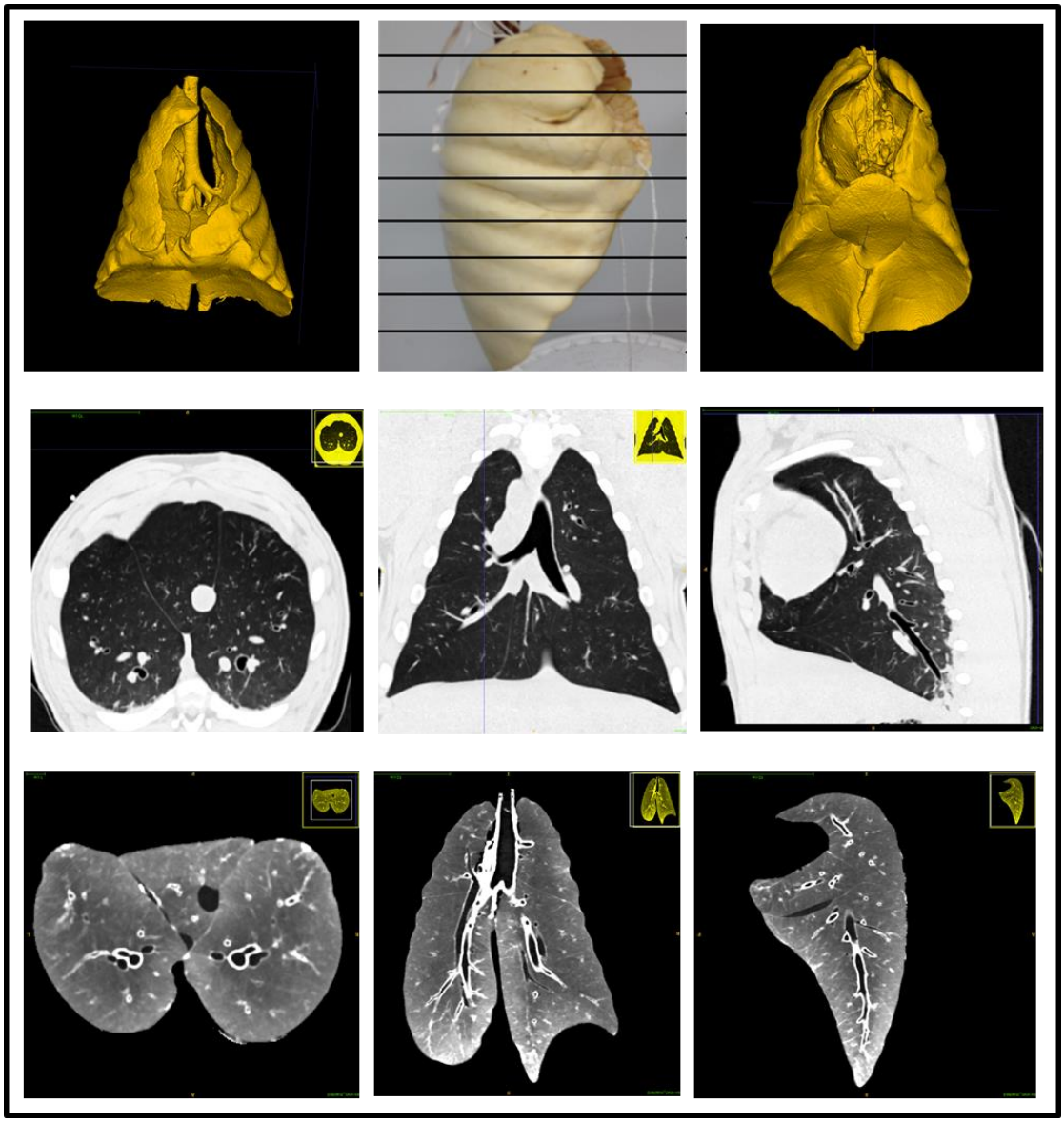

Figure 32. Steps in the sample preparation process. The images represent from left to right: 1st row: 3D rendering of the lung via in-vivo imaging; photograph of the excised lung post fixation and drying; 3D rendering of the ex-vivo lung; 2nd row: Axial, Sagittal and coronal views of the in-vivo lung; 3rd row: Axial Sagittal and Coronal views of the ex-vivo lung.

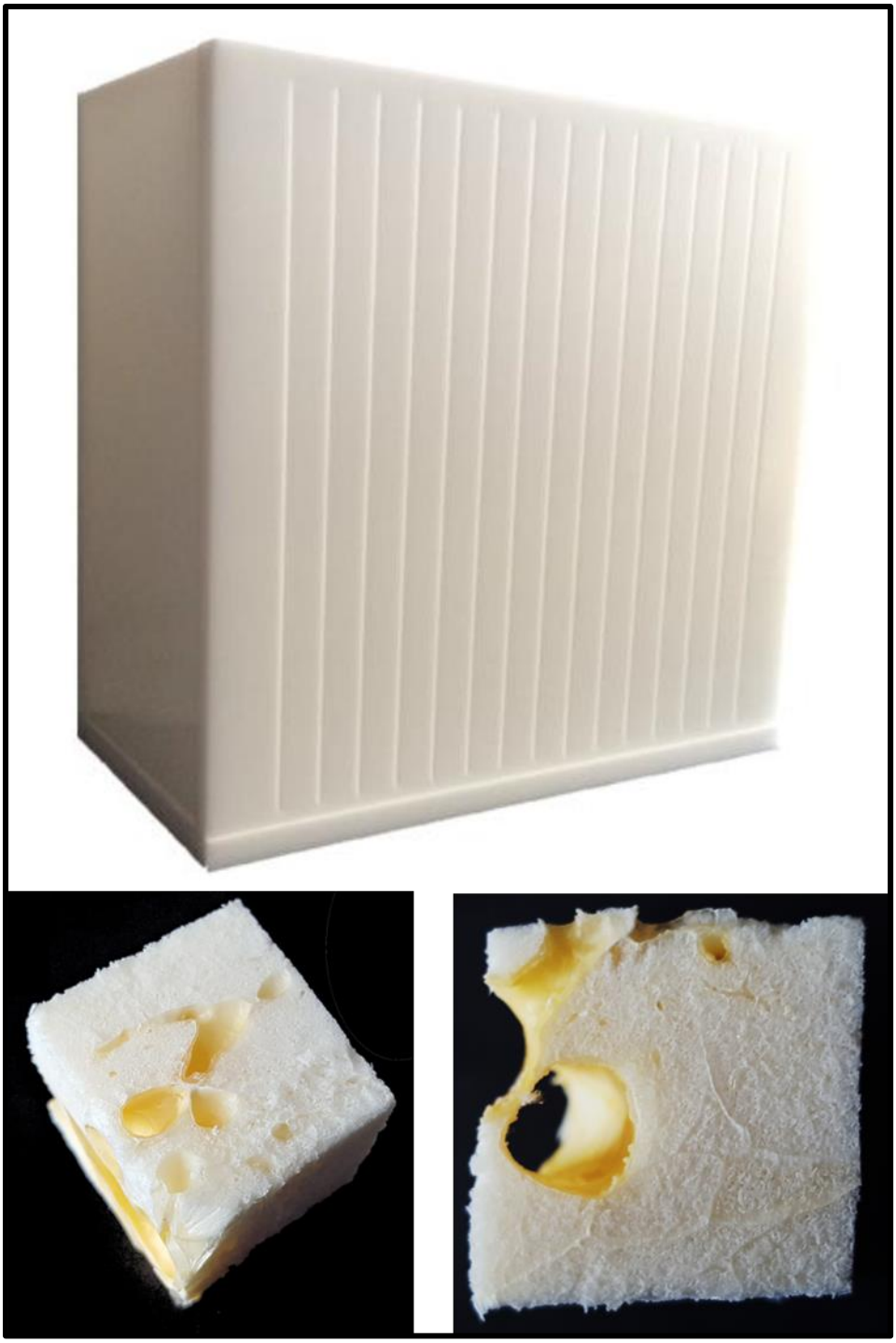

Figure 33. Porcine Sampling protocol. The sectioning box used to dissect the fixed lung into slabs is shown in Fig.A. B and C show the lung core samples that are the end result of the physical sampling process. The samples are cubes with side ~2.5µm. these samples are subjected to the same image-based sampling process as the whole murine lungs.

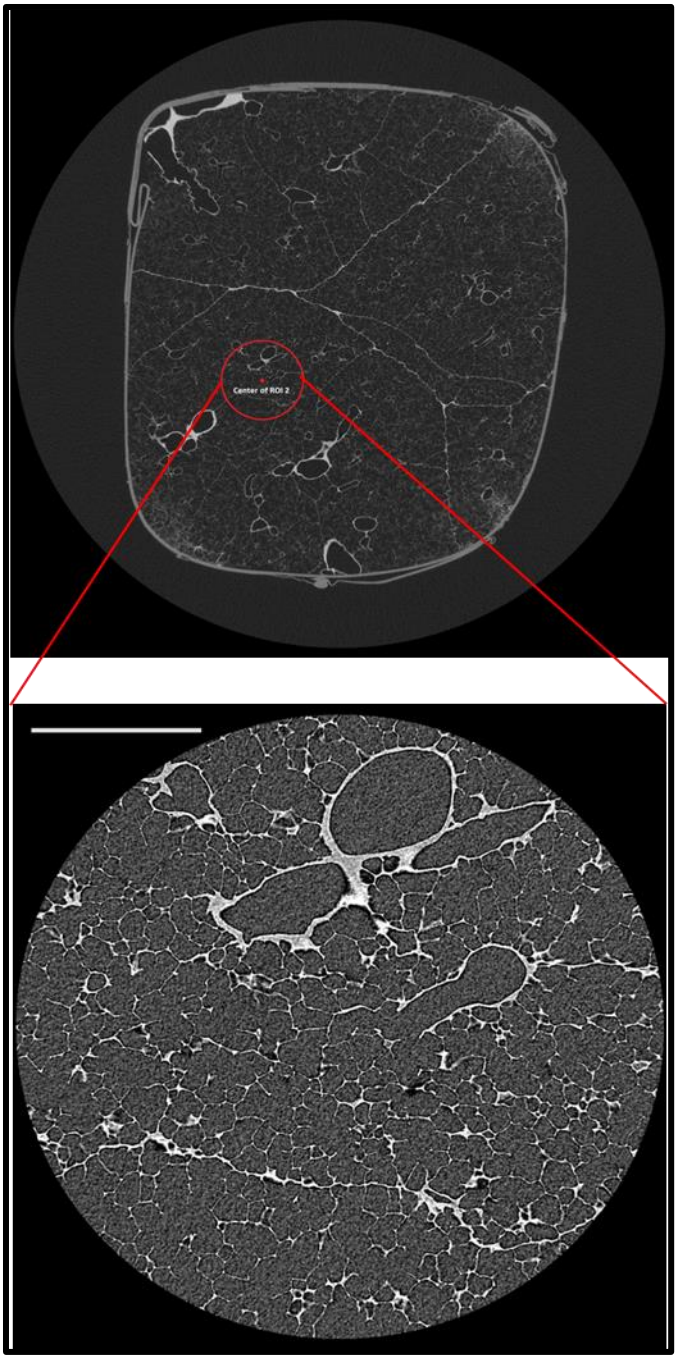

Figure 34. Porcine Imaging protocol. The first image depicts the LFOV image of a single cube obtained by sectioning the fixed lung. The HRES image obtained by scout and zoom at the location specified in the LFOV image is shown at the bottom. The structures in the HRES image can be tracked directly on the LFOV image. The zoom in scale represents a change from a resolution of 16µm in the LFOV image to ~2.1µm in the HRES image.

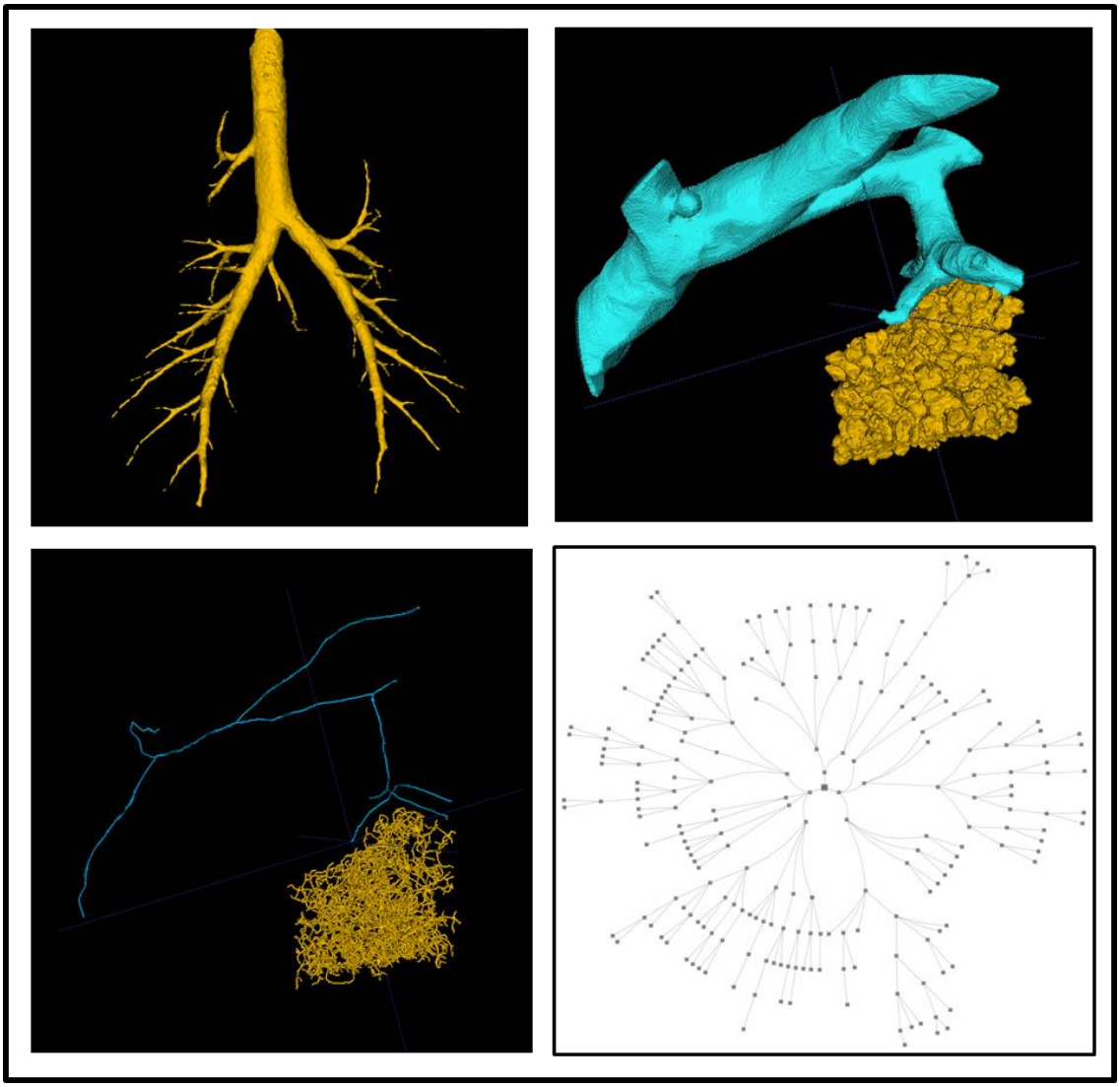

Figure 35. A 3D rendering of the upper airways. B,C - The 3D rendered model depicts the acinus in the HRES image along with the bronchiole that feeds the acinus under study. By tracking the HRES image to LFOV and LFOV to the whole lung ex-vivo image, it is possible to derive a complete airway tree from the trachea down to the acinus. A flattened radial tree representation of the porcine acinus is shown in D.

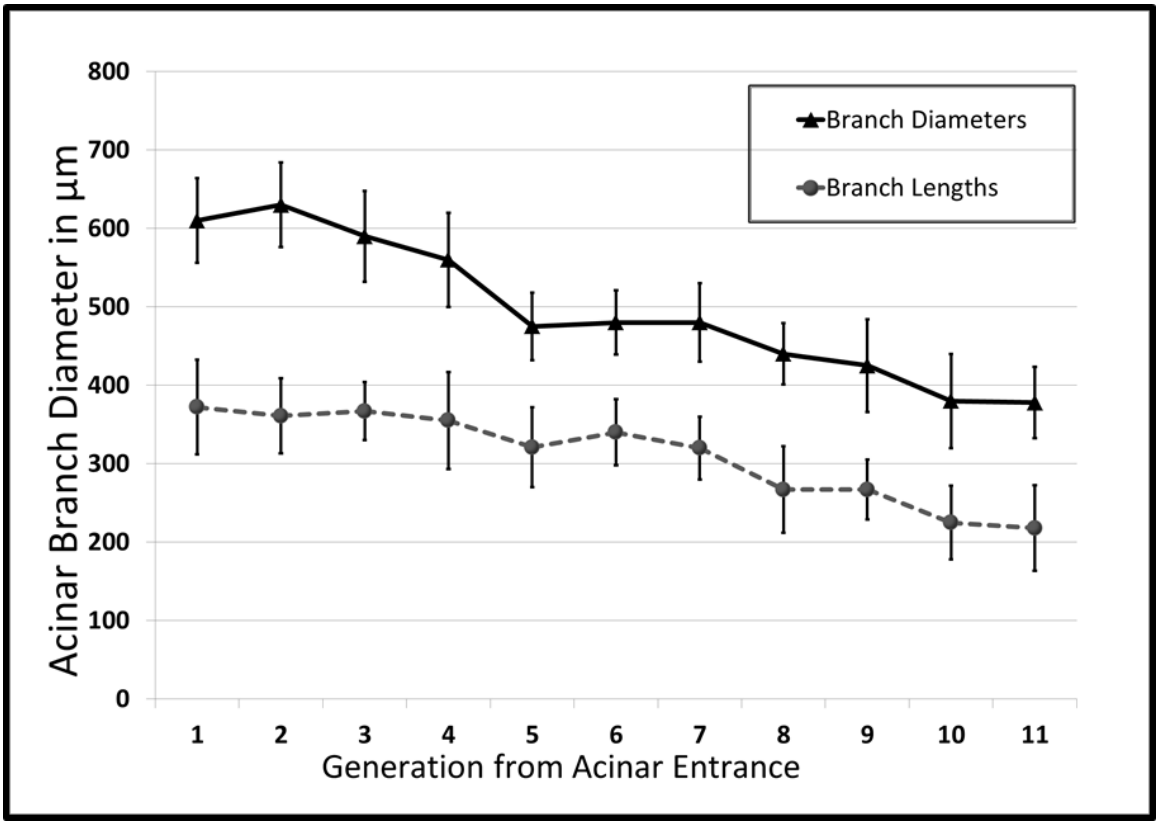

Figure 36. Morphometric Measurements in the Porcine acinus. The graph shows the variations in Branch Diameters and Branch Lengths with increase in generation number as measured from the acinar entrance.

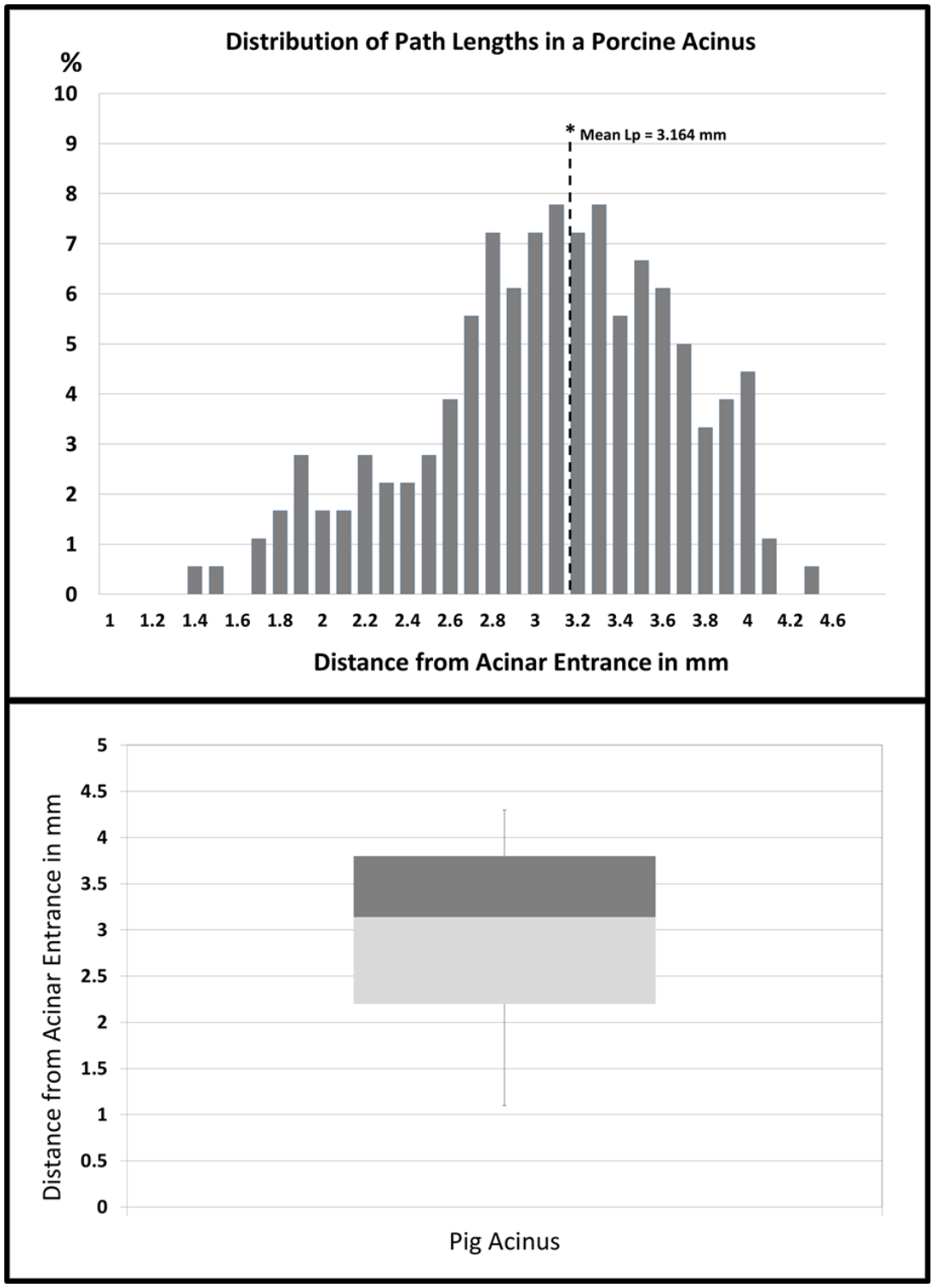

Figure 37. Distribution of Path Lengths in the Porcine Lung. A - histogram analysis of the percentage distribution of the longitudinal path length. B - Box and whisker plot illustrating the interquartile range of the longitudinal path lengths in the acinus under study.

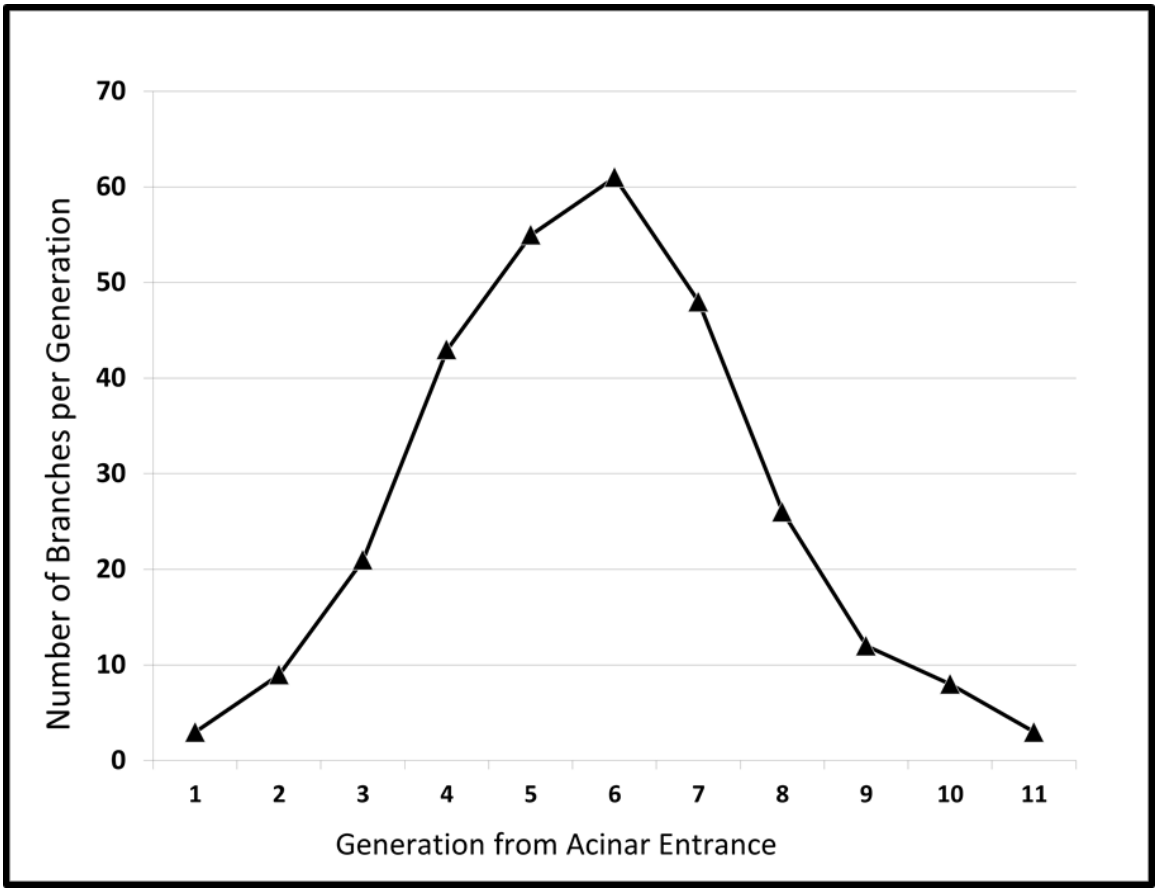

Figure 38. Histogram analysis of branch counts by generation number as measured from the entrance to the acinus.

CHAPTER 7. REGISTRATION BASED ACINAR DEFORMATIONS

7.1 INTRODUCTION

Understanding of flow phenomena in the pulmonary acinus is important for the computational modeling of gas exchange, alveolar mechanics and in predicting particle transport and deposition (22,24) and by inference, in designing effective drug delivery strategies to the alveolar epithelium. Conventional approaches to acinar and alveolar mechanics involve the use of theoretical and numerical techniques (14, 24, 36, 37, 75, 76, 86, 89). Examples of standard acinar models include three-dimensional honeycomb-like straight duct geometry involving a central airspace and surrounding alveoli used to represent an alveolar duct and sacs (10, 90) and regular polyhedral shaped models (64). Most existing mathematical and structural models are based on average morphometric assessments of the acinus, from studies that used traditional methods outlined previously. These models treat the acinus as a homogenous structure and are limited in the ability to simulate the variations in branch morphometry within the acinus and across regions in the lung. Such computational models are therefore limited in their investigations. Normal acinar morphometry has been shown to have asymmetric arrangement of alveolar sacs along with non-dichotomous branching patterns that vary between acini. Recent studies have sought to use heterogeneous models that attempt to theoretically simulate the heterogeneity of the branch morphometry and shapes and sizes of alveoli (5, 38, 41). Image based models, based on the segmented acini from high-resolution microCT images provide a near-anatomical modeling of the architecture of the parenchyma (42, 43, 96) and has the potential to provide comprehensive quantitative assessment of the mechanics of lung function and its relationship to the underlying tissue geometry.

Current high-resolution morphometric studies, including those presented in the previous chapters, have sought to characterize the normal acinus via examination of ex-vivo lungs fixed at a single inflation pressure that mirrors in-vivo imaging protocols. A direct assessment of the change in acinar morphometry with change in the inflation pressure will necessitate the preparation, imaging and analysis of a large number of acini at each volume. In this chapter, we explore the possibility of using in-vivo images, acquired at multiple inflation pressures, to simulate the acinar deformation via registration derived deformation maps. These registration frameworks have been previously applied to define the boundary conditions to study the airflow dynamics within the murine acinus (43) but have not focused on assessing the morphometric parameters, which is the aim of this chapter.

7.2 METHODS

The in-vivo volume data from the C57BL/6 mice used in Chapter 3 was used for preliminary exploration of the registration framework. Analysis of the deformation of one murine acinus was performed and is presented here. The in-vivo MicroCT images were found to have high noise and a number of artifacts that can affect the accuracy of segmentation and consequently, the registration process. In addition, scanner source and stage calibrations at the high-resolution imaging site limited the number of samples and the accuracy of the workflow. As an alternative, the porcine lung used in Chapter 6 was subjected to the same workflow to provide a better test specimen for the registration framework. The animal was imaged in-vivo at steady inflation pressures of 20 and 25cmH_2O, which provided the adequate image samples for registration.

REGISTRATION FRAMEWORK

The registration framework employed for acinar deformations is shown in fig X. In-vivo datasets provide the source of generating the Jacobian maps that represent the deformation of the lung at different inflation pressures. In order to reliably estimate the change in the branch morphometry of the acinus in a fixed lung from in-vivo images, multi-step registration is required. The multi-step registration process is as follows:

NON-RIGID REGISTRATION OF IN-VIVO IMAGES:

The in-vivo CT images acquired baseline inflation pressure (20 cmH2O) is used as the reference image against which all other images are matched. The other available in-vivo volumes are registered to this baseline volume using a mass preserving image registration algorithm (111, 112), which utilizes the tissue volume fraction as the registration metric. The percent tissue volume is calculated locally within the lung in both the fixed and moving image and the transformation matrix that minimizes the sum of square of the difference in the tissue volume fractions provides the best approximation of matched image volumes. A composite of six levels of B-splines are used to describe lung motion.

RIGID REGISTRATION OF HIGH RESOLUTION IMAGES:

The Scout and Zoom imaging workflow of the Zeiss Versa 520 (and the previous generation XRadia MicroXCT400) scanners provide direct information of the physical coordinates of the sample being imaged. Knowledge of the exact coordinates of the center of the FOV of the high resolution acinar images with respect to the LFOV whole lung (or core) image allows for the mapping of the acinar high resolution image to its physical location in the lung. Using the scanner derived coordinates as a starting point, a

rigid transformation (translation and rotation) is used to orient and map the acinar image to the whole lung ex-vivo image. In the case of the porcine lung, the high-resolution acinar image is registered to the core sample, which is then registered to the whole lung ex-vivo image, in a two-step process. The ex-vivo image is then registered onto the baseline in-vivo image corresponding to the ex-vivo inflation pressure (20cmH_2O). In order to account for intensity variations between in-vivo and ex-vivo images, the mutual information metric is used as the similarity in this step of the registration workflow. The deformation is achieved by a combination of rigid, affine and 4 levels of B-Splines transformation. The deformations thus obtained can be applied to map the acinus from the ex-vivo high-resolution image to each in-vivo volume. The deformation can also be directly applied to the acinar segmentation mask and to the center-line skeleton to simulate the deformation of the acinus at different inflation pressures.

The registration framework used in this analysis is illustrated in **Fig. 39**.The in-vivo images (A) are registered with the baseline image resulting in the Jacobian map (B). Ex-vivo registrations are shown in yellow arrows with the extra step of registering the porcine HRES image (C) to the core (D) shown via dotted lines. The final registration step allows the extraction of the regional deformation map (F) that can be applied to the HRES image to simulate acinar deformation. Acinar morphometric analysis is repeated for each of the deformed acinar volumes to estimate change in acinar geometry.

7.3 RESULTS

The volume of the whole ex-vivo murine lung was reduced by 6.1% in comparison to the in-vivo volume (1170.98 mm^3 vs. 1099.69 mm^3) at the end of the

fixation process. This volume difference was reduced to 3.4% after registration (1131.17 mm^3) as shown in **Fig.40**. On average, there is a 10% increase in branch diameters and 5% increase in branch lengths from the 20cmH_2O volume to the 25cmH_2O volume. The change in morphometric measurements in the murine acinus is illustrated in **Fig.41A**. There is evidence for anisotropic changes in the morphometry of the alveolar ducts at each generation, with reduced anisotropy at the alveolar sacs. There are non-uniform changes in volume and surface area within the acinus. The acinar volume was increased by 6.2% while alveolar surface area was increased by 5.4%. The overall surface area to volume ratio (S/V) is similar at both inflation pressures. The results of the porcine acinus are shown in **Fig.41B**. The ex-vivo volume of the porcine lung was found to be 9.7% higher than the in-vivo baseline volume (2160.11 mL vs. 1969.18 mL) due to over-inflation and the opening of the thoracic cavity during the fixation process. This volume difference was reduced and found to be 4.8% after registration (2063.7 mL). The porcine lung exhibited similar anisotropies as observed in the murine lung, with an average increase of 12% in branch diameters and 8% in branch lengths and reduced anisotropy at the alveolar sacs. The acinar volume was increased by 7.5%. S/V ratios were preserved in the porcine acinus similar to the results of the murine lung.

7.4 DISCUSSION

The image based deformations yield interesting insights to the nature of expansion in the acinus. There is evidence of anisotropic expansion of the alveolar ducts at each generation. The current data suggests that with increase in inflation pressures, the alveolar ducts have greater expansion radially than along the axial length of the duct. This trend

was observed in both species and warrants further investigations. The evidence for anisotropy in the expansion of the alveolar ducts is in agreement with the predictions presented by Kumar et al.(43), where the researchers used estimates of S/V ratios to characterize the nature of duct expansion by comparing their estimates with theoretical estimates of radial only, axial only and hemispherical expansions. It is not clear if this state of expansion is maintained throughout the normal pressure range for the animal or if it is isolated to the narrow range of inflation pressures analyzed in this study. The anisotropy in branch deformation and the variations across generations are especially important in the modeling of alveolar flow dynamics. Studies have demonstrated the effects of isotropic wall motion on relative particle depositions (9) and in the flow structure using image velocimetry (7, 8). Previous studies have applied similar registration deformations to assess the mechanics of the alveolar wall and analyze heterogeneity in the mechanical properties of septal tissue. In chapter 4, we have demonstrated evidence for variations in the structural geometry across acini based on their location within the lung and proximity to the pleural surface. An investigation of these regional samples via the registration based deformations presented in this chapter can provide additional information that will help characterize acinar response to increasing inflation pressures. An in-depth analysis of the physiological implications can be performed by an extended study on a larger sample size to investigate these potential variations in acinar deformation between central and surface acini.

Inspection of the Jacobian map of the porcine lung shows regions of high volume changes ($|J|>2.5$) in parts of the lung that do not correspond to realistic physiological deformation. Such registration artifacts might result from errors in the datasets such as

irregular segmentation borders. These errors highlight the need for high quality segmentation masks and warrant further investigation of the registration workflow. In addition, the registration based method is unable to assess or predict the mechanisms of alveolar recruitment, and the mechanical interdependence in acini, but provides a simple mechanism to study the changes in alveolar and acinar morphometry with inflation pressure without the need to prepare specimens at each pressure range. Improvements in registration techniques (especially between in-vivo and ex-vivo images) can be incorporated into the workflow and provide more accurate results describing acinar inflation. Through the use of the wide-field mode operation and vertical stitching features of the Versa 520 systems, we can image and characterize neighboring acini as an attempt to delve further into the nature of the mechanical interdependence between acini. Through the expansion of the inflation pressure range and application of the SURS techniques previously outlined, we show proof of techniques that can be further developed to generate accurate comprehensive data describing the heterogeneity in acinar response to inflation pressures.

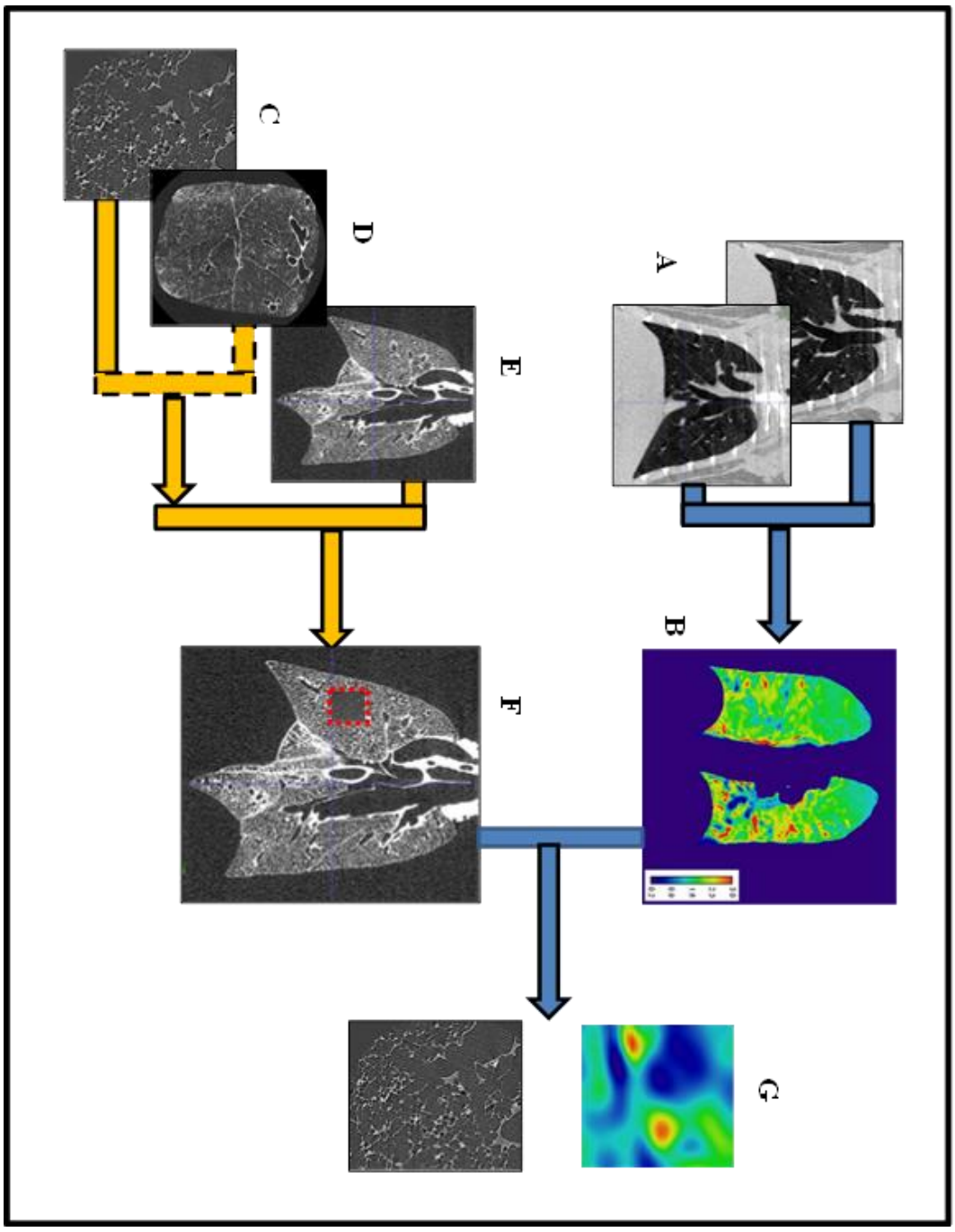

Figure 39. Multi-step registration framework. The in-vivo registration 'A' yields the deformation map 'B'. 'C', 'D' and 'E' represent ex-vivo LFOV and HRES images. 'F' represents the LFOV image registered with the HRES image shown in the red box. The local deformation corresponding to the HRES location is shown in 'G'.

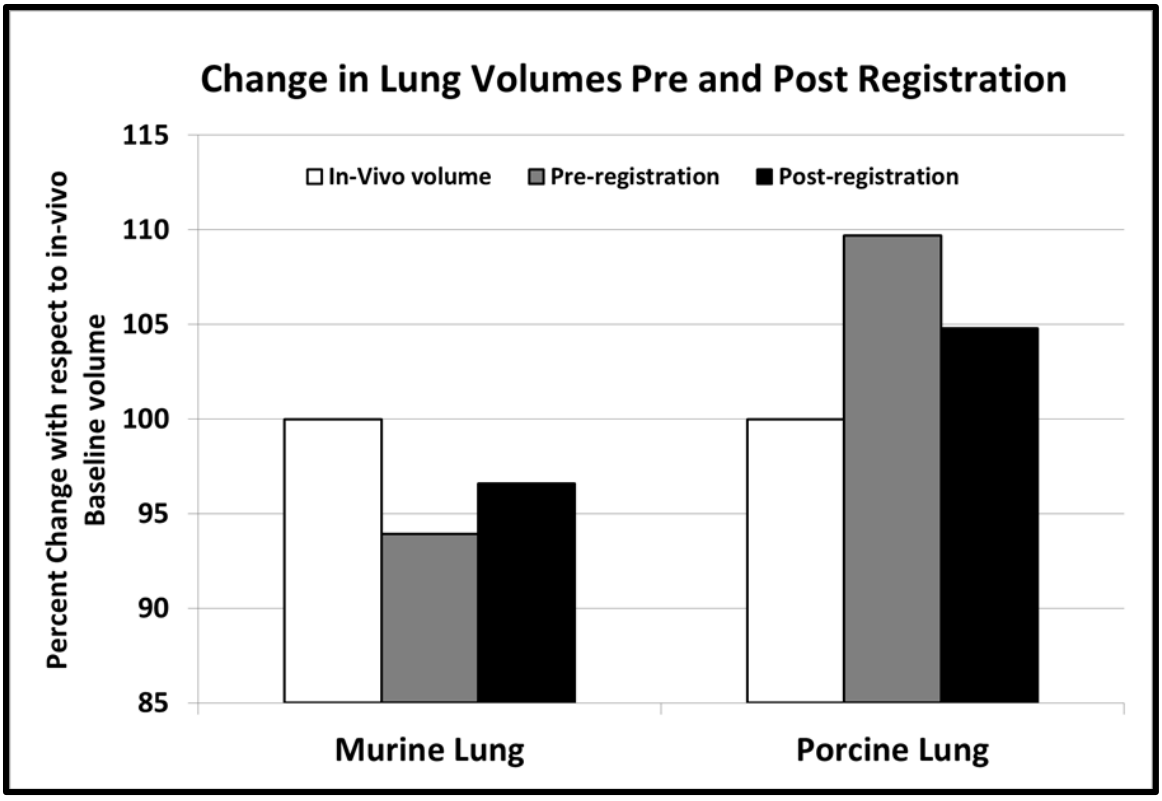

Figure 40. Percent change in Lung volumes between ex-vivo and in-vivo images. The post-registration ex-vivo volume is closer to the in-vivo volume indicating improvement due to registration.

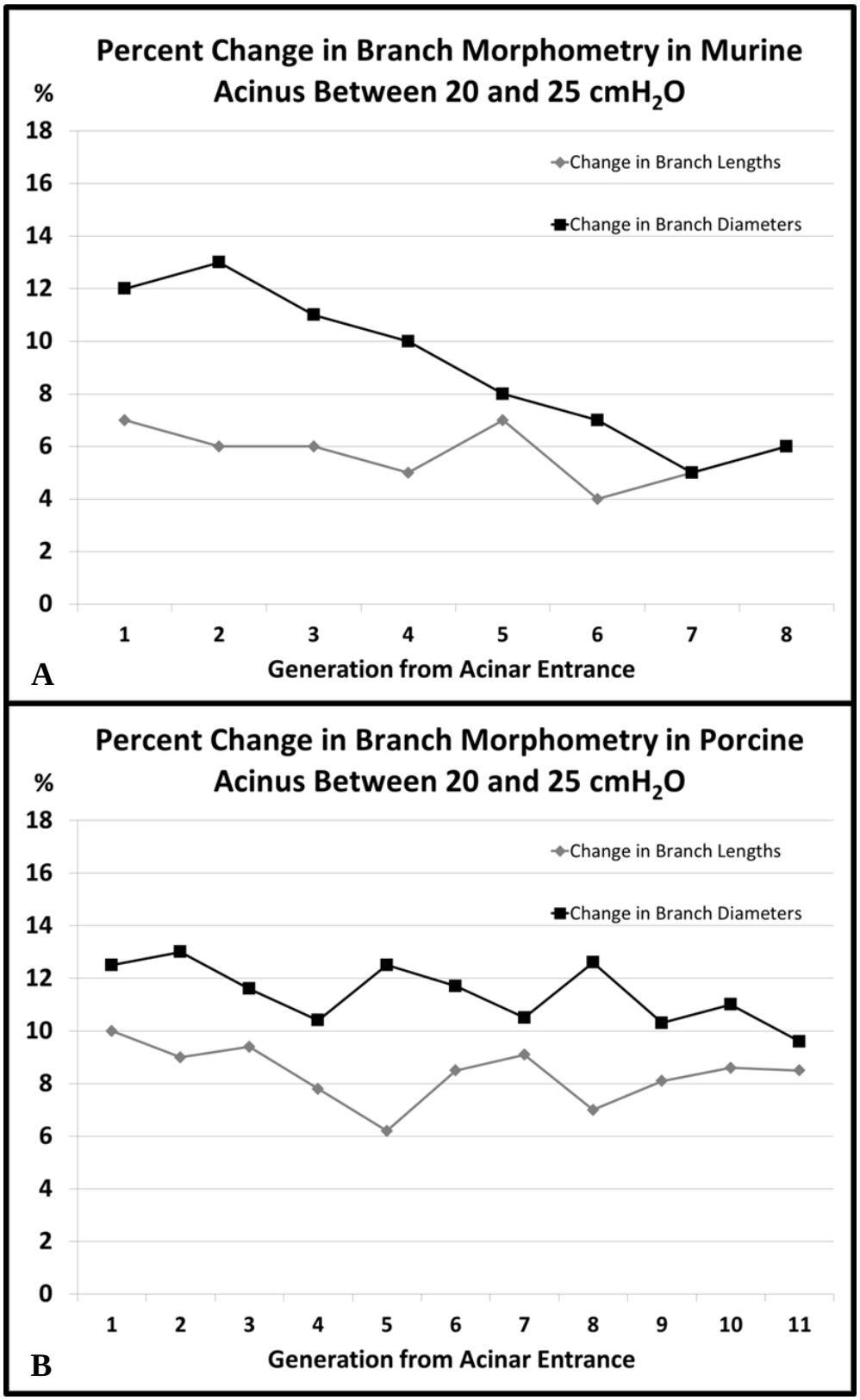

Figure 41. A, B - Change in Murine and Porcine Acinar Branch Morphometry respectively with increase in inflation from Baseline. Both Branch diameters and Lengths are shown in the same graph.

CHAPTER 8. CONCLUSIONS

8.1 CONTRIBUTIONS

The overall aim of this dissertation was to develop a set of imaging protocols, sampling methodologies and analysis tools to perform morphometric assessment of the acinar airspaces. The accomplishments and challenges faced in each of the aims are outlined below.

Aim 1: We have successfully developed and applied center-line based image analysis and quantitative assessment techniques to perform assessment of the acinar branch morphometry. The semi-automated methods presented here provide a simple and easy to use alternative to traditional methods such as serial histological sectioning, and allow for non-destructive visualization and analysis of large datasets. The morphometric measurements have been tested to assess sensitivity to noise and have been found to be robust over the range typically observed during acquisition. Most errors can be minimized by supervision during the pre-processing steps to ensure object connectivity is maintained. The center-line based method was tested on two sets of C57BL/6 mice belonging to two widely separated age groups and has demonstrated evidence of structural changes that manifest in the older mice. Through this analysis, we have generated data that will allow us to develop new hypotheses on the nature of age-dependent structural reconfiguration in the lung. Due to the wide step in the age of the two groups, we are unable to comment directly on the underlying mechanisms that drive this structural reconfiguration. A study design with additional time points that span the current age gap under study may provide a better understanding of the physiological driving forces. The analysis of morphometric relationship between parent-child branches

and sibling branches may allow for the potential classification of acinar branch morphometry and, in conjunction with traditional analysis techniques such as stereology, provide a greater understanding of acinar development and the mechanics of gas exchange. The methods and results presented in Chapter 1 have been published in the Journal of Applied Physiology (39) and in multiple conference proceedings of the American Thoracic Society (ATS).

Aim 2: We have successfully transferred previously developed sampling principles to the particular task of evaluating lungs via interior tomography. The region-based sampling techniques allow us to evaluate and characterize the heterogeneity in acinar morphometry in normal or diseased lungs. The flexibility of the regional sampling allows us to identify and isolate acini from different anatomical locales of interest. The use of SURS techniques also ensures efficient study design, minimizing the number of samples needed to characterize the regions of interest. In addition, application of SURS to imaging allows us to perform stereological assessment of the pulmonary structures by treating the high-resolution microCT slices similar to histological slides. The significant differences observed in central and surface acini provide us with the knowledge necessary to understand and interpret the results of other imaging techniques such as OCT and MRI that have relied on the homogenous nature of acinar branching throughout the lung. The flattened radial tree representation of the acinar branching structure provides a clear visual understanding of the complexity of the acinar airspaces. This representation can be extended to the central airways and provide an elegant approach to visually identify and compare branching patterns in the central and peripheral airways.

Aim 3: A comprehensive assessment of the variations in acinar morphometry across the three strains of mice has been presented. As common research strains used in pulmonary research and as control groups in disease models, the data presented here will provide critical information in understanding the inherent differences in acinar morphometry and in interpreting the structural changes that are a result of pathology, leading to improved computational modeling. The joint assessment of central and surface acini was made necessary in order to test the data against the C57BL/6 strain, for which regional samples were not available. While the results are promising, a matched comparison between central acini and between surface acini from each strain will yield comprehensive data that will allow us to assess the nature of heterogeneity in the lung. We are currently working on the analysis of additional datasets for the C57Bl/6 mice acquired using the sampling techniques used for the other two strains, in order to ensure a uniform protocol across all three strains.

Aim 4: We have demonstrated the capability to translate our acinar morphometric analysis techniques to large animals and, through inference, to lung samples from human subjects. The flexibility of the methods presented here, in conjunction with the use of suitable sampling and sample preparation, allow us to perform characterization of acinar airspaces without any significant change to the imaging protocols or the analysis workflow. We have successfully migrated our small animal imaging protocols and presented data from one specimen as a proof of concept in our transition to large animal species. We have also added additional imaging capabilities to track the small airways that connect the central airways to the bronchioles that lead into the acini. Through the continuation of this work, we expect to develop similar analysis tools for assessing

normal acinar structure in human lungs along with the identification of aberrant branching patterns in the peripheral airways in patients presenting with pathology.

Aim 5: We have successfully applied image registration techniques to perform deformation of the acini in the murine and porcine model to assess changes in acinar morphometry with inflation pressure. While the registration performance in the murine models is currently limited due to high image artefacts, the registration framework itself is successful with improved image quality. This framework can take advantage of developments in registration techniques via new similarity metrics and computational advancements to provide improved analysis of acinar deformation. The current registration models in porcine datasets allow for higher quality of analysis than in murine lungs and provide an insight into the nature of deformation at the acinar and alveolar levels. Extension of this assessment to an increased number of datasets from lungs fixed at different inflation pressures will provide validation of our simulated acinar morphometric response to inflation.

8.2 LIMITATIONS

The major challenge in the present analysis workflow is the significant time involvement and manual interaction required, especially at the branch point selection stage. In order to improve the speed of analysis, we are currently developing automated branch point selection algorithms that can prune the center-line to automatically eliminate small branches and identify loop structures and mark them for deletion based on user approval.

The other challenge was in the registration framework, especially for murine specimens. The levels of noise and artefacts in the microCT images affect the accuracy of the image matching algorithms. The use of improved scanner hardware and reconstruction techniques can minimize the effect of noise. In the case of the porcine lung, the greater challenge was in the surgical process in fixing the lungs in-situ and excising the lung without damage or deforming the shape of the lung. With surgical training, these distortions can be minimized.

8.3 FUTURE WORK

Currently, the directions of potential research resulting from this research are three-fold:

Complete automation of morphometric analysis:

The semi-automated tool can be improved and fully automated to reduce the significant amount of time required for the operator to perform branch point selections. Full automation will also allow for the batch computation and analysis of acini, allowing increased sample sizes without significant increase in time. We are currently in the process of integrating our sampling and analysis techniques with the in-house Pulmonary Analysis Software Suite (PASS), which will enable us to focus on automation and computational efficiency.

Application of morphometric analysis to disease models:

The data presented in this research represents the information about the normal structure of the murine and porcine lungs. This provides baseline parenchymal

characterization upon which further studies can be developed. By applying these analysis techniques to disease models or knockout strains with genetic pre-dispositions to specific states of pathology, we can study the progression of disease states such as emphysema, COPD, cystic fibrosis, etc. and gain critical information on the structural changes associated with disease progression. We are currently applying the analysis techniques presented in this thesis to investigate evidence of structural changes in the lung in a genetic knockout mouse strain pre-disposed to non-orthopedic disorders.

Extension of analysis to other species:

By developing a flexible workflow, we have the capability to study other species without significant difficulties. Currently, we are working with collaborators from UT-Southwestern, to apply our acinar morphometry techniques to study the changes associated with lung regrowth after pneumonectomy in dogs and are exploring collaborations with the University of British Columbia to study the morphometry of human pulmonary acini preserved using different techniques. We also have interest from collaborators at Mc.Gill University who have identified aberrant branching patterns in the upper airways of patients who present with COPD and are interested in using our analysis techniques to assess these variations and the downstream impact on the bronchioles and alveolar ducts.

In this thesis, we have presented a technique to perform comprehensive assessment of murine acini that can be extended to other mammalian species with ease. In conjunction with advanced sampling techniques, our methods allow researchers to identify, image, directly assess and understand the 3D structure of a pulmonary acinus, leading to improved mathematical and near-anatomical models of pulmonary structure.

Through the quantitative metrics and characterization and visualization tools, we present data that will help researchers better understand the architecture and geometry of the micro-structure of the lung. Through the use of such improved models and structural analysis, we provide an opportunity to better understand respiratory physiology in the normal lung and follow pathophysiology in the diseased lung.

REFERENCES

1. Terminology, Definitions, and Classification of Chronic Pulmonary Emphysema and Related Conditions: A Report of the Conclusions of a Ciba Guest Symposium. *Thorax* 14: 286-299, 1959.

2. **Barré Sé F, Haberthür D, Stampanoni M, and Schittny JC**. Efficient estimation of the total number of acini in adult rat lung. *Physiological Reports* 2: 2014.

3. **Boyden EA**. The structure of the pulmonary acinus in a child of six years and eight months. *The American journal of anatomy* 132: 275-299, 1971.

4. **Bult CJ, Krupke DM, Begley DA, Richardson JE, Neuhauser SB, Sundberg JP, and Eppig JT**. Mouse Tumor Biology (MTB): a database of mouse models for human cancer. *Nucleic acids research* 43: D818-824, 2015.

5. **Burrowes KS, Swan AJ, Warren NJ, and Tawhai MH**. Towards a virtual lung: multi-scale, multi-physics modelling of the pulmonary system. *Philosophical transactions Series A, Mathematical, physical, and engineering sciences* 366: 3247-3263, 2008.

6. **Butler JP, Loring SH, Patz S, Tsuda A, Yablonskiy DA, and Mentzer SJ**. Evidence for Adult Lung Growth in Humans. *New England Journal of Medicine* 367: 244-247, 2012.

7. **Chhabra S, and Prasad AK**. Flow and particle dispersion in a pulmonary alveolus--part I: velocity measurements and convective particle transport. *Journal of biomechanical engineering* 132: 051009, 2010.

8. **Chhabra S, and Prasad AK**. Flow and particle dispersion in a pulmonary alveolus--part II: effect of gravity on particle transport. *Journal of biomechanical engineering* 132: 051010, 2010.

9. **Darquenne C, Harrington L, and Prisk GK**. Alveolar duct expansion greatly enhances aerosol deposition: a three-dimensional computational fluid dynamics study. *Philosophical transactions Series A, Mathematical, physical, and engineering sciences* 367: 2333-2346, 2009.

10. **Denny E, and Schroter RC**. A mathematical model for the morphology of the pulmonary acinus. *Journal of biomechanical engineering* 118: 210-215, 1996.

11. **Dijkstra EW**. A note on two problems in connexion with graphs. *Numer Math* 1: 269-271, 1959.

12. **Drazen JM, Finn PW, and De Sanctis GT**. Mouse models of airway responsiveness: physiological basis of observed outcomes and analysis of selected examples using these outcome indicators. *Annual review of physiology* 61: 593-625, 1999.

13. **Eppig JT, Blake JA, Bult CJ, Kadin JA, and Richardson JE**. The Mouse Genome Database (MGD): facilitating mouse as a model for human biology and disease. *Nucleic acids research* 43: D726-736, 2015.

14. **Felici M, Filoche M, Straus C, Similowski T, and Sapoval B**. Diffusional screening in real 3D human acini--a theoretical study. *Respir Physiol Neurobiol* 145: 279-293, 2005.

15. **Fernandez VE, McCaskill V, Atkins ND, and Wanner A**. Variability of airway responses in mice. *Lung* 177: 355-366, 1999.

16. **Gao Z, Vasilescu DM, Hoffman EA, and Saha PK**. A Multi-Scale Topo-Morphologic Opening Approach For Segmenting The Pulmonary Acinus In High Resolution Micro-CT Images Of Fixed Murine Lungs. In: *B70 FINE ANALYSIS OF ALVEOLAR/AIRWAY STRUCTURE AND FUNCTION*American Thoracic Society, 2010, p. A3630-A3630.

17. **Gardi C, Martorana PA, de Santi MM, van Even P, and Lungarella G**. A biochemical and morphological investigation of the early development of genetic emphysema in tight-skin mice. *Experimental and molecular pathology* 50: 398-410, 1989.

18. **Gomez-Arroyo J, Saleem SJ, Mizuno S, Syed AA, Bogaard HJ, Abbate A, Taraseviciene-Stewart L, Sung Y, Kraskauskas D, Farkas D, Conrad DH, Nicolls MR, and Voelkel NF**. A brief overview of mouse models of pulmonary arterial hypertension: problems and prospects. *American journal of physiology Lung cellular and molecular physiology* 302: L977-991, 2012.

19. **Gundersen HJ**. Stereology of arbitrary particles. A review of unbiased number and size estimators and the presentation of some new ones, in memory of William R. Thompson. *J Microsc* 143: 3-45, 1986.

20. **Gundersen HJG**. The smooth fractionator. *Journal of Microscopy* 207: 191-210, 2002.

21. **Gundersen HJG, and Jensen EB**. The efficiency of systematic sampling in stereology and its prediction*. *Journal of Microscopy* 147: 229-263, 1987.

22. **Haberthur D, Barre SF, Tschanz SA, Yao E, Stampanoni M, and Schittny JC**. Visualization and stereological characterization of individual rat lung acini by high-resolution X-ray tomographic microscopy. *Journal of applied physiology (Bethesda, Md : 1985)* 115: 1379-1387, 2013.

23. **Haefeli-Bleuer B, and Weibel ER**. Morphometry of the human pulmonary acinus. *The Anatomical record* 220: 401-414, 1988.

24. **Hofemeier P, and Sznitman J**. Revisiting pulmonary acinar particle transport: convection, sedimentation, diffusion, and their interplay. *Journal of Applied Physiology* 118: 1375-1385, 2015.

25. **Hoffman EA, Simon BA, and McLennan G**. A Structural and Functional Assessment of the Lung via Multidetector-Row Computed Tomography: Phenotyping Chronic Obstructive Pulmonary Disease. *Proceedings of the American Thoracic Society* 3: 519-532, 2006.

26. **Hogg JC, Chu F, Utokaparch S, Woods R, Elliott WM, Buzatu L, Cherniack RM, Rogers RM, Sciurba FC, Coxson HO, and Paré PD**. The Nature of Small-Airway Obstruction in Chronic Obstructive Pulmonary Disease. *New England Journal of Medicine* 350: 2645-2653, 2004.

27. **Hogg JC, McDonough JE, Sanchez PG, Cooper JD, Coxson HO, Elliott WM, Naiman D, Pochettino M, Horng D, Gefter WB, and Wright AC**. Micro–Computed Tomography Measurements of Peripheral Lung Pathology in Chronic Obstructive Pulmonary Disease. *Proceedings of the American Thoracic Society* 6: 546-549, 2009.

28. **Horsfield K**. Morphometry of Airways. *Compr Physiol 2011, Supplement 12: Handbook of Physiology, The Respiratory System, Mechanics of Breathing: 75-88*.

29. **Hsia CC, Hyde DM, Ochs M, and Weibel ER**. An official research policy statement of the American Thoracic Society/European Respiratory Society: standards for quantitative assessment of lung structure. *American journal of respiratory and critical care medicine* 181: 394-418, 2010.

30. **Huang K, Rabold R, Schofield B, Mitzner W, and Tankersley CG**. Age-dependent changes of airway and lung parenchyma in C57BL/6J mice. *Journal of Applied Physiology* 102: 200-206, 2007.

31. **Ito S, Bartolak-Suki E, Shipley JM, Parameswaran H, Majumdar A, and Suki B**. Early emphysema in the tight skin and pallid mice: roles of microfibril-associated glycoproteins, collagen, and mechanical forces. *American journal of respiratory cell and molecular biology* 34: 688-694, 2006.

32. **Ito S, Ingenito EP, Arold SP, Parameswaran H, Tgavalekos NT, Lutchen KR, and Suki B**. Tissue heterogeneity in the mouse lung: effects of elastase treatment. *Journal of Applied Physiology* 97: 204-212, 2004.

33. **Judge EP, Hughes JM, Egan JJ, Maguire M, Molloy EL, and O'Dea S**. Anatomy and bronchoscopy of the porcine lung. A model for translational respiratory medicine. *American journal of respiratory cell and molecular biology* 51: 334-343, 2014.

34. **Keil M, Lungarella G, Cavarra E, van Even P, and Martorana PA**. A scanning electron microscopic investigation of genetic emphysema in tight-skin, pallid, and beige mice, three different C57 BL/6J mutants. *Laboratory investigation; a journal of technical methods and pathology* 74: 353-362, 1996.

35. **Kirby M, Svenningsen S, Kanhere N, Owrangi A, Wheatley A, Coxson HO, Santyr GE, Paterson NA, McCormack DG, and Parraga G**. Pulmonary ventilation visualized using hyperpolarized helium-3 and xenon-129 magnetic resonance imaging: differences in COPD and relationship to emphysema. *Journal of applied physiology (Bethesda, Md : 1985)* 114: 707-715, 2013.

36. **Kitaoka H, and Itoh H**. Computer-assisted three-dimensional volumetry of the human pulmonary acini. *The Tohoku journal of experimental medicine* 167: 1-12, 1992.

37. **Kitaoka H, Nieman GF, Fujino Y, Carney D, DiRocco J, and Kawase I**. A 4-dimensional model of the alveolar structure. *The journal of physiological sciences : JPS* 57: 175-185, 2007.

38. **Kitaoka H, Tamura S, and Takaki R**. A three-dimensional model of the human pulmonary acinus. *Journal of applied physiology (Bethesda, Md : 1985)* 88: 2260-2268, 2000.

39. **Kizhakke Puliyakote AS, Vasilescu DM, Sen-Sharma K, Wang G, and Hoffman EA**. A Skeleton-Tree Based Approach to Acinar Morphometric Analysis Using Micro Computed Tomography with Comparison of Acini in Young and Old C57Bl/6 Mice. *Journal of Applied Physiology* 2016.

40. **Kobayashi E, Hishikawa S, Teratani T, and Lefor AT**. The pig as a model for translational research: overview of porcine animal models at Jichi Medical University. *Transplantation Research* 1: 8-8, 2012.

41. **Koshiyama K, and Wada S**. Mathematical model of a heterogeneous pulmonary acinus structure. *Computers in biology and medicine* 62: 25-32, 2015.

42. **Kumar H, Tawhai MH, Hoffman EA, and Lin C-L**. The effects of geometry on airflow in the acinar region of the human lung. *Journal of biomechanics* 42: 1635-1642, 2009.

43. **Kumar H, Vasilescu DM, Yin Y, Hoffman EA, Tawhai MH, and Lin CL**. Multiscale imaging and registration-driven model for pulmonary acinar mechanics in the mouse. *Journal of applied physiology (Bethesda, Md : 1985)* 114: 971-978, 2013.

44. **Lee TC, Kashyap RL, and Chu CN**. Building Skeleton Models via 3-D Medial Surface Axis Thinning Algorithms. *CVGIP: Graphical Models and Image Processing* 56: 462-478, 1994.

45. **Lorensen WE, and Cline HE**. Marching cubes: A high resolution 3D surface construction algorithm. In: *ACM siggraph computer graphics*ACM, 1987, p. 163-169.

46. **Lorenz RJ**. Weibel, E. R.: Morphometry of the Human Lung. Springer Verlag, Berlin-Göttingen-Heidelberg 1963; 151 S., 109 Abb., DM 36. *Biometrische Zeitschrift* 8: 143-144, 1966.

47. **Macklem PT**. The pathophysiology of chronic bronchitis and emphysema. *The Medical clinics of North America* 57: 669-670, 1973.

48. **Mata JF, Altes TA, Cai J, Ruppert K, Mitzner W, Hagspiel KD, Patel B, Salerno M, Brookeman JR, de Lange EE, Tobias WA, Wang H-TJ, Cates GD, and Mugler JP**. Evaluation of emphysema severity and progression in a rabbit model: comparison of hyperpolarized 3He and 129Xe diffusion MRI with lung morphometry. *Journal of Applied Physiology* 102: 1273-1280, 2007.

49. **McDonough JE, Knudsen L, Wright AC, Elliott WM, Ochs M, and Hogg JC**. Regional differences in alveolar density in the human lung are related to lung height. *Journal of Applied Physiology* 118: 1429-1434, 2015.

50. **McLaughlin RA, Noble PB, and Sampson DD**. Optical Coherence Tomography in Respiratory Science and Medicine: From Airways to Alveoli. *Physiology* 29: 369-380, 2014.

51. **McLaughlin RA, Yang X, Quirk BC, Lorenser D, Kirk RW, Noble PB, and Sampson DD**. Static and dynamic imaging of alveoli using optical coherence tomography needle probes. *Journal of Applied Physiology* 113: 967-974, 2012.

52. **Meissner S, Knels L, and Koch E**. Improved three-dimensional Fourier domain optical coherence tomography by index matching in alveolar structures. *Journal of biomedical optics* 14: 064037-064037-064037, 2009.

53. **Meissner S, Knels L, Schnabel C, Koch T, and Koch E**. Three-dimensional Fourier domain optical coherence tomography in vivo imaging of alveolar tissue in the intact thorax using the parietal pleura as a window. *Journal of biomedical optics* 15: 016030, 2010.

54. **Meißner S, Krüger A, Wendel M, Knels L, Heller A, Koch T, and Koch E**. Determination of Alveolar Geometry by Optical Coherence Tomography to Develop a Numerical Model of the Fluid Dynamics in the Pulmonary Acinus. In: *Advances in Medical Engineering*, edited by Buzug T, Holz D, Bongartz J, Kohl-Bareis M, Hartmann U, and Weber SSpringer Berlin Heidelberg, 2007, p. 337-342.

55. **Mercer RR, and Crapo JD**. Three-dimensional reconstruction of the rat acinus. *Journal of applied physiology (Bethesda, Md : 1985)* 63: 785-794, 1987.

56. **Miao R, Liu J, and Wang J**. Overview of mouse pulmonary embolism models. *Drug Discovery Today: Disease Models* 7: 77-82, 2010.

57. **Moeller A, Ask K, Warburton D, Gauldie J, and Kolb M**. The bleomycin animal model: a useful tool to investigate treatment options for idiopathic pulmonary fibrosis? *The international journal of biochemistry & cell biology* 40: 362-382, 2008.

58. **Mullen JB, Wright JL, Wiggs BR, Pare PD, and Hogg JC**. Reassessment of inflammation of airways in chronic bronchitis. *British medical journal (Clinical research ed)* 291: 1235-1239, 1985.

59. **Namati E, Chon D, Thiesse J, Hoffman EA, de Ryk J, Ross A, and McLennan G**. In vivo micro-CT lung imaging via a computer-controlled intermittent iso-pressure breath hold (IIBH) technique. *Physics in medicine and biology* 51: 6061-6075, 2006.

60. **Namati E, Thiesse J, de Ryk J, and McLennan G**. Alveolar Dynamics during Respiration. *American journal of respiratory cell and molecular biology* 38: 572-578, 2008.

61. **Oldham MJ, and Phalen RF**. Dosimetry implications of upper tracheobronchial airway anatomy in two mouse varieties. *The Anatomical record* 268: 59-65, 2002.

62. **Osmanagic E, Sukstanskii AL, Quirk JD, Woods JC, Pierce RA, Conradi MS, Weibel ER, and Yablonskiy DA**. Quantitative assessment of lung microstructure in healthy mice using an MR-based 3He lung morphometry technique. *Journal of Applied Physiology* 109: 1592-1599, 2010.

63. **Palagyi K, Tschirren J, Hoffman EA, and Sonka M**. Quantitative analysis of pulmonary airway tree structures. *Computers in biology and medicine* 36: 974-996, 2006.

64. **Parameswaran H, Majumdar A, and Suki B**. Linking microscopic spatial patterns of tissue destruction in emphysema to macroscopic decline in stiffness using a 3D computational model. *PLoS computational biology* 7: e1001125, 2011.

65. **Paulus MJ, Gleason SS, Kennel SJ, Hunsicker PR, and Johnson DK**. High resolution X-ray computed tomography: an emerging tool for small animal cancer research. *Neoplasia (New York, NY)* 2: 62-70, 2000.

66. **Phillips CG, and Kaye SR**. On the asymmetry of bifurcations in the bronchial tree. *Respiration Physiology* 107: 85-98, 1997.

67. **Popp A, Wendel M, Knels L, Koch T, and Koch E**. Imaging of the three-dimensional alveolar structure and the alveolar mechanics of a ventilated and perfused isolated rabbit lung with Fourier domain optical coherence tomography. *Journal of biomedical optics* 11: 014015-014015-014019, 2006.

68. **Quirk JD, Lutey BA, Gierada DS, Woods JC, Senior RM, Lefrak SS, Sukstanskii AL, Conradi MS, and Yablonskiy DA**. In Vivo Detection of Acinar Microstructural Changes in Early Emphysema with 3He Lung Morphometry. *Radiology* 260: 866-874, 2011.

69. **Reinhard C, Eder G, Fuchs H, Ziesenis A, Heyder J, and Schulz H**. Inbred strain variation in lung function. *Mammalian genome : official journal of the International Mammalian Genome Society* 13: 429-437, 2002.

70. **Ritman EL**. Micro-computed tomography of the lungs and pulmonary-vascular system. *Proc Am Thorac Soc* 2: 477-480, 501, 2005.

71. **Robertson HT, Kreck TC, and Krueger MA**. The spatial and temporal heterogeneity of regional ventilation: Comparison of measurements by two high-resolution methods. *Respiratory Physiology & Neurobiology* 148: 85-95, 2005.

72. **Rodriguez M, Bur S, Favre A, and Weibel ER**. Pulmonary acinus: Geometry and morphometry of the peripheral airway system in rat and rabbit. *American Journal of Anatomy* 180: 143-155, 1987.

73. **Saha PK, Zhiyun G, Alford SK, Sonka M, and Hoffman EA**. Topomorphologic Separation of Fused Isointensity Objects via Multiscale Opening: Separating Arteries and Veins in 3-D Pulmonary CT. *Medical Imaging, IEEE Transactions on* 29: 840-851, 2010.

74. **Salerno M, Altes TA, Brookeman JR, de Lange EE, and Mugler JP**. Dynamic spiral MRI of pulmonary gas flow using hyperpolarized 3He: Preliminary studies in healthy and diseased lungs. *Magnetic Resonance in Medicine* 46: 667-677, 2001.

75. **Sapoval B, Filoche M, and Weibel ER**. Smaller is better—but not too small: A physical scale for the design of the mammalian pulmonary acinus. *Proceedings of the National Academy of Sciences* 99: 10411-10416, 2002.

76. **Sapoval B, Weibel ER, and Filoche M**. Diffusion Screening, Acinus Size and Optimal Design of Mammalian Lungs. In: *Fractals in Biology and Medicine*, edited by Losa GA, Merlini D, Nonnenmacher TF, and Weibel ER. Basel: Birkhäuser Basel, 2002, p. 25-38.

77. **Schindelin J, Arganda-Carreras I, Frise E, Kaynig V, Longair M, Pietzsch T, Preibisch S, Rueden C, Saalfeld S, Schmid B, Tinevez JY, White DJ, Hartenstein V, Eliceiri K, Tomancak P, and Cardona A**. Fiji: an open-source platform for biological-image analysis. *Nature methods* 9: 676-682, 2012.

78. **Schittny JC, and Burri PH**. Development and growth of the lung. *Fishman's pulmonary diseases and disorders* 1: 91-115, 2008.

79. **Schlesinger RB, and McFadden LA**. Comparative morphometry of the upper bronchial tree in six mammalian species. *The Anatomical record* 199: 99-108, 1981.

80. **Schreider JP, and Raabe OG**. Structure of the human respiratory acinus. *The American journal of anatomy* 162: 221-232, 1981.

81. **Schulz H, Johner C, Eder G, Ziesenis A, Reitmeier P, Heyder J, and Balling R**. Respiratory mechanics in mice: strain and sex specific differences. *Acta physiologica Scandinavica* 174: 367-375, 2002.

82. **Shapiro SD**. Transgenic and gene-targeted mice as models for chronic obstructive pulmonary disease. *The European respiratory journal* 29: 375-378, 2007.

83. **Smith CM, Finger JH, Hayamizu TF, McCright IJ, Xu J, Berghout J, Campbell J, Corbani LE, Forthofer KL, Frost PJ, Miers D, Shaw DR, Stone KR, Eppig JT, Kadin JA, Richardson JE, and Ringwald M**. The mouse Gene Expression Database (GXD): 2014 update. *Nucleic acids research* 42: D818-824, 2014.

84. **Soutiere SE, and Mitzner W**. On defining total lung capacity in the mouse. *Journal of Applied Physiology* 96: 1658-1664, 2004.

85. **Soutiere SE, Tankersley CG, and Mitzner W**. Differences in alveolar size in inbred mouse strains. *Respir Physiol Neurobiol* 140: 283-291, 2004.

86. **Stauber H, Fishler R, Hofemeier P, Waisman D, and Sznitman J**. Particle dispersion in morphologically-inspired computational models of alveolar capillary networks. *International Journal of Experimental and Computational Biomechanics* 3: 300-318, 2015.

87. **Sukstanskii AL, and Yablonskiy DA**. In vivo lung morphometry with hyperpolarized 3He diffusion MRI: Theoretical background. *Journal of Magnetic Resonance* 190: 200-210, 2008.

88. **Sukstanskii AL, and Yablonskiy DA**. Lung morphometry with hyperpolarized 129Xe: Theoretical background. *Magnetic Resonance in Medicine* 67: 856-866, 2012.

89. **Swan AT, Merryn H**. Evidence for minimal oxygen heterogeneity in the healthy Human Pulmonary Acinus. *J Appl Physiol* 110(528-537), 2010.

90. **Sznitman J**. Respiratory microflows in the pulmonary acinus. *J Biomech* 46: 284-298, 2013.

91. **Tankersley CG, Rabold R, and Mitzner W**. Differential lung mechanics are genetically determined in inbred murine strains. *Journal of applied physiology (Bethesda, Md : 1985)* 86: 1764-1769, 1999.

92. **Tanoli TSK, Woods JC, Conradi MS, Bae KT, Gierada DS, Hogg JC, Cooper JD, and Yablonskiy DA**. In vivo lung morphometry with hyperpolarized 3He diffusion MRI in canines with induced emphysema: disease progression and comparison with computed tomography. *Journal of Applied Physiology* 102: 477-484, 2007.

93. **Taubin G**. Curve and surface smoothing without shrinkage. In: *Proceedings of the Fifth International Conference on Computer Vision*IEEE Computer Society, 1995, p. 852.

94. **Thiesse J, Namati E, Sieren JC, Smith AR, Reinhardt JM, Hoffman EA, and McLennan G**. Lung structure phenotype variation in inbred mouse strains revealed through in vivo micro-CT imaging. *Journal of Applied Physiology* 109: 1960-1968, 2010.

95. **Tschirren J, Hoffman EA, McLennan G, and Sonka M**. Intrathoracic airway trees: segmentation and airway morphology analysis from low-dose CT scans. *IEEE transactions on medical imaging* 24: 1529-1539, 2005.

96. **Tsuda A, Filipovic N, Haberthur D, Dickie R, Matsui Y, Stampanoni M, and Schittny JC**. Finite element 3D reconstruction of the pulmonary acinus imaged by synchrotron X-ray tomography. *Journal of applied physiology (Bethesda, Md : 1985)* 105: 964-976, 2008.

97. **Vasilescu DM, Gao Z, Saha PK, Yin L, Wang G, Haefeli-Bleuer B, Ochs M, Weibel ER, and Hoffman EA**. Assessment of morphometry of pulmonary acini in mouse lungs by nondestructive imaging using multiscale microcomputed tomography. *Proc Natl Acad Sci U S A 109(42):17105-10 (2012), PMID 23027935* 2012.

98. **Vasilescu DM, Klinge C, Knudsen L, L Y, G W, E.R. W, M O, and E.A. H**. Stereological assessment of mouse lung parenchyma via nondestructive, multiscale micro-CT imaging validated by light microscopic histology. *J Appl Physiol* 716-724, 2013.

99. **Vasilescu DM, Knudsen L, Ochs M, Weibel ER, and Hoffman EA**. Optimized murine lung preparation for detailed structural evaluation via micro-computed tomography. *Journal of applied physiology (Bethesda, Md : 1985)* 112: 159-166, 2012.

100. **Walters DM, and Kleeberger SR**. Mouse models of bleomycin-induced pulmonary fibrosis. *Current protocols in pharmacology / editorial board, SJ Enna (editor-in-chief) [et al]* Chapter 5: Unit 5.46, 2008.

101. **Wang W, Nguyen NM, Yablonskiy DA, Sukstanskii AL, Osmanagic E, Atkinson JJ, Conradi MS, and Woods JC**. Imaging lung microstructure in mice with hyperpolarized 3He diffusion MRI. *Magnetic Resonance in Medicine* 65: 620-626, 2011.

102. **Weibel ER, and Gomez DM**. Architecture of the human lung. Use of quantitative methods establishes fundamental relations between size and number of lung structures. *Science (New York, NY)* 137: 577-585, 1962.

103. **Weibel ER, Hsia CCW, and Ochs M**. How much is there really? Why stereology is essential in lung morphometry. *Journal of Applied Physiology* 102: 459-467, 2007.

104. **Welsh MJ, Rogers CS, Stoltz DA, Meyerholz DK, and Prather RS**. Development of a porcine model of cystic fibrosis. *Transactions of the American Clinical and Climatological Association* 120: 149-162, 2009.

105. **West JB**. *Respiratory physiology--the essentials*. Baltimore: Williams & Wilkins, 1985, p. x, 183 p.

106. **Wood SA, Zerhouni EA, Hoford JD, Hoffman EA, and Mitzner W**. Measurement of three-dimensional lung tree structures by using computed tomography. *Journal of applied physiology (Bethesda, Md : 1985)* 79: 1687-1697, 1995.

107. **Woods JC, Choong CK, Yablonskiy DA, Bentley J, Wong J, Pierce JA, Cooper JD, Macklem PT, Conradi MS, and Hogg JC**. Hyperpolarized 3He diffusion MRI and histology in pulmonary emphysema. *Magnetic Resonance in Medicine* 56: 1293-1300, 2006.

108. **Wulfsohn D, Knust J, Ochs M, Nyengaard JR, and Gundersen HJG**. Stereological estimation of the total number of ventilatory units in mice lungs. *Journal of Microscopy* 238: 75-89, 2010.

109. **Xiao L, Sera T, Koshiyama K, and Wada S**. A Semiautomatic Segmentation Algorithm for Extracting the Complete Structure of Acini from Synchrotron Micro-CT Images. *Computational and Mathematical Methods in Medicine* 2013: 575086, 2013.

110. **Yablonskiy DA, Sukstanskii AL, Woods JC, Gierada DS, Quirk JD, Hogg JC, Cooper JD, and Conradi MS**. Quantification of lung microstructure with hyperpolarized 3He diffusion MRI. *Journal of Applied Physiology* 107: 1258-1265, 2009.

111. **Yin Y, Hoffman EA, Ding K, Reinhardt JM, and Lin CL**. A cubic B-spline-based hybrid registration of lung CT images for a dynamic airway geometric model with large deformation. *Physics in medicine and biology* 56: 203-218, 2011.

112. **Yin Y, Hoffman EA, and Lin C-L**. Mass preserving nonrigid registration of CT lung images using cubic B-spline. *Medical Physics* 36: 4213-4222, 2009.

113. **Yushkevich PA, Piven J, Hazlett HC, Smith RG, Ho S, Gee JC, and Gerig G**. User-guided 3D active contour segmentation of anatomical structures: significantly improved efficiency and reliability. *NeuroImage* 31: 1116-1128, 2006.

114. **Zeltner TB, Bertacchini M, Messerli A, and Burri PH**. Morphometric Estimation of Regional Differences in the Rat Lung. *Experimental Lung Research* 16: 145-158, 1990.